UNIVERSITY OF CALIFORNIA, SAN DIEGO

Light-Assisted Biopatterning of Hydrogels for Investigating Cell Interactions within their Microenvironment

A dissertation submitted in partial satisfaction of the
requirements for the degree Doctor of Philosophy

in

NanoEngineering

by

Kolin C. Hribar

Committee in charge:

Professor Shaochen Chen, Chair
Professor Liangfang Zhang, Co-Chair
Professor Adam Engler
Professor Michael Heller
Professor Shyni Varghese

2015

The Dissertation of Kolin C. Hribar is approved, and it is acceptable in quality and form for publication on microfilm and electronically:

Co-Chair

Chair

University of California, San Diego

2015

DEDICATION

I dedicate my work to my family, friends, mentors and supporters.

To my parents – you have stressed and strived to put your kids in the best schools since we were born. You've always challenged me to think outside the box and to pursue only the greatest version of myself. You have engrained in me a sense of hard work and commitment to the violin, school, and sports from when I was a baby. I thank you your patience, support, and autonomy while I navigated the waters of early adulthood.

To my sisters, for showing me competition and the art of winning, exposing me to science, medicine, music and design, as well as outdoor and sports excursions. And to my sister's husbands, who have been like brothers to me.

To my grandparents – a constant inspiration of hope, happiness, and wisdom.

To our Swiss friends, for showing me that life is beautiful and should be maximally enjoyed every single day, with no let up and complaints. To our dogs, Montana and Niko – for the love and joy they brought us.

To my close friends, who have pushed me throughout my life, whether knowingly or unknowingly. To the countless games of chess, tennis, soccer, lacrosse, and music concerts, and being just as much of an explorer as I am. Our bond is unshaken and I am truly honored to call you all my friends and companions.

To my teachers, coaches, and mentors over the years – for imparting their knowledge, the joy to learn, to play, and to be free, to not take everything seriously, and pushing me to think different.

EPIGRAPH

"Try not to become a man of success, but rather try to be a man of value"
–Albert Einstein

Your work is going to fill a large part of your life, and the only way to be truly satisfied is to do what you believe is great work. And the only way to do great work is to love what you do. If you haven't found it yet, keep looking. Don't settle. As with all matters of the heart, you'll know when you find it.
–Steve Jobs

"Fail fast, fall often"

"Innovation is an endless quest – very few products are so good that they cannot be continually improved upon"
–Richard Branson

"We have no rose without its thorn; no pleasure without alloy.
It is the law of our existence, and we must acquiesce.
–Thomas Jefferson

TABLE OF CONTENTS

LIST OF FIGURES

Chapter 1

Chapter 2

Chapter 3

ACKNOWLEDGEMENTS

I would first like to thank my doctoral advisor, Dr. Shaochen Chen, PhD, who brought me to UCSD as a PhD student after a few emails and a skype meeting. From the beginning, he demonstrated faith in my research ability and creativity to think outside the box, and gave me autonomy to explore what I found the most scientifically engaging in his field of 3D bioprinting, while providing insightful discussion and guidance along the way. To my collaborators and committee members, who have vastly expanded my knowledge in the fields of tissue engineering and cancer diagnostics – Dr. Kristiina Vuori, Dr. Ben Finlay, Dr. Amy Rommel, Dr. Inder Verma, Dr. Yu Suk Choi, Dr. Adam Engler, Dr. Liangfang Zhang, Dr. Michael Heller, and Dr. Shyni Varghese, and many more. To my Chen labmates, who provided helpful and unbiased critique of my work that pushed me to be a better engineer, teammate, and researcher.

To my undergraduate and Masters advisor in Bioengineering at the University of Pennsylvania – Dr. Jason Burdick, PhD – who took a chance on me as a transfer student from the Chemical Engineering Department. After a meeting to discuss my research experience from UCSF, we drafted up a quick sketch of a concept that would later form the basis of my research in his lab for the remaining three years at Penn. I look back on that experience and not only cherish my in-lab accomplishments but the friendships, bonding, and love for learning and research I gained from all members of Burdick Lab.

To Dr. Ivan El-Sayed, MD, at UCSF Medical School. He took me under his wing as a lowly freshman undergrad looking for a research position as I returned home for the summer in 2006, and again in the summer and winter of 2007. As a jack of many trades – including a full-time head and neck oncology surgeon, cancer nanotechnology researcher,

father and husband – he showed me everything he knew, exposed me to the careful link of boundary-pushing, disruptive research in the nanotech field merging with cancer therapeutics, with an understanding for the needs of the clinic. He demonstrated that passion, hard work, and love for one's work and family could intersect, and I'm eternally grateful for getting my start with him.

Chapter 1, in part, is a reformatted version of the published article as it appears in Lab on a Chip, Volume 14 (2014). The dissertation author was the primary investigator and author of this paper, and thanks co-authors Pranav Soman, John Warner, Peter H. Chung, and Dr. Shaochen Chen for their contributions. This work was supported by grants (EB012597 and EB017876) from the National Institute of Biomedical Imaging and Bioengineering and grants (CMMI-1130894, CMMI-1120795) from the US National Science Foundation.

Chapter 2, in full, is a reformatted version of the published article as appears in Advanced Functional Materials, Volume 24 (2014). The dissertation author was the primary investigator and author of this paper, and thanks co-authors Dr. Yu Suk Choi, Matthew G. Ondeck, Dr. Adam J. Engler, and Dr. Shaochen Chen for their contributions. This work was supported by the National Science Foundation (grants CMMI-1130894, CMMI-1332681), the National Institute of Health (NIH DP02 OD006460), and UCSD Neuroscience Microscopy Shared Facility Grant P30 NS047101.

Chapter 3, in full, has been submitted for publication of the material. The dissertation author was the primary investigator and author of this paper, and thanks co-authors Dr. Yu Suk Choi, Matthew G. Ondeck, Dr. Adam J. Engler, and Dr. Shaochen Chen for their contributions. This work was supported by the National Science

Foundation (grants CMMI-1130894, CMMI-1332681), the National Institute of Health (NIH DP02 OD006460), and UCSD Neuroscience Microscopy Shared Facility Grant P30 NS047101.

Chapter 4, in full, is a reformatted version of the published article as appears in Lab on a Chip, Volume 15 (2015). The dissertation author was the primary investigator and author of this paper, and thanks co-authors Dr. Darren Finlay, Xuanyi Ma, Dr. Xin Qu, Matthew G. Ondeck, Peter H. Chung, Fabian Zanella, Dr. Adam J. Engler, Dr. Farah Sheikh, Dr. Kristiina Vuori, and Dr. Shaochen Chen for their contributions. This work was supported by grants EB012597 and EB017876 from the NIH-National Institute of Biomedical Imaging and Bioengineering and grants CMMI-1332681 and CMMI-1120795 from the National Science Foundation (SC); the Saving tiny Heart Society and the California Institute of Regenerative Medicine (FS); ARRA grant (RC1 EB011780) from the NIH-National Institute of Biomedical Imaging and Bioengineering (KV); and DP020D006460 grant from the NIH (AJE).

Chapter 5, in part, is currently being prepared for submission for publication of the material. The dissertation author was the primary investigator and author of this paper, and thanks co-authors Dr. Amy Rommel, Dr. Inder Verma, and Dr. Shaochen Chen for their contributions. This work was supported by the National Institute of Health (grants HL053670 and EB017876), and The Leona M. and Harry B. Helmsley Charitable Trust (Award # 2012-PG-MED002).

VITA

2010	Bachelor of Science in Engineering, University of Pennsylvania
2011	Master of Science in Engineering, University of Pennsylvania
2011-2015	Research Assistant, Department of NanoEngineering University of California, San Diego
2015	Doctor of Philosophy, University of California, San Diego

FIELDS OF STUDY

Major Field: Bioengineering

Studies in Drug Delivery and Tissue Engineering
Professor Jason A. Burdick, Ph.D. (University of Pennsylvania)

Major Field: NanoEngineering

Studies in 3D printing and Tissue Engineering
Professor Shaochen Chen, Ph.D. (UC San Diego)

PUBLICATIONS

Hribar, K.C., Rommel, A., Verma, I. and Chen, S. "3D Bioprinted Tumor-Matrix Predicts Clinical Outcomes", *in preparation*

Hribar, K.C., Meggs, K., Liu, J., Qu, X. and Chen, S. "Three-dimensional cell patterning by ultrafast laser-induced degredation of collagen hydrogels", *submitted*

Hribar, K.C., Finlay, D., Ma, X., Qu, X., Ondeck, M.G., Chung, P.H., Zanella, F., Engler, A.J., Sheikh, F., Vuori, K. and Chen, S.C. "Nonlinear 3D Projection Printing of Concave Hydrogel Microstructures for Long-Term Multicellular Spheroid and Embryoid Body Culture" Lab on a Chip, Vol. 15, pp. 2412 - 2418, 2015

Wen, J.H., Vincent, L.G., Fuhrmann, A., Choi, Y.S., **Hribar, K.C.**, Taylor-Weiner, H., Chen, S. and Engler, A.J. "Interplay of matrix stiffness and protein tethering in stem cell differentiation" Nature Materials, Vol. 13, pp. 979 - 987, 2014

Hribar, K.C., Choi, Y.S., Ondeck, M.G., Engler, A.J. and Chen, S. "Digital Plasmonic Patterning for Localized Tuning of Hydrogel Stiffness" Advanced Functional Materials, Vol. 24, pp. 4922 - 4926, 2014

Hribar, K.C., Soman, P., Warner, J., Chung, P.H. and Chen, S. "Light-based Direct-write of 3D Functional Biomaterials" Lab on a Chip, Vol. 14, pp. 268 - 275, 2014

Zhang, A.P., Qu, X., Soman, P., **Hribar, K.C.**, Lee, J.W., Chen, S. and He, S. "Rapid Fabrication of Complex 3D Extracellular Microenvironments by Dynamic Optical Projection Stereolithography" Advanced Materials, Vol. 24, pp. 4266 – 4270, 2012

Lee, M.H., **Hribar, K.C.**, Brugarolas, T., Kamat, N.P., Burdick, J.A. and Lee, D. "Harnessing Interfacial Phenomena to Program the Release Properties of Hollow Microspheres" Advanced Functional Materials, Vol. 22, pp. 131 - 138, 2012

Ramanan, V.V., **Hribar, K.C.**, Katz, J.S. and Burdick, J.A. "Nanofiber-Nanorod Composites Exhibiting Light-Induced Reversible LCST Transitions" Nanotechnology, Vol. 22, pp. 494009, 2011

Hribar, K.C., Lee, M.H., Lee, D. and Burdick, J.A. "Enhanced Release of Small Molecules from Near-Infrared Light Responsive Polymer-Nanorod Composites" ACS Nano, Vol. 5, pp. 2948 - 2956, 2011

Charati, M.B., Lee, I., **Hribar, K.C.** and Burdick, J.A. "Light-sensitive Polypeptide Hydrogel and Nanorod Composites" Small, Vol. 6, pp. 1608 - 1611, 2010

Hribar, K.C., Metter, R.B., Ifkovits, J.L., Troxler, T. and Burdick, J.A. "Light-Induced Temperature Transitions in Biodegradable Polymer and Nanorod Composites" Small, Vol. 5, pp. 1830 - 1834, 2009

ABSTRACT OF THE DISSERTATION

Light-Assisted Biopatterning of Hydrogels for Investigating Cell Interactions within their Microenvironment

by

Kolin C. Hribar

Doctor of Philosophy in NanoEngineering

University of California, San Diego, 2015

Professor Shaochen Chen, Chair
Professor Liangfang Zhang, Co-Chair

Our bodies are composed of complex tissues and organs, and each tissue is governed by the careful coordination of cells, solutes, and extracellular matrix components. As such, the tissue engineering field has sought to develop tools to study tissue physiology at the molecular and cellular level. Biomaterials play a critical role in mimicking the extracellular matrix in design and function, acting as the scaffolding from which cells can attach, proliferate, and differentiate to form complex tissues. This dissertation focuses on light-assisted patterning of these materials for investigating cellular interactions within the tissue microenvironment.

The stiffness of the extracellular matrix has been implicated in governing cell fate (e.g. proliferation, migration, and differentiation) *in vivo*, thus we developed digital plasmonic patterning (DPP) – a laser-based patterning system – to control stiffness on a two-dimensional (2D) hydrogel substrate *in vitro*. Cells exhibited durotaxis, or migration to the stiffer patterns, as well as alignment onto the patterns. We built on this research by studying cellular migration in a three-dimensional (3D) collagen hydrogel. We used ultrafast laser-induced degradation (ULID) to spatially pattern channels (void spaces) in the collagen gel. Endothelial cells responded to the void spaces by migrating, aligning, and eventually forming tube-like structures similar to early blood vessel formation.

To enable the fabrication of more complex hydrogel structures, we turned to UV light-based 3D printing. First, we printed hydrogels with precise concave architectures and seeded breast cancer cells. Cells aggregated into spheroids over several days and developed hypoxic and necrotic cores by day 10, hallmarks of the tumor microenvironment. These results suggest a new way to study tumor progression. We furthered our study of cancer progression by developing a co-culture 3D printed *in vitro* model of glioblastoma (GBM) and its blood vessels. Results showed GBM proliferating, invading, and ultimately coopting the vasculature, and moreover demonstrated a similar response to FDA approved drugs as the clinical outcome.

In summary, we demonstrated the vast utility of light-assisted biopatterning for understanding cellular interactions in their microenvironment and later applied these methods to develop *in vitro* models for drug screening.

Chapter 1

Introduction

Tissue engineering refers to a broad field within the biomedical field that uses engineering tools to recreate the tissue microenvironment for diagnostic and therapeutic purposes [1–4]. Biomaterials are often used as the substrates or scaffolding on which cells attach, proliferate, and differentiate. The patterning of biomaterials and cellular components is thus critical to studying cellular interactions in their microenvironment as well as the development of more complex and biomimetic tissue engineered constructs.

Over the years, patterning techniques have been extensively developed for modulating cell behavior [1]. Micro-contact printing of proteins allows for the two-dimensional (2D) patterning of cells following protein deposition in a preconfigured design [5]. However, several studies have demonstrated that cells grown in 2D cultures display inconsistencies to physiological *in vivo* environment with respect to morphology, cell-cell and cell-ECM contacts, proliferation and differentiation [6].

More recently, researchers have sought to develop dynamic biomaterials and patterning methods for generating 3D multicellular environments that better mimic native tissue while permitting user controlled modification [7, 8]. Bioprinting, or biofabrication, platforms for these types of tissue engineered constructs have immense potential in generating more physiologically relevant tissue engineered constructs, enabling the investigation of fundamental biology, as well as the rapid screening of toxins, drugs, and ligands, in a more native, yet controllable micro/nano 3D environment [9–11].

3D biofabrication is primarily divided into two types: computer-assisted and process-directed techniques. Process-driven fabrication methods – those which do not utilize computer control or direct placement – include freeze-drying [12], salt leaching [13], electrospinning [14], porogen melting [15] gas foaming [16], and fiber deposition [17]. These methods allow control over bulk physical properties (e.g. material stiffness, swelling, etc.), however the resulting internal architecture is relatively uncontrolled. Computer-assisted direct-writing approaches, on the other hand, are capable of precisely dictating the internal architecture at the micro- and nanoscale, and thus facilitating greater control at the cellular and subcellular level.

Direct-writing techniques, typically referred to as free-form fabrication or rapid prototyping, are well suited to manufacture 3D scaffolds with orthogonal control over fabrication parameters [18, 19]. In most cases, a user-defined 3D structure is modeled using a computer software and broken down into a series of transverse-plane image slices. These slices are created as thin 2D layers for stacking in a layer-by-layer fashion (additive manufacturing), and a 3D scaffold is fabricated according to these image slices by translating either the computer-controlled stage or the deposition source in XYZ directions. Direct-writing allows the investigation of one or several biophysical parameters such as internal-architecture and mechanical properties. This approach also permits the use of a wide array of physiological components, such as biochemicals and encapsulated cells, in a modular fashion. Within the confines of direct-writing, the utility of light (e.g. laser or UV) offers a precise, rapid, and cost-effective way to fabricate and pattern bio-structures at the micro- and nanoscale. This chapter will discuss two light-assisted direct-write bioprinting platforms and applications of each: (A) projection

printing and (B) laser–based systems, in addition to highlighting some commonly used biomaterials.

1.1 Biomaterials

Numerous monomers and a selection of photoinitiators provide many permutations of materials for light-assisted fabrication systems [19]. Monomers of different chain lengths and chemical species at varying concentrations can be used to tune mechanical properties, porosity, and osmotic swelling of the resulting polymerized gels. Modulation of light intensity can also vary the degree of polymerization, additionally affecting these parameters. Though many conventional hydrogels such as agarose and polyacrylamide have been used in light-assisted printing, we will focus on three extensively-utilized, biocompatible, photocurable biomaterials which form hydrogels through free-radical photopolymerization: synthetic poly(ethylene glycol diacrylate) (PEGDA) [20, 21], and naturally-derived gelatin methyacrylate (GelMA) [22] and hyaluronic acid (HA) [23]. For a more complete list of polymers used in hydrogel fabrication, the reader is asked to consult the following references [24, 25].

PEGDA provides an excellent material for biomedical applications because of its high water content, biocompatibility and tunable mechanical properties [26]. Like many monomers, PEGDA may be synthesized at different molecular weights (typically 700-10,000 Da, in accordance to the number of polymer chains) and poly-distributions to generate polymerized gels of varying crosslinking densities and materials properties (e.g. stiffness, swelling, porosity). Moreover, multiple PEGDA monomers may be mixed at different concentrations to further alter the aforementioned material properties (e.g.

10kDa PEGDA mixed with 700Da PEGDA). Some synthetic materials like PEGDA are nondegradable, however chemical modification or mixing with other materials (e.g. DTT) may achieve a predictable degradation effect [27]. For cell seeding, PEG scaffolds require the grafting of adhesive peptide sequences (e.g. RGDS and YIGSR) or adhesive proteins (e.g. fibronectin and laminin).

Naturally derived hydrogels made from gelatin methacrylate (GelMA) have biologically active sequences that bind key integrins, enabling cells to adhere and migrate onto the structure [22, 28]. GelMA is generally a xenogenic modified macromer, therefore relatively inexpensive depending on the source and has the associated limitations *in vivo*. Hyaluronic acid (HA), a naturally occurring native ECM component and FDA-approved biomaterial, is a non-immunogenic polymer known to be important in wound healing. For instance, exogenous HA has been shown to reduce scar formation and promote regeneration in peripheral nerve injuries [23]. Since various biochemical moieties can be functionally introduced along the HA polymer backbone, a photopolymerizable form of HA has been created through the addition of methacrylate groups, termed glycidyl methacrylate-modified HA (GMHA). GMHA scaffold surfaces can be further modified to incorporate the cell-adhesive protein laminin. The library of photopolymerizable materials continues to expand with the development and modification of new and existing monomers/macromers, respectively, such as the aforementioned GMHA and GelMA, and thus light-assisted printing has the ability to work with an abundance of materials.

1.2 Projection Printing Systems

Digital mask (i.e. “maskless”) projection printing is a type of stereolithography which uses a digital micro-mirror device (DMD) found in conventional computer projectors to polymerize and solidify a photosensitive liquid prepolymer using either UV or other light sources [19, 21, 29-36]. Figure 1.1A shows a version of the maskless projection printing system called the dynamic optical projection stereolithography (DOPsL) platform [20, 21, 37-42]. The “maskless” or digital mask option allows for the use of controllable and interchangeable reflected light patterns rather than static, more expensive physical masks (such as those used in photolithography). The system spatially modulates collimated UV light using a DMD chip (1920 × 1080 resolution) to project custom-defined optical patterns onto a photocurable prepolymer solution. The DMD chip serves as an array of reflective coated aluminum micro-mirrors, capable of redirecting light to two states [0,1], tilted with two bias electrodes to form angles of either +12° or -12° with respect to the surface. Illumination from the light source reflects into the projection lens only when the micro-mirror is in its arbitrary “on” state. In the “off” state, the pixel appears dark as the illuminated light is reflected away from the projection lens.

To generate 3D structures, projection stereolithography platforms such as DOPsL employ a layer-by-layer fabrication procedure. Often, a 3D computer rendering (made with a CAD software or CT scans) is deconstructed into a series of evenly spaced planes,

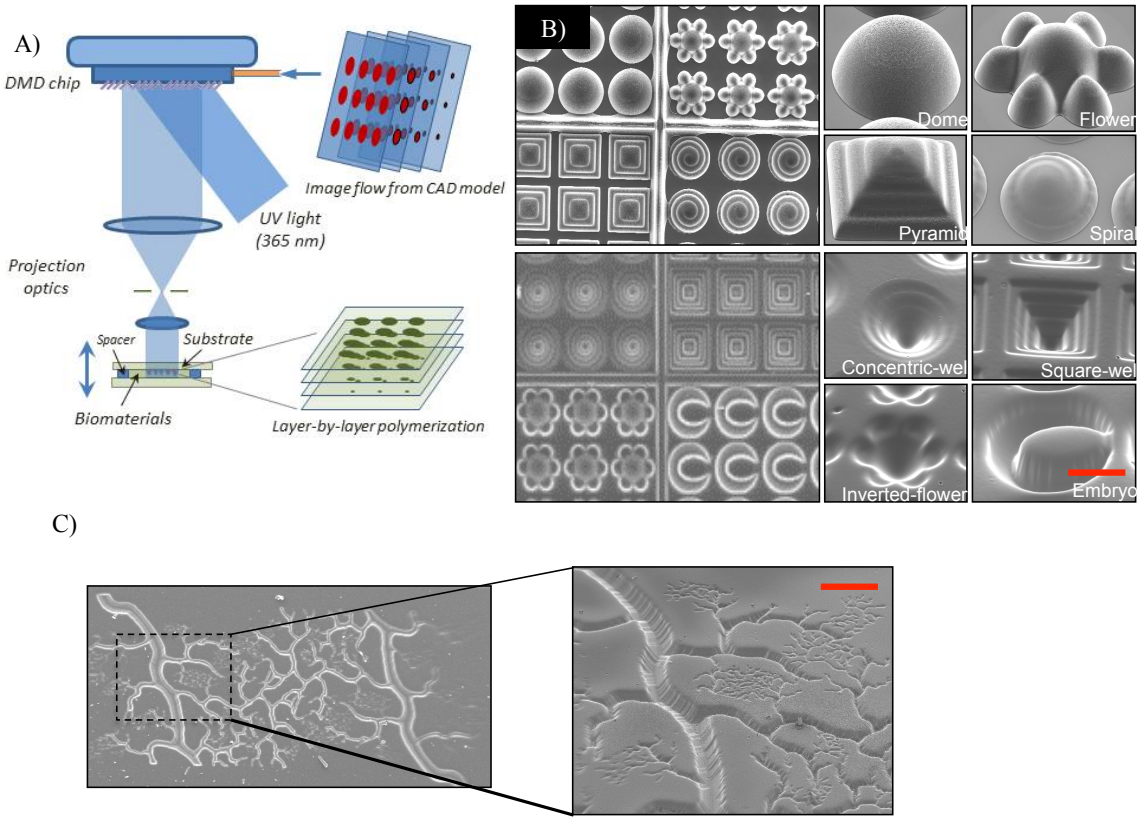

Figure 1.1: Projection Printing. A) Schematic of a projection printing setup called dynamic optical projection stereolithography (DOPsL): UV-light illuminates the DMD mirror system, which generates an optical pattern according to the image flow from the control computer. The optical pattern is projected through optical lens and onto the photosensitive biomaterial to fabricate a 3D scaffold in a layer-by-layer manner. **B**) SEM images of the concave and convex features (e.g. domes, microwells, etc.) using PEGDA demonstrating the versatility of the biofabrication system [41]. **C**) SEM image of a complex vasculature in PEGDA fabricated from a CAD file. Scale bar = 100 µm

or layers. The pattern for each layer is displayed on the DMD chip, exposing UV light onto the photcurable material. After one layer is patterned, the substrate is lowered using an automated stage and the next pattern is displayed. The user has control over the stage speed, intensity of the light, and height of the structure, allowing for the fabrication of various complex structures, such as spiral domes, pyramids and microwells (Figure 1.1B) [41]. Figure 1.1C demonstrates a complex vascular structure fabricated in PEGDA using this technology, another example of its versatility. As previously mentioned, mimicking the native tissue microenvironment with respect to architecture and material properties is key to the design of these 3D biostructures.

We will illustrate projection printing's increasing importance and utility in the tissue engineering field with several examples. From Gauvin et al., hydrogels comprised of GelMA were fabricated in 3D log-pile and hexagonal layered constructs (Figure 1.2A) [22]. Mechanical properties were varied by the geometry and prepolymer concentration (Figure 1.2B), and following, cell migration and proliferation into the scaffolds were monitored (Figure 1.2C). Log-pile and hexagonal structures displayed different moduli even when the prepolymer solution remained constant (10% GelMA). Importantly, the results from this study demonstrated the capability of the projection printing systems to generate cell-compatible scaffolds with tailored mechanical properties (by either varying prepolymer concentration or the micro-architecture). In another example, Lin et al. utilized projection printing to investigate cellular responses to varying scaffold porosities (Figure 1.3A) [34]. After encapsulating adipose-derived stem cells within the structures and incubating for seven days, an MTS assay reported a higher cell viability and activity of the cells in porous structures than in solid, non-porous structures (Figure 1.3B).

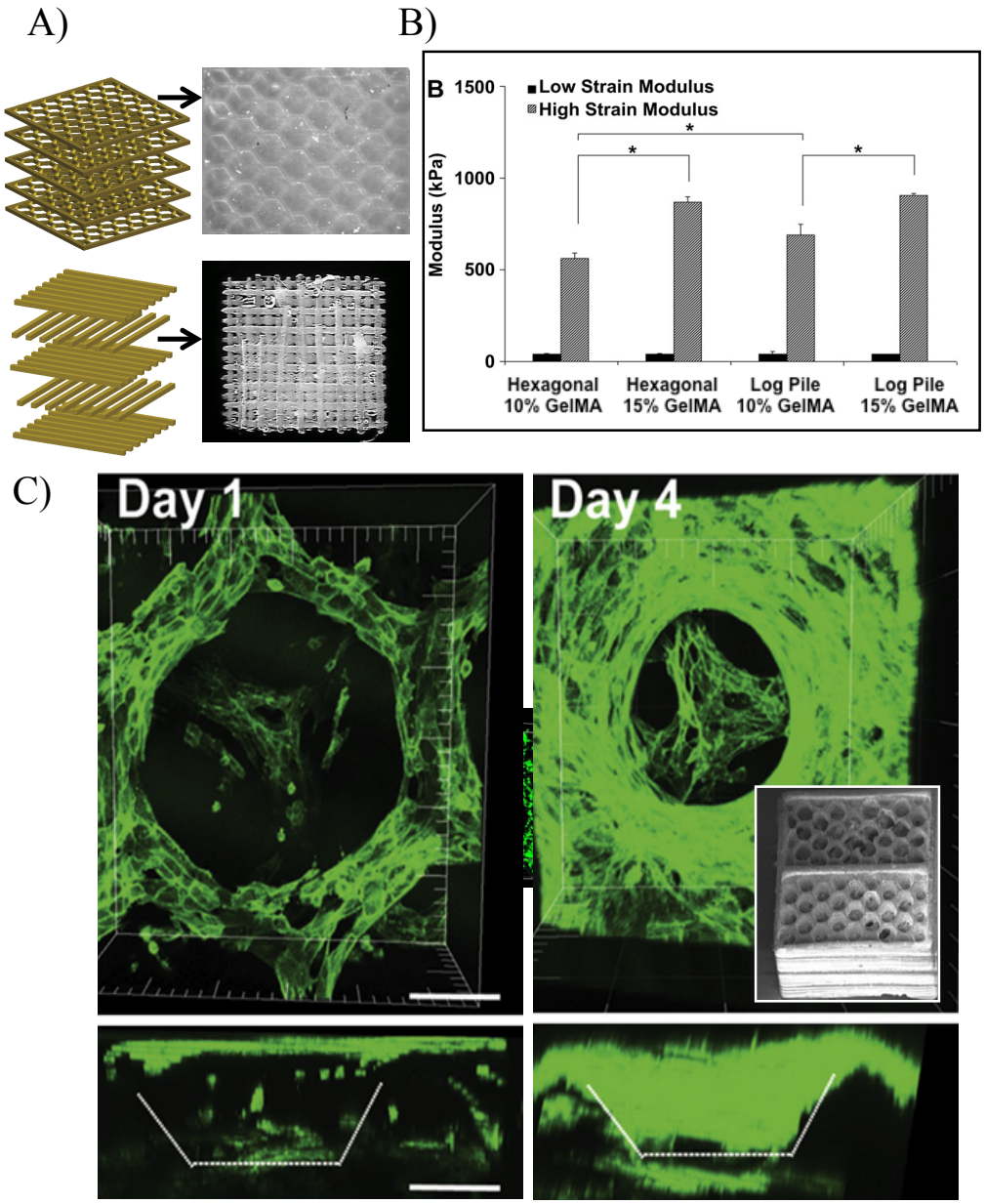

Figure 1.2: Layer-by-layer fabrication. A) Schematic shows layer-by-layer manufacturing of log-pile and hexagonal internal architecture. Optical images depict 3D scaffolds using GelMA biomaterial. **B**) Mechanical properties of scaffolds having hexagonal or log-pile structures using various GelMA percentages. Prepolymer concentration and engineered structures can be used to tailor the mechanical properties of the GelMA scaffolds. * indicates statistical significance ($p < 0.05$). **C**) 3D confocal images showing scaffold coverage by the HUVEC-GFP cells and cell penetration into the porous structure as a function of time; Inset: SEM image of hexagonal layered scaffold [22]. Scale = 100 μm

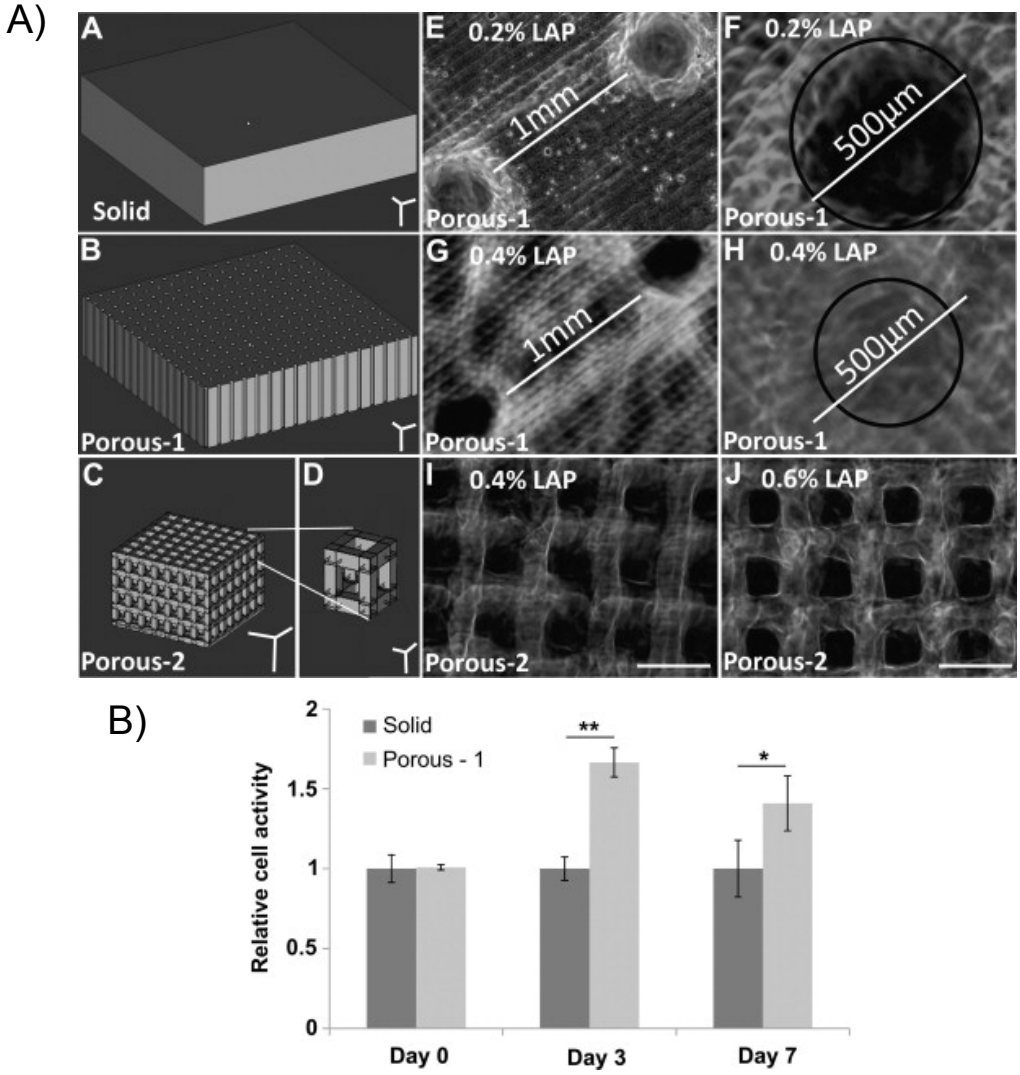

Figure 1.3: Examples of Stereolithography Fabrication A) 3D gels of varying porosity fabricated by projection stereolithography, with the CAD drawings and resulting internal architectures. Scale bar = 500 μm unless otherwise indicated. **B**) Relative cell activity assessed by MTS assay, using either solid or porous scaffolds [34].

Another parameter in tissue engineering – Poisson's ratio (PR) – has also been investigated using projection printing [39, 40, 42]. In general, the mechanical properties of a biomaterial scaffold can be quantitatively described by its elastic modulus and PR. Elastic modulus of the underlying substrate describes the material's elastic behavior during loading, while PR refers to the degree at which the scaffold contracts/expands in the transverse direction. Previously, research has extensively reported on the connection between a substrate's elastic modulus and cell response [43, 44]. PR has been less explored with conventional manufacturing approaches (e.g. annealing of polyurethane foams), because they offer little control over the microarchitecture [45, 46].

Light-assisted direct-writing, on the other hand, can provide precise control over this parameter. For instance, our lab used the DOPsL platform to fabricate unit-cell geometries for negative Poisson's ratio (NPR) (re-entrant structure, missing rib model) and zero Poisson ratio (ZPR) (semi-reentrant structure) scaffolds (Figure 1.4A). Figure 1.4B shows a structure undergoing tensile stress and expanding in the transverse direction, thereby demonstrating NPR. Analysis of the PR effect according to several unit-cells is documented in Figure 1.4C. Scaffolds exhibiting NPR (those which expand upon application of tensile stress) or ZPR may be more suitable for emulating the behavior of certain native tissues (e.g. expansion in blood vessels), and could be further investigated with projection printing.

These examples and others serve to demonstrate the versatility of projection printing systems in fabricating complex 3D structures of varying topographical features, mechanical properties, and porosity. Additionally, projection printing offers superior fabrication speeds (e.g. DOPsL fabricates within seconds) as compared to serial writing

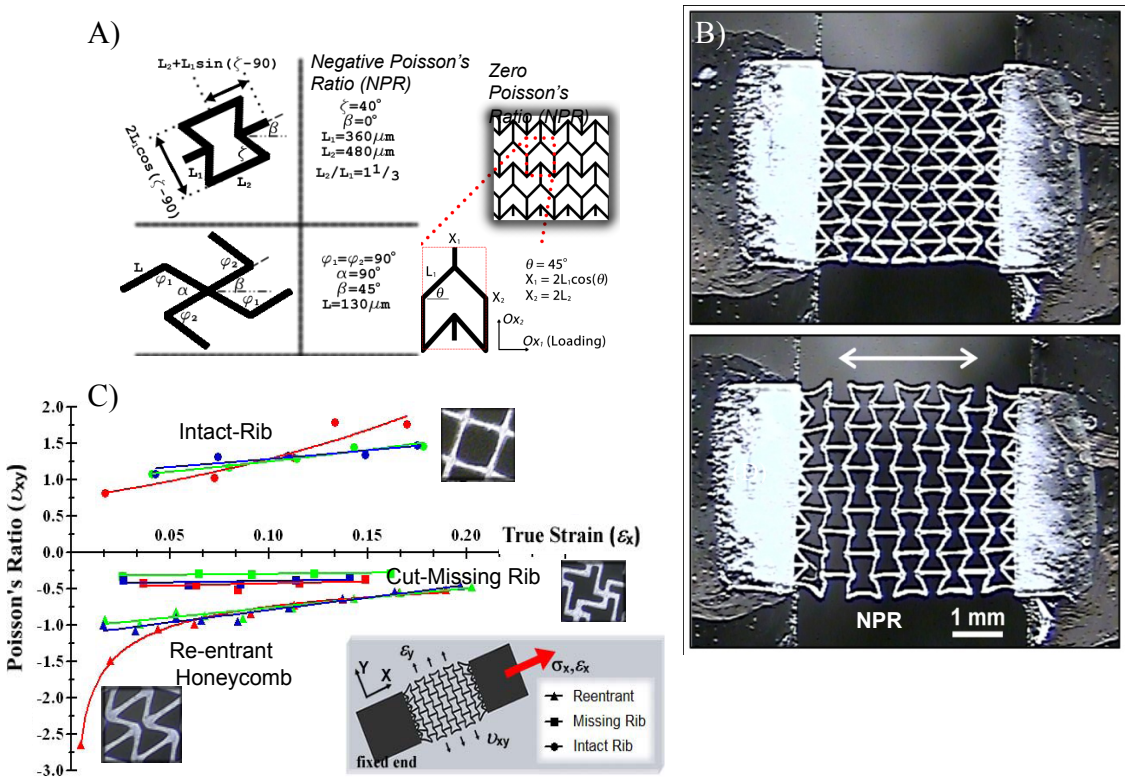

Figure 1.4: Exploring Poisson's Ratio with Scaffold Design A) Unit-cell parameters and relevant dimensional parameters of NPR (reentrant honeycomb, cut missing rib) and ZPR (semi-re-entrant) architectures. The walls of the unit-cells (denoted as ribs) are approximately 40 μm wide and 50-100 μm deep. **B**) PEGDA scaffolds with NPR expand with application of strain in X-axis (white arrow). Scale = 1 mm. **C**) Measured Poisson's ratio as a function of true strain for single-layer PEGDA scaffolds composed of the reentrant, missing-rib, and intact-rib (control) unit-cell geometries [42].

of two/multiple-photon polymerization [19, 41]. However, limitations include the resolution feature size (due to limitations of the projection lens and material swelling), the requirement of using photopolymerizable materials, and the effect of UV exposure to cells and photosensitive biomaterials [19, 47]. Improved optics will continue to enhance the resolution, and the expanding library of photopolymerizable materials will allow for increased scaffold complexity.

1.3 Laser-based techniques

Many of the concepts introduced with the projection-based systems, including material selection, geometry optimization, cell seeding and encapsulation design, also apply to the laser-based systems [18]. Historically, laser-based printing techniques such as laser-direct-writing [48, 49], laser-induced forward transfer (LIFT) [50], matrix-assisted pulsed laser evaporation (MAPLE) [51] etc., have been used to spatially pattern cells in 2D [52, 53], with limitations of low cell viability and throughput. Recently, 3D laser bioprinting has evolved to additive manufacturing (e.g. layer-by-layer) [54-56].

3D laser direct-writing incorporates a CAD model numerically sliced into a series of 2D layers, and fabricates 3D structures utilizing a motorized stage (controlled in XYZ) to manipulate the sample or laser (Figure 1.5A) [33, 57]. Laser-based fabrication differs from projection printing primarily in its light source [58-60], where a laser focused through an objective lens is used to crosslink and polymerize a liquid biopolymer. Writing width can be modulated and controlled by exposure energy – dictated by the beam size and laser power – and writing speed. After the first layer is crosslinked, the stage moves downward and a new layer of polymer is solidified according to the design.

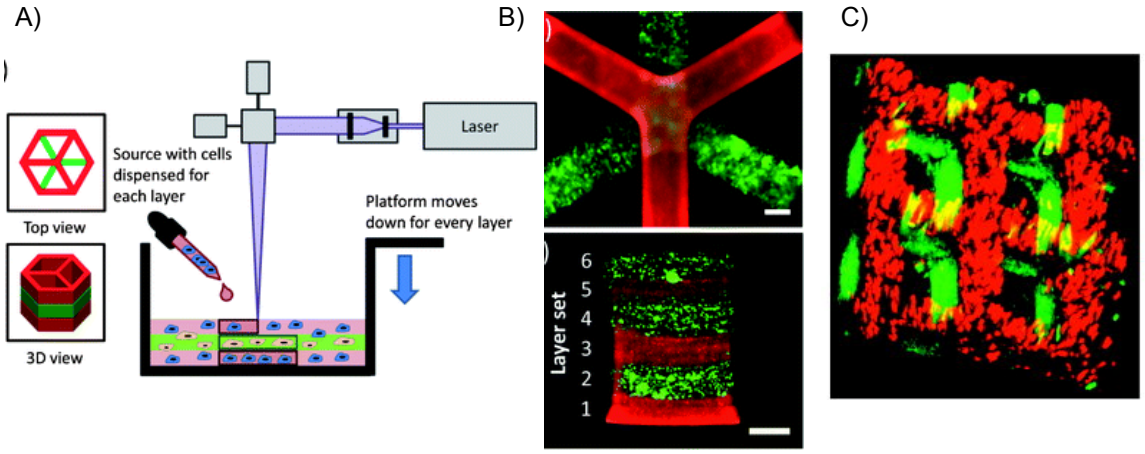

Figure 1.5: Laser Stereolithography of Biomaterial Structures A) Schematic of laser stereolithography using SLA (stereolithography apparatus) [57]. **B**) resulting SLA-fabricated 3D hydrogels with six layers [57]. Scale bars = 1 mm. **C**) spatially-patterned 3D scaffolds fabricated by laser-assisted stereolithography [61].

One such system, termed SLA (stereolithography apparatus), employs a focused single-photon UV laser to polymerize photocurable materials [57]. Chan et al. used SLA for generating controlled 3D structures to co-culture a heterogeneous cell distribution and assess long-term cell viability (Figure 1.5B). In a similar laser setup, Mapili et al. demonstrated a multilayer PEG hydrogel scaffold functionalized with heparin or RGD-peptide sequences for cell adhesion (Figure 1.5C) [61].

Two-photon polymerization (TPP) is another type of laser-based direct-writing which uses focused near-infrared (NIR) femtosecond laser pulses (wavelength ~ 800 nm) to trigger crosslinking of a photosensitive biomaterial [62]. In this fabrication technique, simultaneous absorption of two NIR photons generates free radicals to initiate the polymerization of volume-blocks (voxels) [63-65]. A distinct advantage of this system is the nonlinear nature of the laser-material interaction, achieving feature sizes below the diffraction limit of applied light. This process allows for better resolution at the expense of slower speeds and limited scalability (due to restrictions of the objective lens' working distance) compared to single photon polymerization (e.g. SLA) (Figure 1.6A). Figure 1.6B shows a typical TPP laser setup. In tissue engineering applications, TPP has been exploited to generate precise microscale biomaterial structures. For instance, in Figure 1.6C, TPP was used to fabricate a 3D log-pile structure (1 micron width lines) made of PEGDA with spacing of 8 μm. In another example, a gradient array of microdots (2-10 microns in diameter) were fabricated using a mixture of PEGDA and Cultrex 3-D Culture Matrix, a type of standardized basement membrane extract (Figure 1.6D) [66]. Lee et al. also demonstrated TPP fabrication of RGD-modified hydrogels to dictate cell migration

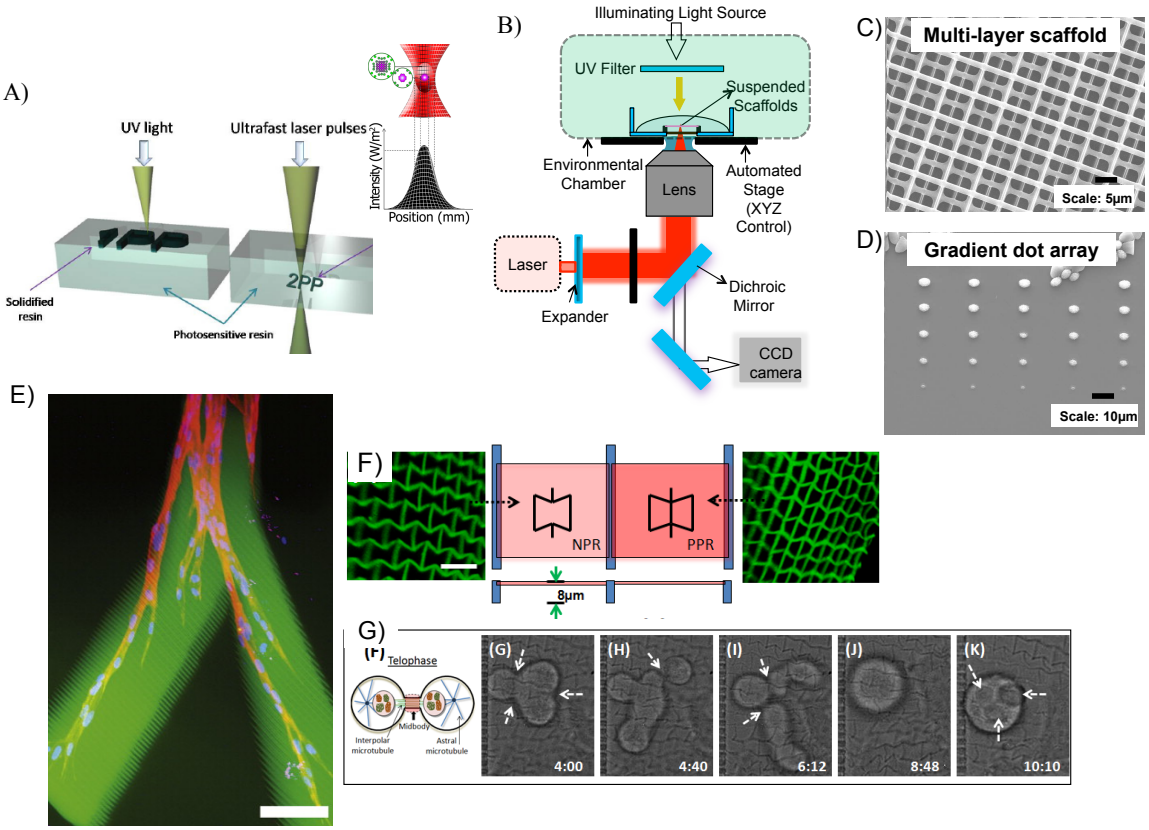

Figure 1.6: Laser-based Two-Photon Polymerization A) Principle of operation for single- and two-photon polymerization [69] **B**) Schematic of femtosecond laser fabrication set-up. **C**) Multi-layer log-pile scaffold with ~1 μm features [66]. **D**) gradient dot array at sub-micron resolution (the largest dot size ~4 μm, with spacing ~20 μm) fabricated by decreasing the laser-power from top to bottom. Biochemicals such as growth factors can be incorporated in these arrays [66]. **E**) 3D migration of cells within an RGD-modified PEG hydrogel, fabricated by TPP. (scale bar = 100 μm) [67] **F**) NPR and PPR structures patterned with TPP, and **G**) time-resolved single cell studies on an NPR structure (for details on this study, please refer to the reference) [68].

in 3D (Figure 1.6E) [67]. These examples demonstrate TPP's ability to chemically pattern and generate biostructures at cellular and subcellular scales.

Additionally, one can use TPP to explore the interaction of topographical features and single cell response. Similar to a study described in the projection printing section, Zhang et al. fabricated PEGDA-derived scaffolds exhibiting either NPR or PPR (negative or positive Poisson's ratio, respectively) (Figure 1.6F) [68]. Cell motility, orientation, and proliferation varied between NPR and PPR constructs, suggesting that PR plays a role in cell fate (Figure 1.6G); further tests are needed to promote this claim, however. Importantly, single cell studies are possible with TPP due to its high resolution of fabrication, compared to single photon or projection printing.

1.4 Summary

Both projection printing (e.g. DOPsL) and laser-based direct-writing systems (SLA, TPP) offer promising technologies to fabricate 3D bioconstructs with precise micro- and nano-architecture. Though these processes require photopolymerizable materials, the library of such materials continues to expand, accommodating for various scaffold properties (e.g. stiffness, porosity, swelling) in a 3D setting. Additionally, projection printing allows for the rapid printing of various complex structures, demonstrating its potential for high throughput screening. Though typically slower than projection printing (and SLA), TPP provides a high-resolution alternative to direct-writing for the fabrication of nanoscale features, and could play a significant role in single cell analysis in the years to come.

More interesting yet, combining several platforms such as projection printing and TPP could enable researchers to study a multitude of parameters in 3D. Light-assisted direct-writing could also compliment non-light-assisted direct-writing platforms (e.g. nozzle-based or extrusion systems) for generating precise nano/microscale features and chemical patterning within a larger scaffold. In the years ahead, we welcome the convergence of multiple printing technologies in the pursuit of growing physiologically relevant 3D tissue constructs *in vitro* (i.e. tissue-on-a-chip). Such *in vitro* biomimetic LOCs will enable us to more accurately answer basic cell biology questions and monitor various testing parameters (e.g. drug toxicity/discovery, (patho)physiology) prior to more expensive *in vivo* models.

The aims of this dissertation are (1) to use novel laser-based systems for patterning hydrogels, for understanding complex cellular interactions in their microenvironment on various substrates and 3D matrices, (2) to use 3D projection printing to develop *in vitro* models for understanding the cellular microenvironment in 3D, and (3) to develop a 3D printed tumor model for understanding tumor progression and response to clinically-relevant drugs.

Chapter 2 of this dissertation describes a new technique called digital plasmonic patterning (DPP) that alters a hydrogel substrate stiffness and studies the cellular interactions as a result of durotaxis. Chapter 3 builds on the technique from Chapter 2 and uses ultrafast laser-induced degradation (ULID) to pattern a collagen hydrogel in 3D. Cell migration, alignment and tube formation are noted as a result of the patterned channels (void spaces). Chapters 4 and 5 utilize a 3D projection printer for developing 3D cellular systems and studying tumor progression. Chapter 4 describes 3D printed

concave hydrogels for generating tumor spheroids and embryoid bodies, and shows their progression as representative of the *in vivo* environment. Chapter 5 describes a 3D printed co-culture angiogenesis model of glioblastoma and its vasculature, highlighting the tumor progression (invasion, vascular cooption) in response to various clinically-relevant drugs.

1.5 Acknowledgements

Chapter 1, in full, is a reformatted version of the published article as it appears in Lab on a Chip, Volume 14 (2014). The dissertation author was the primary investigator and author of this paper, and thanks co-authors Pranav Soman, John Warner, Peter H. Chung, and Dr. Shaochen Chen for their contributions. This work was supported by grants (EB012597 and EB017876) from the National Institute of Biomedical Imaging and Bioengineering and grants (CMMI-1130894, CMMI-1120795) from the US National Science Foundation.

1.6 References

1. A. Khademhosseini, R. Langer, J. Borenstein, J.P. Vacanti, *Proceedings of the National Academy of Sciences of the United States of America*, 2005, **103**, 2480.

2. P.X. Ma, *Advanced Drug Delivery Reviews*, 2008, **60**, 184.

3. R. Langer, J.P. Vacanti, *Science*, 1993, **260**, 920.

4. L.G. Griffith, G. Naughton, *Science*, 2002, **295**, 1009.

5. A. Bernard, J.P. Renault, B. Michel, H.R. Bosshard, E. Delamarche, *Advanced Materials*, 12, 2000, 1067.

6. A.J. Engler, M.A. Griffin, S. Sen, C.G. Bönnemann, H.L. Sweeney, D.E. Discher, *The Journal of Cell Biology*, 2004, **166**, 877.

7. A.M. Ghaemmaghami, M.J. Hancock, H. Harrington, J. Kaji, A. Khademhosseini, *Drug Discovery Today*, 2012, **17**, 173.

8. D.E. Ingber, G.M. Whitesides, Lab on a Chip, 2012, **12**, 2089.

9. M. Baker, *Nature*, 2011, **471**, 661.

10. D. Huh, Y.S. Torisawa, G.A. Hamilton, H.J. Kim, D.E. Ingber, *Lab on a Chip*, 2012, **12**, 2156.

11. I.R.-D. Jorge, Z. Bimeng, R. Daniel, S. Zhi-dong, X. Tao, *Biofabrication*, 2012, **4**, 035001.

12. F.J. O'Brien, B.A. Harley, I.V. Yannas, L. Gibson, *Biomaterials*, 2004, **25**, 1077.

13. S.B. Lee, Y.H. Kim, M.S. Chong, S.H. Hong, Y.M. Lee, *Biomaterials*, 2005, **26**, 1961.

14. X. Zong, H. Bien, C.-Y. Chung, L. Yin, D. Fang, B.S. Hsiao, B. Chu, E. Entcheva, *Biomaterials*, 2005, **26**, 5330.

15. A.S.P. Lin, T.H. Barrows, S.H. Cartmell, R.E. Guldberg, *Biomaterials*, 2003, **24**, 481.

16. R. Nazarov, H.-J. Jin, D. L. Kaplan, *Biomacromolecules*, 2004, **5**, 718.

17. L. Moroni, J.R. de Wijn, C.A. van Blitterswijk, *Biomaterials*, 2006, **27**, 974.

18. I. Antoniac, T. Billiet, M. Vandenhaute, J. Schelfhout, S. Vlierberghe, P. Dubruel, in *Biologically Responsive Biomaterials for Tissue Engineering*, Springer New York, 2013, pp. 201-249.

19. T. Billiet, M. Vandenhaute, J. Schelfhout, S. Van Vlierberghe, P. Dubruel, *Biomaterials*, 2012, **33**, 6020.

20. L. H. Han, G. Mapili, S. Chen, K. Roy, *J. Manuf. Sci. E–T. ASME*, 2008, **130**, 021005-1.

21. Y. Lu, G. Mapili, G. Suhali, S.C. Chen, K. Roy, *J Biomed Mater Res A*, 2006, **77A**, 396-405.

22. R. Gauvin, Y.-C. Chen, J. W. Lee, P. Soman, P. Zorlutuna, J. Nichol, S. C. Chen, A. Khademhosseini, *Biomaterials*, 2012, **33**, 3824-3834.

23. S. Suri, L.H. Han, W. Zhang, A. Singh, S.C. Chen, C. E. Schmidt, *Biomedical Microdevices*, 2011, **13**, 983.

24. K.T. Nguyen, J.L. West, *Biomaterials*, 2002, **23**, 4307.

25. J.L. Ifkovits, J.A. Burdick, *Tissue Eng*, 2007, **13**, 2369.

26. B. Baroli, *Journal of Pharmaceutical Sciences*, 2007, **96**, 2197.

27. G.A. Hudalla, T.S. Eng, W.L. Murphy, *Biomacromolecules*, 2008, **9**, 842.

28. A.I. Van Den Bulcke, B. Bogdanov, N. De Rooze, E.H. Schacht, M. Cornelissen, H. Berghmans, *Biomacromolecules*, 2000, **1**, 31.

29. J.-W. Choi, R. Wicker, S.-H. Lee, K.-H. Choi, C.-S. Ha, I. Chung, *Journal of Materials Processing Technology*, 2009, **209**, 5494.

30. A.D. Lantada, P.L. Morgado and J. Stampfl, in *Handbook on Advanced Design and Manufacturing Technologies for Biomedical Devices*, Springer US, 2013, pp. 181-205.

31. T.J. Horn, O.L. A. Harrysson, *Science Progress*, 2012, **95**, 255.

32. S.D. Gittard, R.J. Narayan, *Expert Review of Medical Devices*, 2010, **7**, 343.

33. A. Waldbaur, H. Rapp, K. Lange, B.E. Rapp, *Analytical Methods*, 2011, **3**, 2681.

34. H. Lin, D. Zhang, P.G. Alexander, G. Yang, J. Tan, A.W. Cheng, R.S. Tuan, *Biomaterials*, 2013, **34**, 331.

35. R. Liska, M. Schuster, R. Inführ, C. Turecek, C. Fritscher, B. Seidl, V. Schmidt, L. Kuna, A. Haase, F. Varga, H. Lichtenegger, J. Stampfl, *Journal of Coatings Technology and Research*, 2007, **4**, 505.

36. L.H. Han, G. Mapili, S. Chen, K. Roy, *J. Manuf. Sci. E–T. ASME*, 2008, **130**, 021005.

37. P. Soman, J.A. Kelber, J.W. Lee, T.N. Wright, K.S. Vecchio, R.L. Klemke, S. Chen, *Biomaterials*, 2012, **33**, 7064.

38. P. Soman, B.T. D. Tobe, J.W. Lee, A. Winquist, I. Singec, K.S. Vecchio, E.Y. Snyder, S. Chen, *Biomedical Microdevices*, 2012, **14**, 829.

39. P. Soman, D.Y. Fozdar, J.W. Lee, A. Phadke, S. Varghese, S. Chen, *Soft Matter*, 2012, **8**, 4946.

40. P. Soman, J.W. Lee, A. Phadke, S. Varghese and S. Chen, *Acta Biomaterialia*, 2012, **8**, 2587.

41. A.P. Zhang, X. Qu, P. Soman, K.C. Hribar, J.W. Lee, S. Chen, S. He, *Advanced Materials*, 2012, **24**, 4266.

42. D.Y. Fozdar, P. Soman, J.W. Lee, L.H. Han, S. Chen, *Advanced functional materials*, 2011, **21**, 2712.

43. D.E. Discher, P. Janmey and Y.-l. Wang, *Science*, 2005, **310**, 1139-1143.

44. A.J. Engler, S. Sen, H.L. Sweeney, D.E. Discher, *Cell*, 2006, **126**, 677.

45. R.H. Baughman, S. Stafstram, C. Cui, S.O. Dantas, *Science*, 1998, **279**, 1522.

46. R. Lakes, *Science*, 1987, **235**, 1038.

47. A. Khademhosseini, R. Langer, *Biomaterials*, 2007, **28**, 5087.

48. D.J. Odde, M.J. Renn, *Biotechnology and Bioengineering*, 2000, **67**, 312.

49. L. Koch, M. Gruene, C. Unger, B. Chichkov, *Current Pharmaceutical Biotechnology*, 2013, **14**, 91.

50. R.S. Nathan, T.C. David, H. Yong, R. Nurazhani Abdul, X. Yubing, B.C. Douglas, *Biofabrication*, 2010, **2**, 032001.

51. P.K. Wu, B.R. Ringeisen, J. Callahan, M. Brooks, D.M. Bubb, H.D. Wu, A. Piqué, B. Spargo, R.A. McGill, D.B. Chrisey, *Thin Solid Films*, 2001, **398-399**, 607.

52. A. Doraiswamy, R.J. Narayan, M.L. Harris, S.B. Qadri, R. Modi, D.B. Chrisey, *Journal of Biomedical Materials Research Part A*, 2007, **80A**, 635.

53. M.O. Christina, W. Xingjia, J.A. Juanita, R.R. Bradley, *Biomedical Materials*, 2008, **3**, 034101.

54. M. Gruene, M. Pflaum, C. Hess, S. Diamantouros, S. Schlie, A. Deiwick, L. Koch, M. Wilhelmi, S. Jockenhoevel, A. Haverich, B. Chichkov, *Tissue Eng C Meth*, 2011, **17**, 973.

55. L. Koch, A. Deiwick, S. Schlie, S. Michael, M. Gruene, V. Coger, D. Zychlinski, A. Schambach, K. Reimers, P.M. Vogt and B. Chichkov, *Biotechnology and Bioengineering*, 2012, **109**, 1855.

56. R.K. Pirlo, P. Wu, J. Liu and B. Ringeisen, *Biotechnology and Bioengineering*, 2012, **109**, 262.

57. V. Chan, P. Zorlutuna, J.H. Jeong, H. Kong and R. Bashir, *Lab on a Chip*, 2010, **10**, 206.

58. F.P.W. Melchels, J. Feijen, D. W. Grijpma, *Biomaterials*, 2010, **31**, 6121.

59. D.W. Hutmacher, M. Sittinger, M.V. Risbud, *Trends in biotechnology*, 2004, **22**, 354.

60. A. Ovsianikov, M. Gruene, M. Pflaum, L. Koch, F. Maiorana, M. Wilhelmi, A. Haverich, B. Chichkov, *Biofabrication*, 2010, **2**, 014104.

61. G. Mapili, Y. Lu, S.C. Chen, K. Roy, *Journal of Biomedical Materials Research Part B-Applied Biomaterials*, 2005, **75B**, 414.

62. M. Gebinoga, J. Katzmann, U. Fernekorn, J. Hampl, F. Weise, M. Klett, A. Läffert, T.A. Klar, A. Schober, *Engineering in Life Sciences*, 2013, **13**, 368.

63. R. Landers, A. Pfister, U. Hubner, H. John, R. Schmelzeisen, R. Mulhaupt, *J Mater Sci*, 2002, **37**, 3107.

64. A. Ovsianikov, A. Deiwick, S. Van Vlierberghe, P. Dubruel, L. Moller, G. Dralger, B. Chichkov, *Biomacromolecules*, 2011, **12**, 851.

65. E.T. Ritschdorff, J.B. Shear, *Analytical Chemistry*, 2010, **82**, 8733.

66. W. Zhang, S.C. Chen, in *MRS Bulletin*, 2011, pp. 1028-1033.

67. S.H. Lee, J.J. Moon, J. L. West, *Biomaterials*, 2008, **29**, 2962.

68. W. Zhang, P. Soman, K. Meggs, X. Qu, S. Chen, *Advanced Functional Materials*, 2013, **23**, 3226.

69. S. Wu, J. Serbin, M. Gu, *Journal of Photochemistry and Photobiology A: Chemistry*, 2006, **181**, 1.

Chapter 2

Digital Plasmonic Patterning for Localized Tuning of Hydrogel Stiffness

Abstract

The mechanical properties of the extracellular matrix (ECM) can dictate cell fate in biological systems. In tissue engineering, varying the stiffness of hydrogels – water-swollen polymeric networks that act as ECM substrates– has previously been demonstrated to control cell migration, proliferation, and differentiation. Here, we developed "digital plasmonic patterning" (DPP) to mechanically alter a hydrogel encapsulated with gold nanorods using a near-infrared laser, according to a digital (computer-generated) pattern. DPP can provide orders of magnitude changes in stiffness, and can be tuned by laser intensity and speed of writing. *In vitro* cellular experiments using A7R5 smooth muscle cells confirm cell migration and alignment according to these patterns, making DPP a useful technique for mechanically patterning hydrogels for various biomedical applications.

2.1 Introduction

Patterning biomaterials in a controlled, systematic fashion is a focal point in the fields of tissue engineering and more broadly biomedical research [1-3]. The engineering of heterogeneous material properties can instigate a complex cellular response, better mimicking the complexity of tissue *in vivo* [4, 5]. Specifically, mechanics of the extracellular matrix have been demonstrated to play a pivotal role in governing cell fate [6-8]. For instance, soft (~1 kPa) versus stiff (>30 kPa) materials can dictate adipogenic or osteogenic lineages in stem cell differentiation, respectively [9]. Additionally, it has been shown that stiff materials provide enhanced traction for cell motility, compared to soft substrates [10]. Consequently, adhesive cells preferably migrate toward stiffer substrates by focal adhesion polarization when exposed to a stiffness gradient. This phenomenon is called durotaxis and is observed in many cell cultures including smooth muscle cells and stem cells [8, 11, 12]. The design of biomaterials with tunable mechanical properties is thus central to tissue engineering, and can facilitate cell migration, proliferation, and differentiation.

In this chapter, we describe a new patterning technique called “digital plasmonic patterning” (DPP) to alter mechanical properties of a polymeric hydrogel. Gold nanorods within a loosely crosslinked poly(ethylene glycol) (PEG) hydrogel matrix absorb a focused laser to generate heat and thermally crosslink the network further. A femtosecond near-infrared (NIR) laser beam (pulse width = 100 femtoseconds, wavelength = 800 nm, 80 MHz) passes through an objective lens onto a motorized microscope stage and the stage moves according to a digital (computer-generated)

pattern. Atomic force microscopy (AFM) is used to assess stiffness profiles on the hydrogel substrate. Changes in both light intensity and speed of writing can alter the crosslinking (and accompanying stiffness increase) of the matrix. We then assess cellular response to the patterned stiffness, demonstrating a high degree of cell migration and alignment to the patterns.

Previously, other fabrication techniques have been used to pattern mechanical changes in hydrogels, such as photolithography [8, 13]. However, multiple materials and hard masks are a requirement of these types of processes, in addition to clean room conditions. Here, DPP can enhance a hydrogel's stiffness on the same gel template (with no additional materials), in a highly tunable fashion and without the requirement of a physical mask or clean room. DPP represents a potentially useful tool in locally tuning the mechanical properties of hydrogels for biomedical applications.

2.2 Materials and Methods

2.2.1 Materials

For gold nanorod synthesis and modification, hydrochloroauric acid ($HAuCl_4$), silver nitrate ($AgNO_3$), sodium borohydride, and L-ascorbic acid were purchased from Sigma-Aldrich and cetyltrimethylammonium bromide (CTAB) was purchased from CalBioChem (EMD Millipore). Milli-Q water (18.2 Ω, MilliPore) was used in all synthesis steps. mPEG-thiol (5 kDa) (Nanocs) was used in nanorod surface modification. For pre-polymer solution, poly(ethylene glycol)diacrylate (PEGDA) (575 Da, Sigma), Milli-Q H_2O (Milli-Pore), and lithium phenyl-2,4,6-trimethylbenzoylphosphinate (LAP)

photoinitiator [14] were used. Acryloyl-PEG-RGDS was synthesized according to previous protocols [15].

2.2.2 Digital Plasmonic Patterning

Hydrogels patterned by DPP were made in a two-step polymerization process. First, a prepolymer solution was photopolymerized with UV light, creating a partially polymerized hydrogel network. Second, a focused NIR laser was used to crosslink the network further. Gold nanorods (average length = 33.2 ± 3.0 nm, width = 9.5 ± 1.1 nm, aspect ratio = 3.5 ± 0.5) were synthesized according to a general wet chemical synthesis and surface modified with PEG-SH to reduce cytotoxicity [16, 17]. A prepolymer solution was made consisting of 9% (v/v) poly(ethylene glycol) diacrylate (MW 575 Da), 1 nM gold nanorods, and 0.05% (w/v) LAP photoinitiator in diH_2O. The solution was pipetted between two glass slides and a cover slip spacer (#1 thickness, Chemglass), where one side was methacrylated glass for chemical linkage to the hydrogel and the other side was coated with dichlorodimethylsilane (DCDMS), a hydrophobic monolayer to allow easy hydrogel removal. The solution was exposed to UV light (350 nm, 4.5 mW cm^{-2}, UVP) for 10 or 12 seconds to produce partially crosslinked gels with stiffness measurements of 7 kPa or 17 kPa, respectively. Gels were incubated in diH_2O for several days to remove any unreacted materials from the gel, then placed on a glass coverslip with 25 µl fresh diH_2O and secured to an automatic stage atop an inverted microscope. Patterning via DPP occurred when a femtosecond laser beam (800 nm, 80 MHz, Coherent) was focused through the laser objective lens (10x, NA 0.45) and onto the gel sample. Patterns were drawn according to a digital mask designed on the computer and relayed to the stage controller (MS2000, ASI) for controlled writing speed (mm/s).

2.2.3 AFM Analysis: Mechanical and Topographical Testing

Stiffness of the hydrogel was confirmed by atomic force microscopy (AFM; MFP3D, Asylum Research) as detailed previously [8, 18]. Briefly, a pyramidal probe, 0.08 N m^{-1} spring constant with a 35° half angle (PNP-TR20, Nanoworld), was used to indent a substrate every 10 μm in triplicate over two repeats of the low/high pattern stripes. The probe indentation velocity was fixed at 2 μm/s with the trigger force of 2 nN. Elastic modulus maps were determined by the Hertz cone model with a sample Poisson ratio of 0.5 fit over a range of 10%-90% indentation force [18]. Surface height is also simultaneously computed based on when probe deflection occurs as it indents the material. AFM software (Igor pro 6.22) was applied to generate the stiffness and analyze height data.

2.2.4 *in Vitro* Cell Studies

Prepolymer solution was modified with 2.5 mM acryloyl-PEG-RGDS prior to the first crosslinking step to facilitate cell attachment to the hydrogels. Gels were patterned by DPP with 80 mW of laser power and 1.0 mm s^{-1} writing speed, and were subsequently exposed to 2% Penn/strep in PBS for several days in a 24-well plate followed by 1hr of UV-exposure (cell culture hood) for sterilization. A7R5 smooth muscle cells were cultured in Dulbecco's Modified Eagle's Medium with 10% FBS, trypsinized, and seeded at a cell density of 25,000 cells mL^{-1} into each well. Media was exchanged every two days. Images were captured at various timepoints (up to six days) using DIC microscopy. Cells were fixed on day 6 with 4% paraformaldehyde and stained for actin and nuclei with rhodamine phalloidin and DAPI fluorescent dyes, respectively. Fluorescent images

were captured with a Leica fluorescent microscope and analyzed for cell distributions and alignment (determined by the long axis of the nuclei) using ImageJ computer software.

2.3 Results and Discussion

2.3.1 The DPP Platform: a Two-Step Polymerization Process

Hydrogels patterned using DPP technology were fabricated in a two-step polymerization process (Figure 2.1A). In the first step, a loosely-crosslinked hydrogel was made by UV photopolymerization. A prepolymer solution – consisting of 9% (v/v) PEG diacrylate (PEGDA) (MW 575 Da), 0.05% (w/v) LAP photointiator, 1 nM gold nanorods, and diH_20 – was administered between glass coverslips and exposed to a UV light source (350 nm, 4.5 mW cm^{-2}) for various times (see methods for details). The UV light permits free radical polymerization through conversion of the acrylate double bonds on the PEG monomer. DPP represents the second step of polymerization. Highlighting its digital nature, a computer-generated design was applied to the stage controller and patterned within a few minutes on the hydrogel substrate (depending on the fabrication parameters and scale of the design). The resulting pattern was visualized under brightfield microscopy without the requirement of any fluorescent tags or external labeling techniques. The darker regions can be attributed to higher material density due to DPP crosslinking of the network.

The mechanism of crosslinking during the two-step polymerization process is illustrated in Figure 2.1B. We anticipate only partial acrylate conversion in the first step thereby producing a “partially-crosslinked” soft gel that serves as a template for further

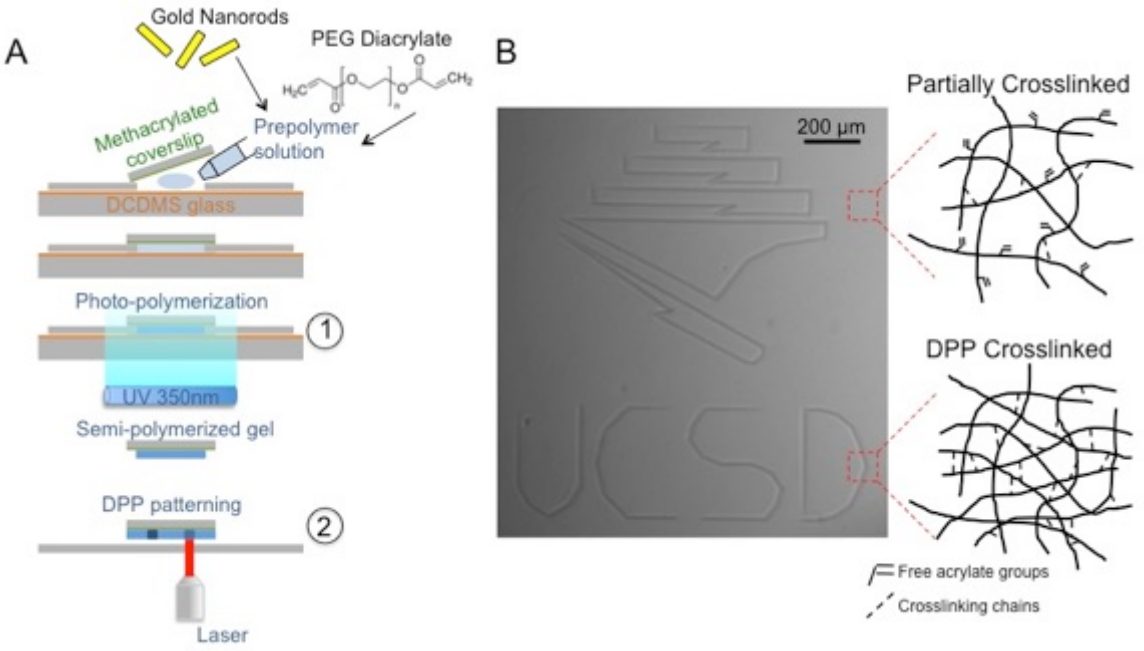

Figure 2.1: General Process of DPP. A) Two-step process of making patterned hydrogels, with the outset showing the prepolymer constituents (gold nanorods and PEG diacrylate). A partially-crosslinked network is photopolymerized under UV light (1), followed by DPP patterning using a focused NIR laser (2), causing further crosslinking to take place. **B**) Digital image patterned onto the hydrogel substrate, and mechanism of crosslinking illustrated.

mechanical patterning. We conjecture that DPP drives conversion of the remaining free acrylate bonds due to thermal crosslinking, in addition to possible physical entanglements of the PEG chains.

PEG hydrogels have traditionally been utilized in tissue engineering research for their biocompatibility, high water retention, low immunogenicity and strong molecule transport [19, 20]. Additionally, PEG can be easily functionalized with cell adhesion peptides (e.g. RGD) and synthesized with a range of molecular weights and crosslinking arms, allowing for a variety of material properties tailored to a specific application and design. In this research project, while we explored relatively high-molecular weight PEGs (e.g. 10 kDa), we ultimately chose a low-molecular weight PEGDA (575 Da) to limit hydrogel swelling after the first step of polymerization and encourage thermal crosslinking in the subsequent DPP step.

During DPP, gold nanorods embedded in the hydrogel matrix were photothermally excited by a femtosecond NIR laser to mechanically pattern the substrate. The laser was directed through the objective lens (10x, NA = 0.45) and onto a motorized microscope stage where the laser beam is focused onto the sample. Based on microscopic inspection, we concluded the beam size was around ~40-50 μm in diameter and exhibited a Gaussian distribution. The beam size is a limitation of our setup, though presumably this could be further narrowed with higher magnification systems that produce a more focused laser beam. Importantly, the laser wavelength (800 nm) coincided with the longitudinal surface plasmon peak of the gold nanorods, allowing for their plasmonic enhancement (Figure 2.2). It has been well documented that gold nanorod absorption at

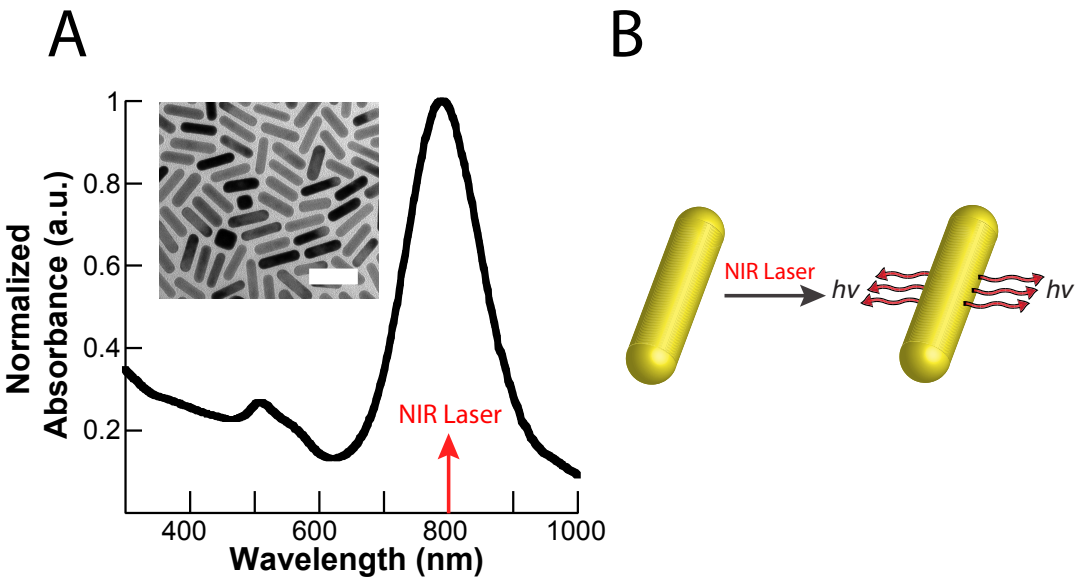

Figure 2.2: Plasmonic enhancement of gold nanorods. A) Absorbance of aqueous gold nanorod solution in relation to the laser wavelength (inset: transmission electron microscopy image of gold nanorods, scale bar = 50 nm). **B**) Mechanism of the photothermal effect, where the nanorods absorb near-infrared light at their surface plasmon resonance (800 nm) to produce a thermal output.

their plasmon resonance produces a photothermal effect due to excitable electrons on the nanoparticle surface, releasing energy in the form of phonons [21, 22]. Due to this photothermal crosslinking event, we performed the DPP step prior to any cell seeding to prevent cellular damage, a limitation of the current fabrication design.

2.3.2 Surface Topography and Mechanical Characterization

It was important to verify whether the nanorods themselves contributed to topographical features on the hydrogel substrate, which could potentially affect cell responses. AFM was used to assess the surface topography and the results are shown in Figure 2.3. The surface appears smooth across samples with and without nanorods, confirming that gold nanorods did not contribute to the surface nanotopography.

Figure 2.4 depicts the AFM mechanical testing of DPP hydrogel substrates. We fabricated hydrogels with a baseline stiffness of 17 kPa for mechanical patterning, though this value could be adjusted by the time of UV exposure during the first polymerization step. Laser intensity was tuned using a polarizer to achieve either 80 mW or 100 mW of average power and writing speeds were set to 1.0, 1.5 or 2.0 mm s^{-1} by a motorized stage controller. Figure 2.4A shows a microscope image of the AFM tip over the DPP stiffened regions of the hydrogel (darkened regions). Interestingly, both writing speed and laser intensity determined the degree to which the hydrogel stiffened. For instance, DPP writing criteria of 80 mW : 1.0 mm s^{-1}, 80 mW : 1.5 mm s^{-1}, 80 mW : 2.0 mm s^{-1} and 100 mW : 2.0 mm s^{-1} produced stiffness peaks of 350 ± 12 kPa, 65 ± 6 kPa, 35 ± 3 kPa, and 79 ± 11 kPa, with topographical changes of -4.1 ± 0.1 μm, -0.7 ± 0.2 μm, -1.2 ± 0.1 μm, and -1.37 ± 0.0 μm, respectively (Figure 2.4B-D). We explored another baseline stiffness of 7 kPa and the results appear in Figure 2.5. In both cases, it was observed that

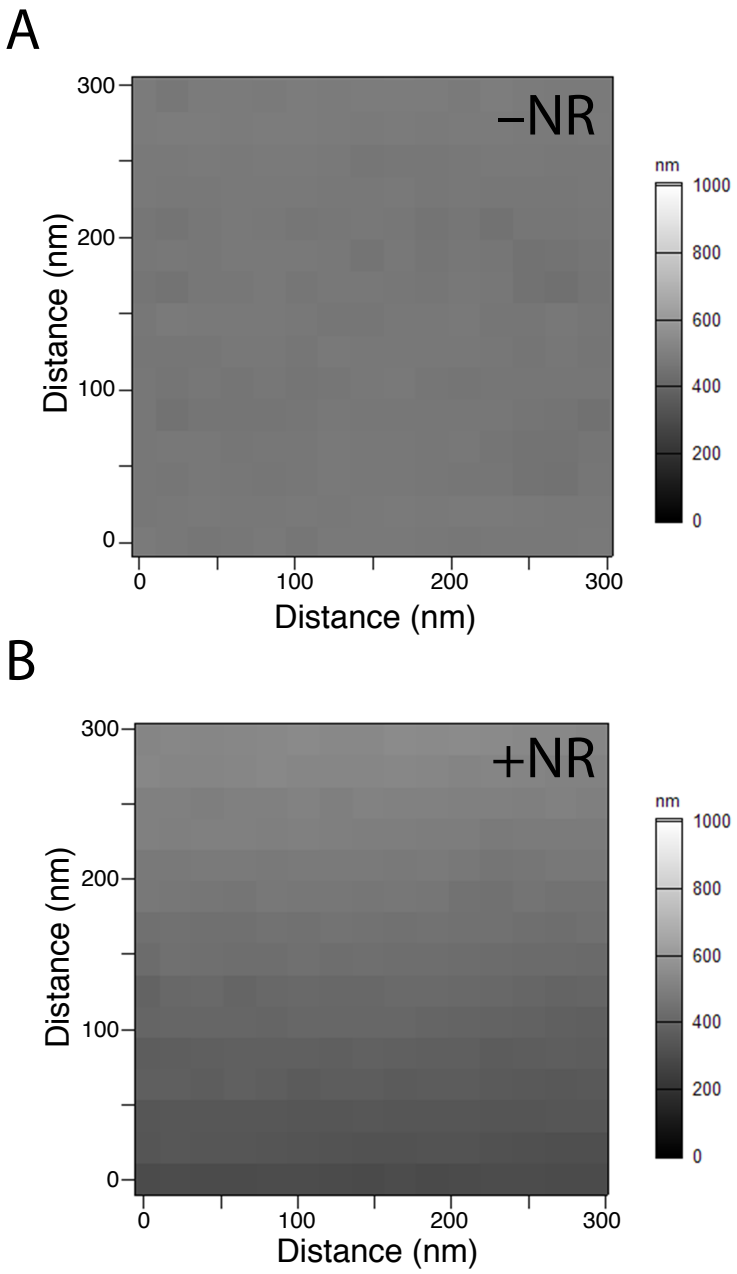

Figure 2.3: Surface nanotopography of PEG hydrogels A) without and **B)** with gold nanorods, at a constant stiffness.

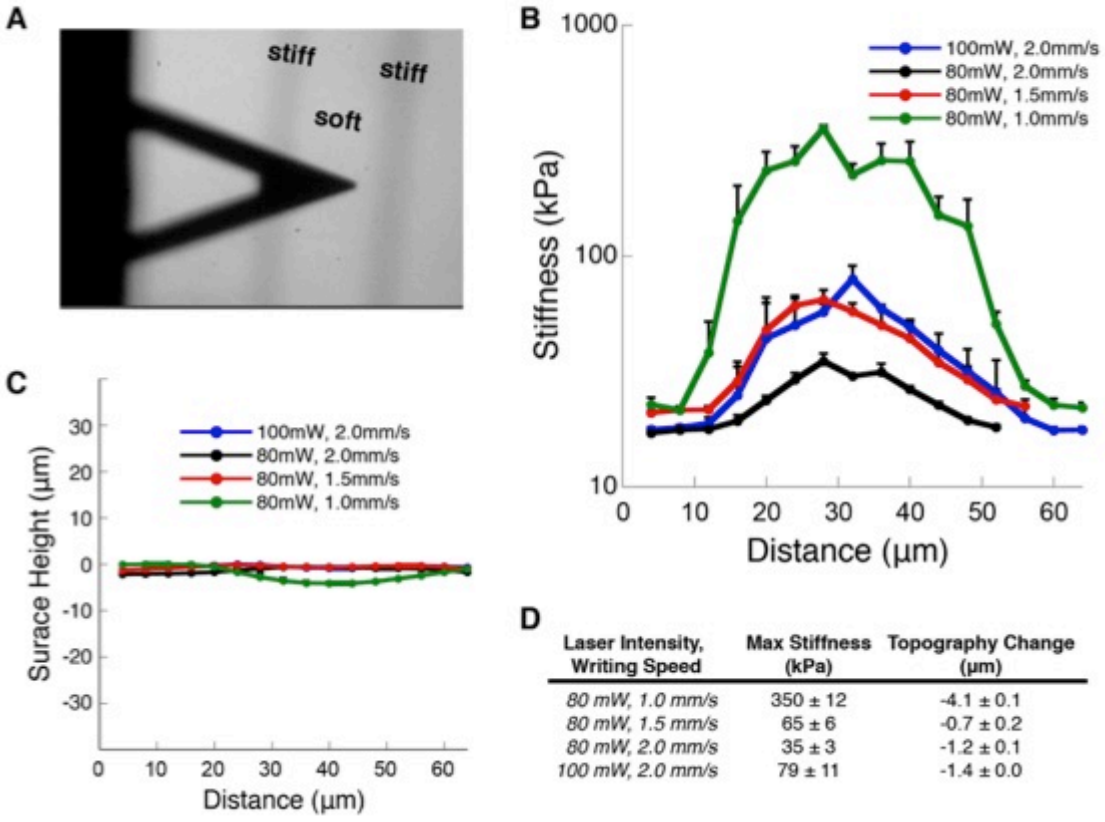

Laser Intensity, Writing Speed	Max Stiffness (kPa)	Topography Change (µm)
80 mW, 1.0 mm/s	350 ± 12	-4.1 ± 0.1
80 mW, 1.5 mm/s	65 ± 6	-0.7 ± 0.2
80 mW, 2.0 mm/s	35 ± 3	-1.2 ± 0.1
100 mW, 2.0 mm/s	79 ± 11	-1.4 ± 0.0

Figure 2.4: AFM Characterization. A) AFM tip over a patterned hydrogel substrate. AFM analysis of **B**) mechanical and **C**) topographical changes associated with DPP areas on hydrogel with various laser intensities and writing speeds. **D**) Quantification of max stiffness and height change from B) and C).

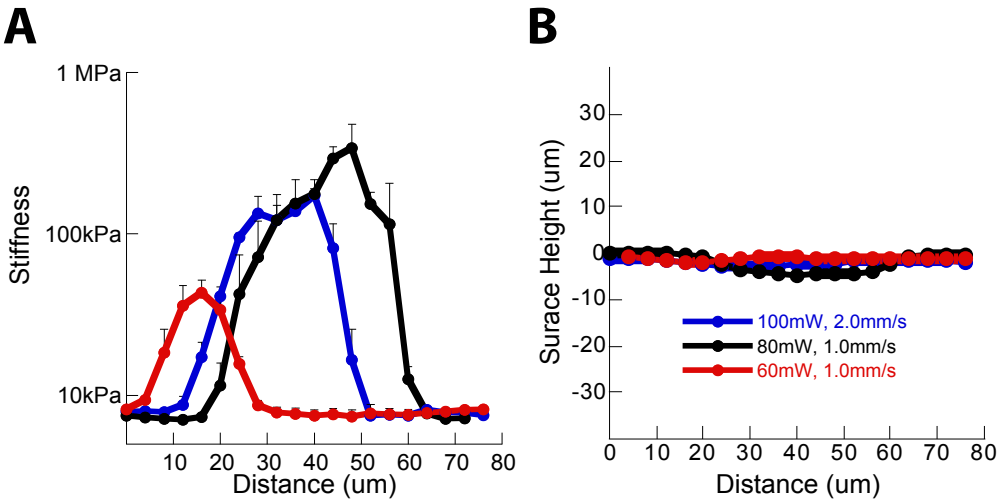

Figure 2.5: AFM results for 7 kPa gels. A) Mechanical changes and **B**) surface height changes according to various laser intensities and writing speeds.

increasing the laser intensity or decreasing the laser writing speed produced an increase in the stiffness jump. The marginal change in topography can be attributed to a change in crosslinking density that affects the swelling of the material. By comparison, a fully crosslinked gel (prepolymer solution exposed to UV for ~10 min) produced a substrate stiffness of ~ 250 kPa. Thus, we believe that for stiffened regions greater than 250 kPa are a result of increased physical entanglement of the PEG chains.

2.3.3 *in Vitro* Cellular Experiments

Employing gold nanorods with their NIR-absorbing optical properties offers an interesting avenue for crosslinking hydrogels in tissue engineering. In previous biomedical research, gold nanorods have been utilized in triggered drug delivery, hydrogel actuation, and sensing [23-25]. A concern in each case is nanorod cell toxicity. Thus, we modified the nanorod surface with PEG-thiol (a non-biofouling, nontoxic coating) and selected a concentration of PEGylated nanorods (1 nM) that minimally affects cell viability [26].

After validating the stiffness increases associated with DPP, we investigated the *in vitro* cellular response to the mechanical patterns. 17 kPa gels were patterned with 80 mW : 1.0 mm s^{-1} (which produced an increase in stiffness to 370 kPa at the peak value, as noted in Figure 2.4). Gels were modified with the addition of 2.5 mM PEG-RGDS for cell adhesion. A7R5 smooth muscle cells were seeded onto the gels and grown for six days. Images were taken at each day to assess migratory patterns, and on day 6, cells were fixed and stained for actin and nuclei. The timelapse images in Figure 2.6A suggest that cells evenly distributed initially but migrated onto the patterned areas and elongated by day 3 or 4.

Figure 2.6B details the actin alignment according to patterns. We chose to vary the distance between patterns, namely 50 μm, 100 μm, and 150 μm, to assess cell recruitment and alignment. 50 μm spaced-patterns showed some bridging effects between cells in close proximity and on adjacent patterns, however all patterns exhibited optimal nuclei alignment. Moreover, these data suggest that once cells migrated to the pattern, they recruited other cells to form aligned cell aggregates. It is well known that cells migrate towards stiffer regions of their substrate, a process called durotaxis. At the molecular level, cells transmit mechanical signals from their extracellular environment – in this case a patterned hydrogel – via mechanotransduction pathways and undergo migration to stiffer areas [27]. By providing a means to control substrate stiffness, DPP can be a useful platform for studying a range of molecular sensing mechanisms during durotaxis.

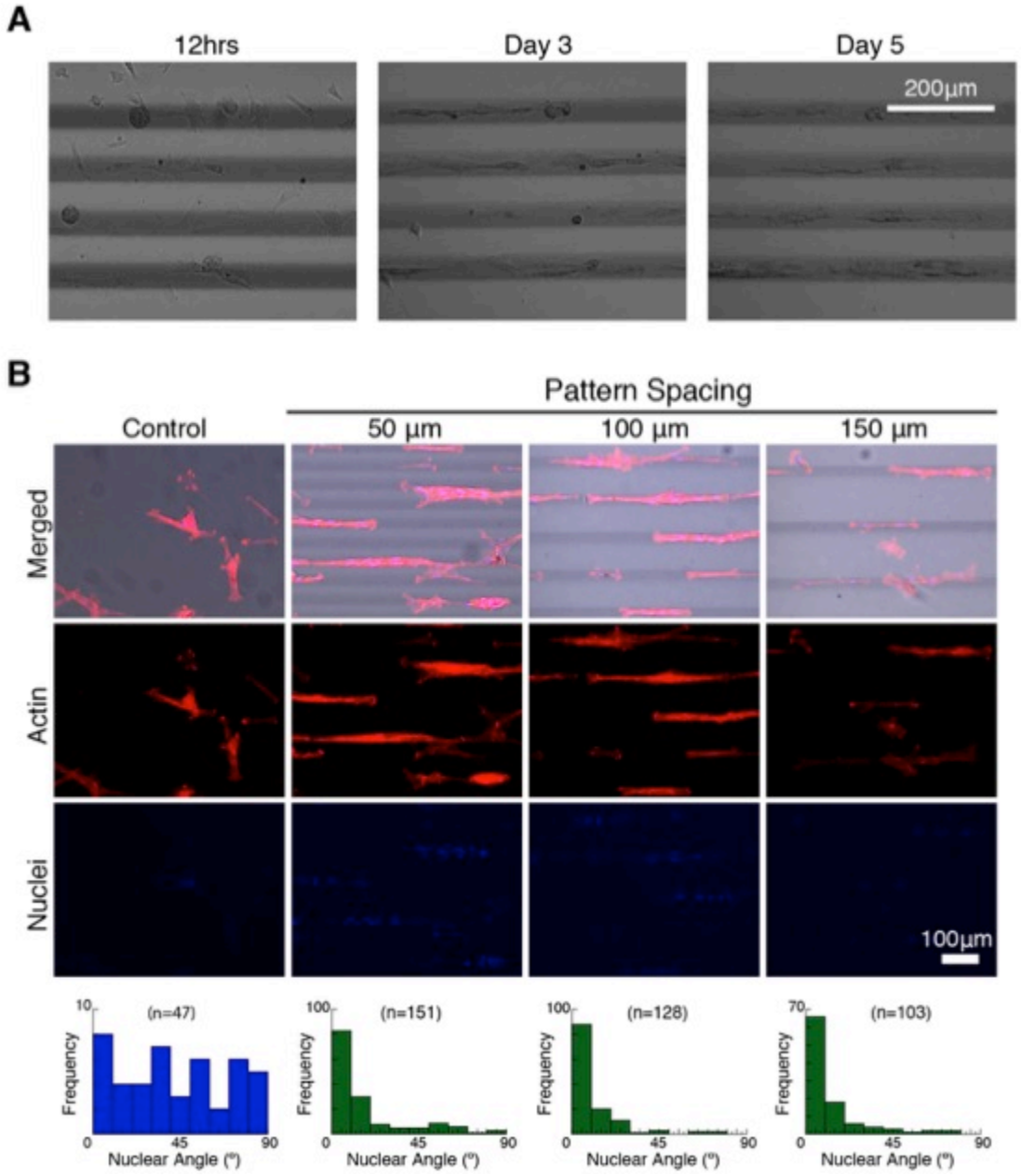

Figure 2.6: *in vitro* Cell Analysis. A) A7R5 smooth muscle cells show migration to the stiffer regions patterned by DPP. **B**) A7R5 cells stained for actin/nuclei on day 6 after incubating on DPP stiffened hydrogels with 50, 100, 150 micron spacing between the patterns. Cell alignment is quantified according to the patterned lines (0 degrees being perfectly aligned to the pattern) and compared to controls with no patterning.

2.4 Conclusions

DPP provides a novel way to spatially and tunably pattern mechanical changes on a hydrogel substrate. It allows the user to modulate stiffness according to laser intensity, writing speed and any digital pattern, thus providing enhanced flexibility in hydrogel design without the requirement of multiple polymer solutions or physical masks. DPP could be employed in various facets of tissue engineering, such as for studying tissue mechanics in governing cell fate (e.g. stem cell differentiation, migration, and proliferation). More generally, the platform could be used on a variety of temperature-sensitive materials for the effect of altering scaffold mechanics (via thermal crosslinking or degradation). Patterning resolution could also be optimized with the appropriate automated stage and light configuration (e.g. ultra-focused laser). With its versatility and adaptability, DPP can be a potentially useful tool for mechanically patterning hydrogels in a designer fashion.

2.5 Acknowledgements

Chapter 2, in full, is a reformatted version of the published article as appears in Advanced Functional Materials, Volume 24 (2014). The dissertation author was the primary investigator and author of this paper, and thanks co-authors Dr. Yu Suk Choi, Matthew G. Ondeck, Dr. Adam J. Engler, and Dr. Shaochen Chen for their contributions. This work was supported by the National Science Foundation (grants CMMI-1130894, CMMI-1332681), the National Institute of Health (NIH DP02 OD006460), and UCSD Neuroscience Microscopy Shared Facility Grant P30 NS047101. We would like to thank Dr. Marilyn Farquhar for the use of the electron microscopy facility at UCSD, and Timo Meerloo for electron microscopy sample preparation. We would also like to thank Dr. Xin Qu (UC San Diego) and Professor Jason Burdick (University of Pennsylvania) for helpful discussions.

2.6 References

1 Z. Nie, E. Kumacheva, *Nature Materials*, 2008, **7**, 277.

2 T. Dvir, B. P. Timko, D. S. Kohane, R. Langer, *Nature nanotechnology*, 2011, **6**, 13.

3 A. M. Kloxin, A. M. Kasko, C. N. Salinas, K. S. Anseth, *Science* 2009, **324**, 59.

4 A. Atala, F. K. Kasper, A. G. Mikos, *Science translational medicine*, 2012, **4**, 160rv12.

5 M. P. Lutolf, J. A. Hubbell, *Nat Biotechnol*, 2005, **23**, 47.

6 A. J. Engler, S. Sen, H. L. Sweeney, D. E. Discher, *Cell* 2006, **126**, 677.

7 A. Engler, L. Bacakova, C. Newman, A. Hategan, M. Griffin, D. Discher, *Biophys J*, 2004, **86**, 617.

8 Y. S. Choi, L. G. Vincent, A. R. Lee, K. C. Kretchmer, S. Chirasatitsin, M. K. Dobke, A. J. Engler, *Biomaterials*, 2012, **33**, 6943.

9 M. Guvendiren, J. A. Burdick, *Nature communications*, 2012, **3**, 792.

10 C. M. Lo, H. B. Wang, M. Dembo, Y. L. Wang, *Biophysical Journal*, 2000, **79**, 144.

11 B. C. Isenberg, P. A. Dimilla, M. Walker, S. Kim, J. Y. Wong, *Biophysical journal*, 2009, **97**, 1313.

12 L. G. Vincent, Y. S. Choi, B. Alonso-Latorre, J. C. del Alamo, A. J. Engler, *Biotechnology journal*, 2013, **8**, 472.

13 A. Pathak, S. Kumar, *Proceedings of the National Academy of Sciences of the United States of America*, 2012, **109**, 10334.

14 B. D. Fairbanks, M. P. Schwartz, C. N. Bowman, K. S. Anseth, *Biomaterials*, 2009, **30**, 6702.

15 M. S. Hahn, L. J. Taite, J. J. Moon, M. C. Rowland, K. A. Ruffino, J. L. West, *Biomaterials*, 2006, **27**, 2519.

16 T. K. Sau, C. J. Murphy, *Langmuir : the ACS journal of surfaces and colloids*, 2004, **20**, 6414.

17 H. W. Liao, J. H. Hafner, *Chem Mater*, 2005, **17**, 4636.

18 M. Radmacher, *Method Cell Biol*, 2007, **83**, 347.

19 N. A. Peppas, J. Z. Hilt, A. Khademhosseini, R. Langer, *Adv. Mater.*, 2006, **18**, 1345.

20 C. C. Lin, K. S. Anseth, *Pharm. Res.*, 2009, **26**, 631.

21 S. Link, M. A. El-Sayed, *J Phys Chem B*, 1999, **103**, 8410.

22 S. Link, M. A. El-Sayed, *Int Rev Phys Chem*, 2000, **19**, 409.

23 K. C. Hribar, R. B. Metter, J. L. Ifkovits, T. Troxler, J. A. Burdick, *Small*, 2009, **5**, 1830.

24 K. C. Hribar, M. H. Lee, D. Lee, J. A. Burdick, *ACS Nano*, 2011, **5**, 2948.

25 X. Huang, I. H. El-Sayed, W. Qian, M. A. El-Sayed, *J. Am. Chem. Soc.*, 2006, **128**, 2115.

26 C. Grabinski, N. Schaeublin, A. Wijaya, H. D'Couto, S. H. Baxamusa, K. Hamad-Schifferli, S. M. Hussain, *ACS Nano*, 2011, **5**, 2870.

27 A. W. Holle, A. J. Engler, *Current opinion in biotechnology,* 2011, **22**, 648.

Chapter 3

Three-dimensional cell patterning by ultrafast laser-induced degradation of collagen hydrogels

Abstract

We report a methodology for three-dimensional cell patterning through ultrafast laser induced degradation (ULID) in a hydrogel *in situ.* Gold nanorods within a cell-encapsulating collagen hydrogel absorb a focused near-infrared femtosecond laser beam, locally degrading the collagen and forming channels, into which endothelial cells migrate, align, and eventually form tube-like structures, similar to the formation of micro-vessels. Pattern resolution can be tuned by writing speed, nanorod concentration, collagen concentration, and laser power. ULID presents a flexible, one-step, direct-write method that can be broadly applicable in 3D tissue engineering systems requiring spatial cellular patterning.

3.1 Introduction

Tissue engineering offers the ability to generate functional tissues for implantation and *in vitro* modeling [1]. Three-dimensional (3D) cellular organization is critical to the function of a given tissue, and moreover, vascular integration plays a crucial role in providing nutrient and gas transport to the rest of the tissue [2-6]. Thus, materials that enable 3D organization of the tissue and its vasculature are of high importance [7, 8]. Hydrogels – water-swollen polymer networks - are extensively used as the scaffolding in engineered tissues [9]. There are various ways to control hydrogel structure in 3D for the purpose of dictating cellular organization. 3D printing, which includes extrusion, stereolithography, and projection printing, builds hydrogel structures in an additive fashion [10-12]. Oppositely, the selective removal of material from a bulk gel (for instance, using a ultrafast laser) can also generate 3D structures with precise architecture [13, 14].

To this end, we developed a novel 3D patterning method - ultrafast laser-induced degradation (ULID) – to pattern hydrogels that can be spatially degraded to promote cell recruitment, alignment, and ultimately vascular tube formation *in vitro* (Figure 3.1). The hydrogel is composed of collagen with gold nanorods that absorb NIR light at their plasmon resonance to photothermally degrade the collagen and create internal channels. Photothermal activation in temperature-sensitive materials has previously been explored for triggered drug release, bulk hydrogel degradation, and 2D hydrogel patterning [10, 15, 16]. Here, we report for the first time its utility in 3D hydrogel patterning. Patterning takes place within *milliseconds* and can be tuned by the laser writing speed, gold nanorod

concentration, collagen concentration and laser power. We empirically determined the optimal parameters to achieve high cell viability and reproducible patterning that enables vascular tube formation, making this ULID platform a viable alternative for cellular patterning in 3D, as well as an important step towards creating microvasculature in tissue engineered hydrogels.

3.2 Materials and Methods

3.2.1 Materials

For gold nanorods, hydrochloroauric acid ($HAuCl_4$), silver nitrate ($AgNO_3$), sodium borohydride ($NaBH_4$), and L-ascorbic acid were purchased from Sigma-Aldrich and cetyltrimethylammonium bromide (CTAB) was purchased from CalBioChem (EMD Millipore). Milli-Q water (18.2 Ω, MilliPore) was used in all synthesis steps. mPEG-thiol (5 kDa) (Nanocs) was used in nanorod surface modification. For hydrogels, collagen I, High Concentration (8.7 mg/mL) (VWR) was purchased.

3.2.2 Gold Nanorod Synthesis and Surface Modification

Gold nanorods were synthesized and using a seed-mediated growth and surface-modification methodology as previously described with some modifications [17]. 7.5mL 0.1M of CTAB was mixed with 250μL 0.01M $HAuCl_4$, followed by addition of 600μL 0.01 $NaBH_4$. Seeds formed after 2 minutes of mixing. The growth solution was prepared by mixing 40mL of 0.1M CTAB, 1.7 mL 0.01M $HAuCl_4$, 250μL of 0.01 $AgNO_3$, and 270 μL of 0.1M L-ascorbic acid, followed by 420μL of the seed solution. Nanorods formed after several hours. Nanorods were surface modified by first centrifuging twice at 15,000 *g*, removing the supernatant and resuspending in diH_2O, followed by adding

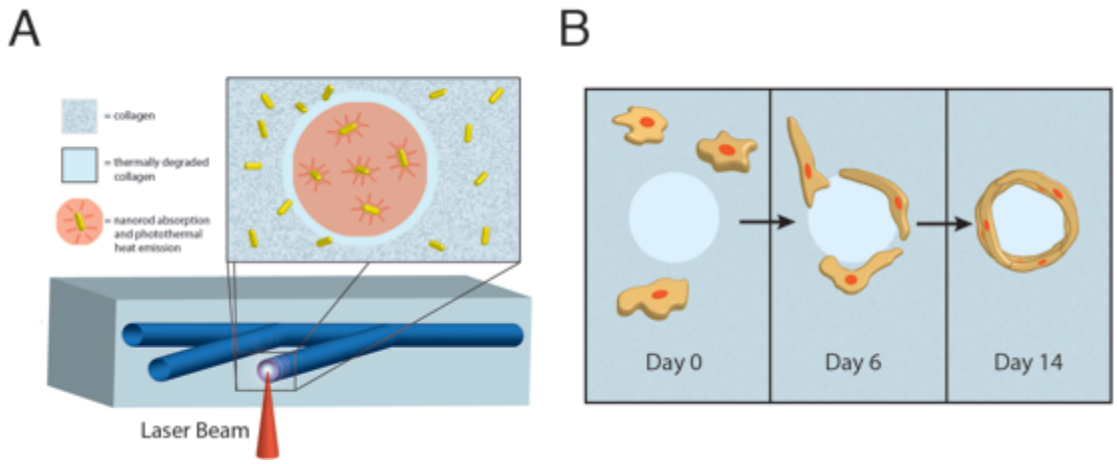

Figure 3.1: ULID patterning process and resulting cell response. A) A near-infrared (NIR) laser is focused inside the optically clear hydrogel and triggers the photothermal degradation of the collagen internally according to a computer-generated design, thereby creating channels. **B**) Expected cell response to degraded channels, where cells migrate towards the channels, align, and eventually form tubular structures with hollow cores, resembling microvasculature.

mPEG-SH dropwise and allow to gently mix for 2 hours. Nanorods were again pelleted and washed in diH_2O to remove excess reactants and sterilized through a 0.22 μm filter for later use. Final nanorod concentration was determined to be 5.45 e-9 M, by absorbance readings at its plasmon resonance (~800 nm).

3.2.3 Cell Culture

Bend3 mouse endothelial cells were used for cell culture experiments. Bend3 were grown in EGM-2 media (Lonza) and passaged several times after thawing. In preparation for collagen gel experiments, cells were trypsinized in 0.25% trypsin-EDTA, pelleted and resuspended in EGM-2 at various concentrations (1.0 million/mL up to 5 million/mL).

3.2.4 Gelation of Collagen-nanorod Hydrogels

Collagen gels were formed using the manufacturer's instructions. Briefly, an ice-cold mixture of 1.04μL of 1N NaOH, 10μL 10x dPBS, and 10 μL of nanorods at their final concentration was prepared. Next, 33 μL of either diH_2O or cells at various concentrations (in EGM-2) was added, again kept at 4 degrees. 46 μL of stock Collagen I (8.7 mg/mL) was added to the solution and pipetted slowly to mix the contents without producing air bubbles. The mixed solution was then added to 35 mm glass-bottom dishes with 10 mm wells (#0 cover glass, In Vitro Scientific) and placed in the incubator (37 degrees C, 5.0% CO_2) for 30 minutes. Following gelation, 2 mL of warmed EGM-2 media was added for cell culture.

3.2.5 *in Vitro* Hydrogel Patterning with bend3 Endothelial Cells

Gels were immediately used for patterning following gelation and addition of warmed media. The glass dishes were placed on an automatic stage atop an inverted

microscope (Olympus). A femtosecond laser beam (100 femtoseconds, 800 nm wavelength, 80 MHz, Coherent) was used to pattern the samples. The laser was focused through the laser objective lens (10x, NA 0.45) and onto the gel sample. Patterns were drawn inside the hydrogels by varying the focal plane of the beam (in z-direction) and according to digital masks designed on the computer, with controlled writing speeds (mm/s) using the stage controller (MS2000, ASI). Average power of the laser beam was modulated using an attenuator, varying the power from 100 - 290 mW, read by a power meter (Coherent Fieldmax).

2.3 Results and Discussion

Collagen hydrogels with gold nanorods displayed an absorbance profile similar to that of the nanorods in solution (Figure 3.2a), peaking at 800nm – coinciding with the wavelength of the NIR femtosecond laser. Collagen hydrogels without nanorods, conversely, showed low absorbance at 800 nm. When exposed to maximum power and the slowest speed (290 mW, 0.25 mm/s), collagen hydrogels without nanorods (collagen – NR) showed no changes in hydrogel morphology and resulting cell organization, suggesting the gold nanorods played a key role in the patterning mechanism (Figure 3.3). Figure 3.2b displays a computer-designed pattern using ULID on a collagen-NR hydrogel and the resulting image using brightfield microscopy.

Internal patterning of the collagen-nanorod hydrogel was a modular process, where laser power and writing speed (in millimeters per second, mm/s) altered the diameter of the resulting channel pattern. Figure 3.4a displays brightfield images of the resulting patterns in the collagen gel exposed to 100 mW or 150 mW laser power, at laser

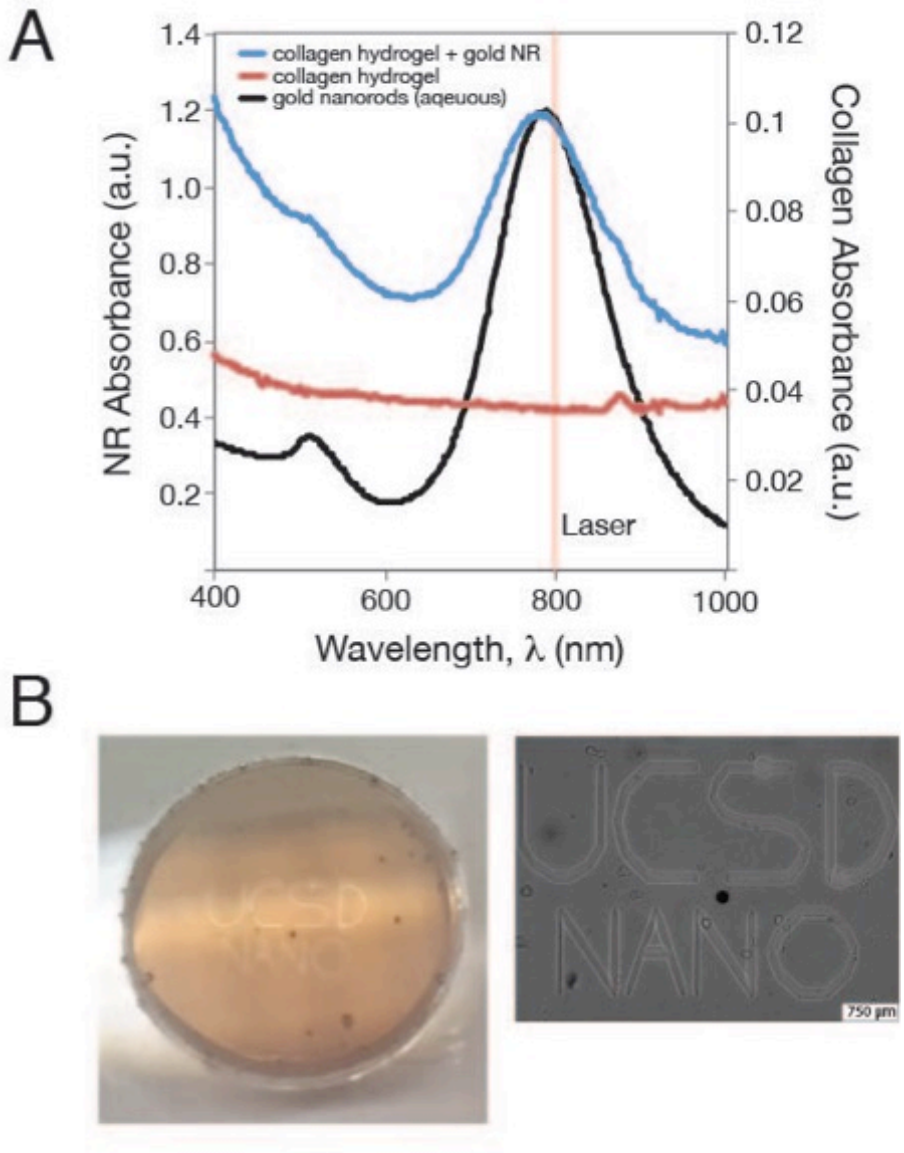

Figure 3.2: Characterization of materials. A) Absorbance of collagen hydrogels with and without nanorods, compared to nanorods in aqueous solution. The laser wavelength is also highlighted (800 nm). **B**) Image of gel within the glass dish, with outset showing the brightfield image of the same pattern.

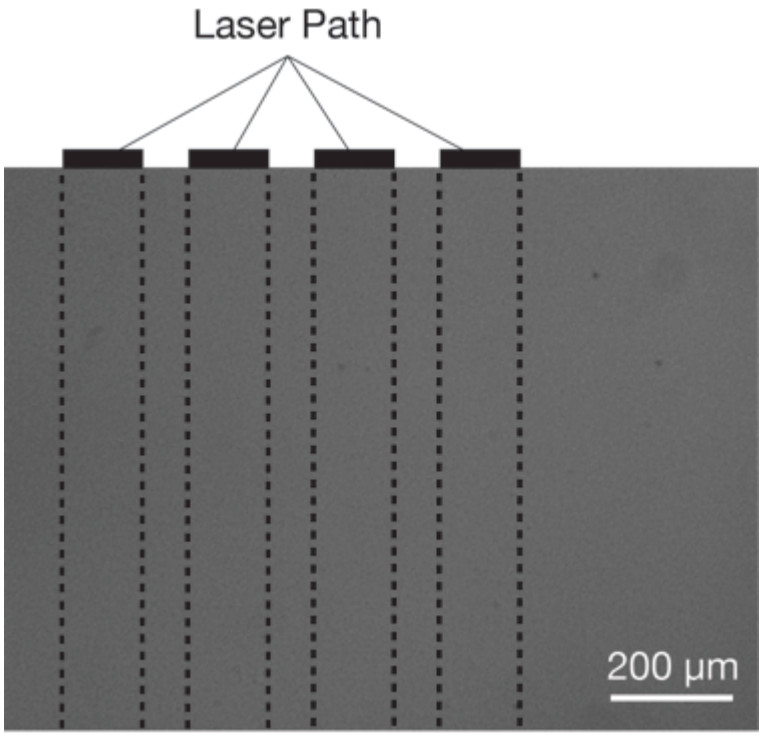

Figure 3.3: Collagen without nanorods displays no pattern. Top view of a collagen hydrogel without nanorods showing no response to NIR light at maximum power and slow writing speeds (290 mW, 0.25 mm/s, respectively).

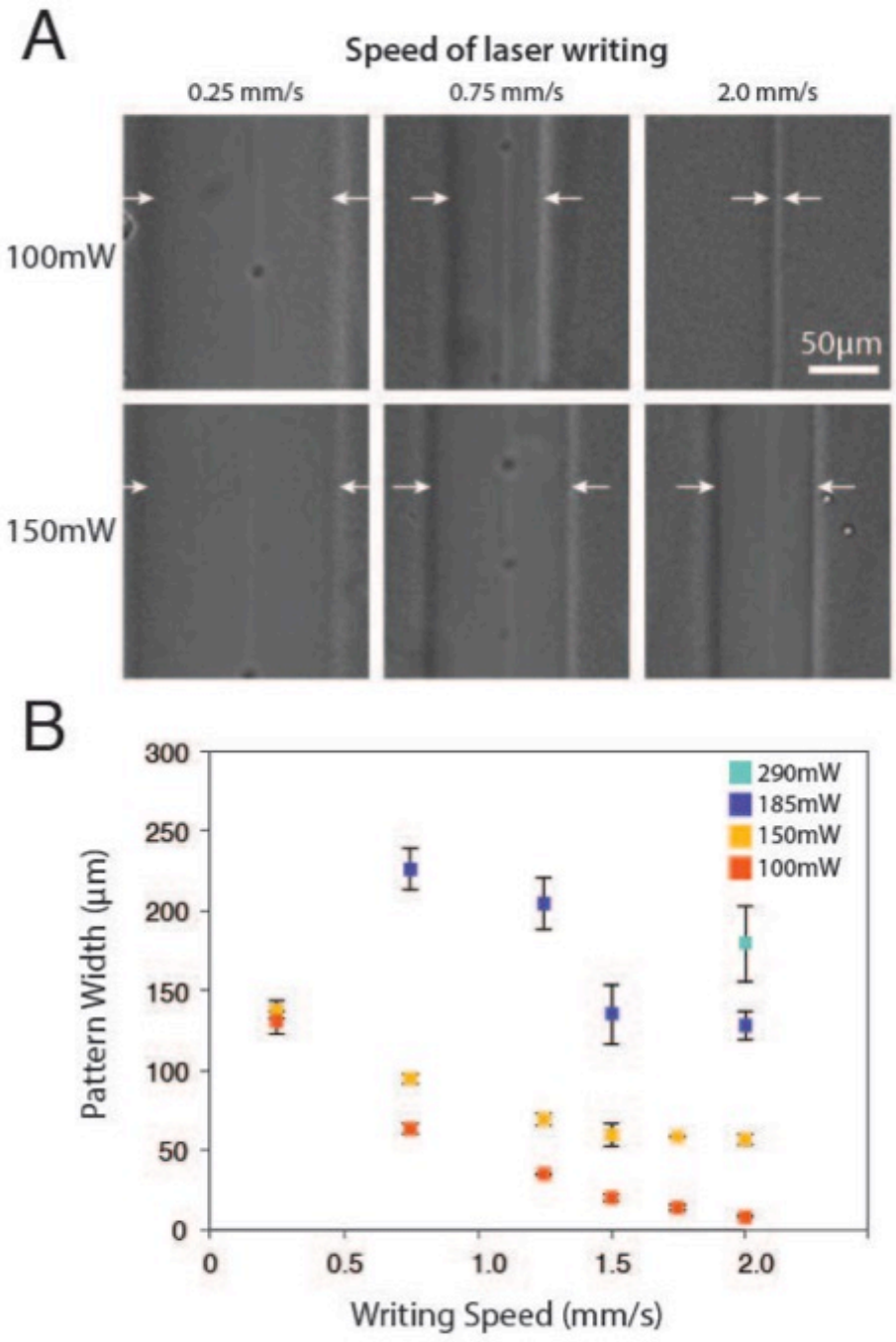

Figure 3.4: Characterization of ULID patterning. A) Brightfield images of the patterned lines at different writing speeds (0.25, 0.75, and 2.0 mm/s) and laser powers (100 and 150 mW). **B**) Characterization of patterned line widths in response to various writing speeds and laser powers.

scanning speeds of 0.25 mm/s, 0.75 mm/s, or 2.0 mm/s. Figure 3.4b shows the graphical representation of this data. An inverse relationship exists between the writing speed and pattern width. Laser power determines the threshold pattern size, where 100mW can generate 8.7 ± 0.5 μm resolution patterns (equal to the diameter of the laser beam) while higher powers such as 150mW and 190mW plateaued at 56.7 ± 3.0 μm and 128.6 ± 9.3 μm, respectively. Patterns made with 290mW power were barely distinguishable as the response in the collagen gel degraded the entire construct, however at a speed of 2.0 mm/s, the resolution was roughly 179.3 ± 23.5 μm. Writing speeds greater than 2.0 mm/s were not possible due to limitations with the automated stage, but presumably the patterns could become even more optically defined with faster speeds.

For cell studies, collagen-nanorod hydrogels with bend3 endothelial cells at a concentration of 1000 cells per μl were used. We patterned channels using various powers and writing speeds and performed a fluorescent live/dead assay with calcein AM/ethidium homodimer (Figure 3.5a). We believe collagen degradation is occurring because the cells appear loose and mobile in the patterned region upon irradiation of the NIR light. Ultimately, we chose a writing speed of 2.0 mm/s and a laser power of 100 mW for the remaining cell experiments due to their high pattern fidelity and high cell viability (>90%). We allowed collagen gels to incubate for several weeks, during which we observed cell migration towards the patterns, cell elongation on the walls, and by day 7 demonstrated hollow tube formation (Figure 3.5B). We confirmed that the channels were inducing this cellular organization by comparing with hydrogels without patterns (Figure 3.6). It is clearly shown that the patterns induce cellular tube formation.

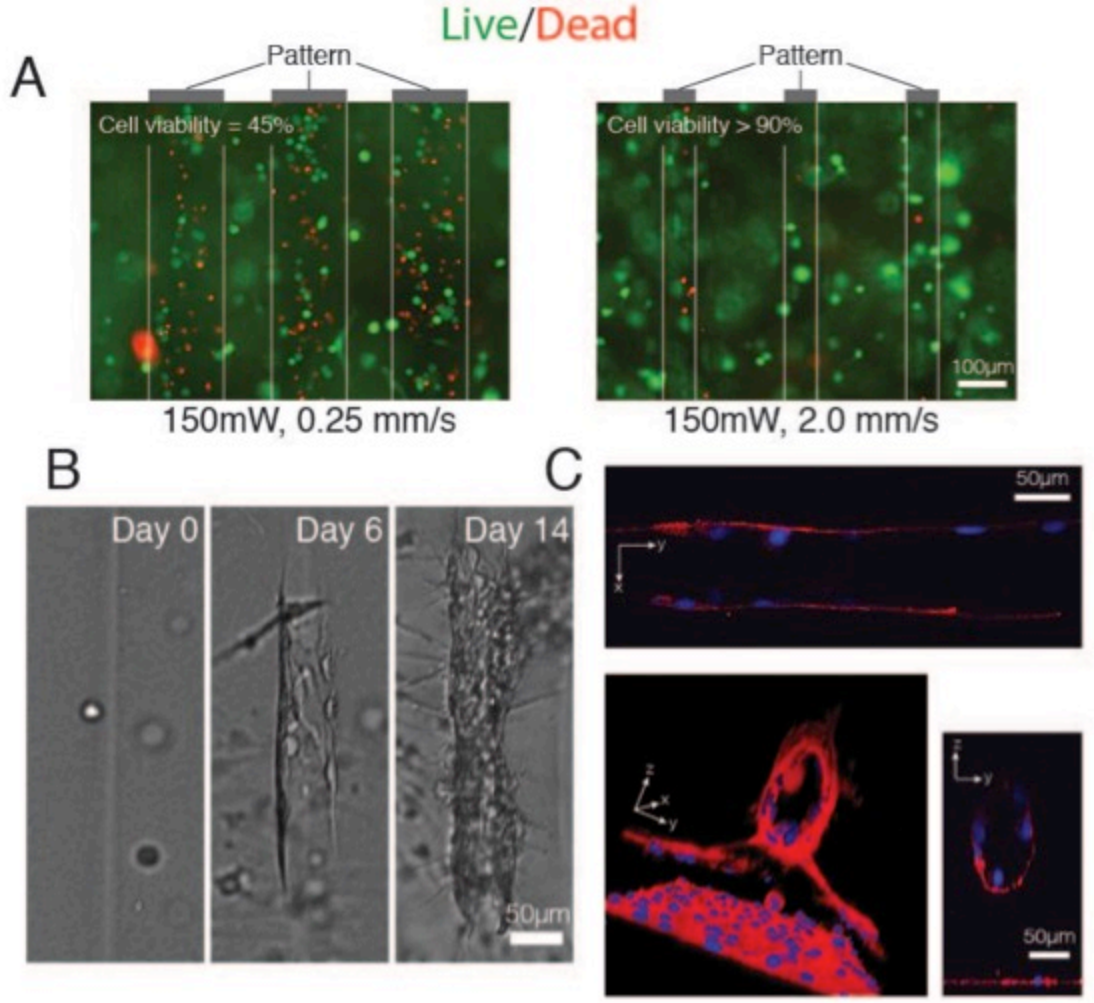

Figure 3.5: Endothelial cell response to 3D patterning. A) Live/dead fluorescent images overlayed with brightfield images, denoting differences in cell viability according to different writing speeds (0.25 and 2.0 mm/s) at 150mW laser power. **B**) Cell migration and tube formation, visualized in brightfield. **C**) Endothelial tube formation visualized with confocal, showing hollow cores in the YZ plane and aligned endothelial cells in the XY plane.

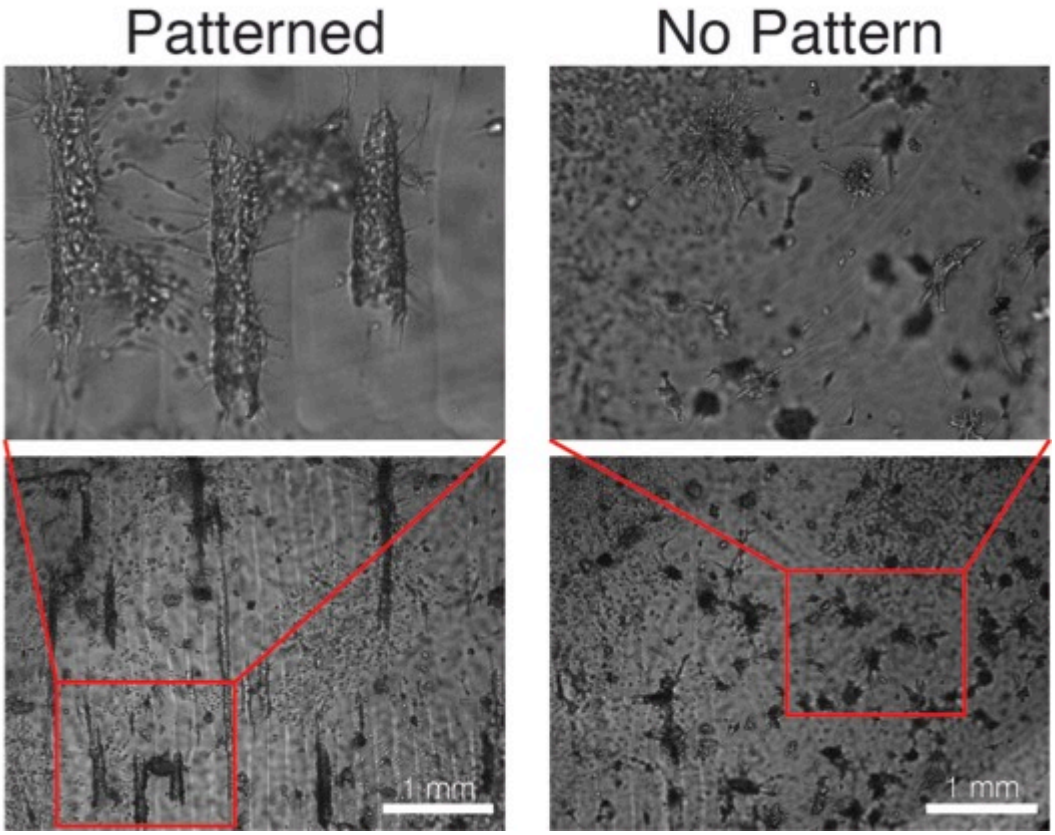

Figure 3.6: Pattern vs. no pattern cell response. Cell response to patterned and unpatterned collagen gels with gold nanorods after 14 days of culture.

To further confirm this phenomenon, the gels were fixed and stained for actin and nuclei and imaged using confocal microscopy. Using Volocity 3D reconstruction software (PerkinElmer Inc), we were able to visually observe the tube structure (Figure 3.5C), and XY and YZ planes confirmed the tubes length and hollow nature (Figure 3.5C outset). These data suggest tube formation occurred along the hollowed degraded channel and that endothelial cells populated the channel walls, forming hollow tubes similar to vessel formation in vasculogenesis.

The concept of spatially degrading a hydrogel for directing cellular response has been previously explored [14]. Groups have developed photolabile materials that respond to UV or visible light. One disadvantage of these systems, however, is the relatively long timescale – in *minutes* – to achieve patterning. Another disadvantage is that the shorter wavelengths (<600 nm) are damaging to cellular content, since water absorbs more light in those wavelengths. Here we demonstrated hydrogel patterning with NIR light as a more benign way to pattern hydrogels as it is minimally absorbed by water [18]. The efficient absorption of NIR light by the gold NRs and subsequent photothermal degradation of collagen allows for rapid patterning and minimizes cell exposure and thus potential for cell damage. We previously demonstrated a method to pattern gold nanorod-hydrogel substrates in 2D [16], however, to our knowledge, this concept has not yet been explored in 3D hydrogel patterning. Additionally, it was previously demonstrated that hydrated collagen (similar to our collagen hydrogel) degrades at 55˚C [19]. Thus, it can be interpreted that our patterns are momentarily (i.e. for *milliseconds*) heating up to this temperature during patterning before returning to sink conditions of 37˚C. Below a certain threshold (e.g. patterning at 50mW and 2.0 mm/s) we see no pattern and resulting

cell response. Therefore we believe the collagen is not degrading in this instance (Figure 3.3).

As with any new fabrication/materials/ process, finding an application for NR induced hydrogel degradation is key. We found that a combination of the right parameter of nanorod concentration, collagen material, laser speed, and laser power allowed for fabrication of 3D channels inside a pre-made collagen encapsulating cell network with very little cell damage. Using a programmable 3D stage allows for complex vascular tube formation. Vasculogenesis within hydrogels has remained a hurdle for achieving tissues of scale for implantation and biomimetic tissue models for *in vitro* studies. Previously, only a few groups have reported guidance of tube formation using labor-intensive techniques such as micromolding and casting [20, 21]. Here, we demonstrated a facile, one-step process that instantaneously degrades channels within the hydrogel, allowing for on-demand cell patterning. We not only showed endothelial cell migration and elongation on degraded channels, but confocal microscopy confirmed that *hollow* tube formation had occurred after a week, with the tubes elongating over several weeks after. This result could be interpreted as a breakthrough in the vascularization of tissue engineering systems and could be broadly implemented in many different tissues and models.

One such model that stands to benefit from this novel process is an angiogenesis model, whereby the creation of vascular tubes and subsequent seeding of a second cell type (e.g. cancer) can provide a facile means of studying angiogenesis between the two cell populations. Another possibility is to implement this platform with more complex vascular structures in hopes of guiding a biomimetic cellular organization *in vitro*. We believe this platform may also be generally applicable to many cell types that require

cellular organization in 3D, making it versatile and robust for tissue engineering systems. Lastly, while we showed complete collagen degradation, it may be achievable to incur partial degradation – or uncrosslinking – of the collagen network, or utilize a material whose degradation occurs at lower temperatures (closer to 37˚C) – which could allow for additionally altered cell responses.

2.4 Conclusions

The described platform – ultrafast light-induced degradation (ULID) of hydrogels – allows for the patterning of internal channels in collagen hydrogels *in situ*, in this case enabling microvasculature formation. Alignment of nearby cells can be visualized as early as 1 day post-patterning, while migration and tube formation may take up to 14 days. This platform has broad applications in *in vitro* cell patterning and can be applied to a host of light-responsive materials in addition to collagen. Furthermore, more complex patterns could be implemented to achieve a higher degree of 3D patterning.

2.5 Acknowledgements

Chapter 3, in part, is currently being prepared for submission for publication of the material. The dissertation author was the primary investigator and author of this paper, and thanks co-authors Dr. Yu Suk Choi, Matthew G. Ondeck, Dr. Adam J. Engler, and Dr. Shaochen Chen for their contributions. This work was supported by the National Science Foundation (grants CMMI-1130894, CMMI-1332681), the National Institute of Health (NIH DP02 OD006460), and UCSD Neuroscience Microscopy Shared Facility Grant P30 NS047101. We'd like to thank Dr. Amy Rommel and Prof. Inder Verma for graciously providing the bend3 cell line. We'd also like to acknowledge Yu Suk Choi (Assistant Professor at University of Sydney) for helpful conversations.

3.6 References

1. L.G. Griffith, G. Naughton, *Science*, 2002, **295**, 1009.

2. H. Bae, A.S. Puranik, R. Gauvin, F. Edalat, B. Carrillo-Conde, N.A. Peppas, *Science translational medicine*, 2012**, 4**, 160.

3. Y. Aizawa, R. Wylie, M. Shoichet, *Advanced materials*, 2010, **22**, 4831.

4. H. Aubin, J.W. Nichol, C.B. Hutson, H. Bae, A.L. Sieminski, D.M. Cropek, P. Akhyari, A. Khademhosseini, *Biomaterials*, 2010, **31**, 6941.

5. E. Cukierman, R. Pankov, K.M. Yamada, *Current opinion in cell biology*, 2002, **14**, 633.

6. D. Loessner, K.S. Stok, M.P. Lutolf, D.W. Hutmacher, J.A. Clements, S.C. Rizzi, *Biomaterials,* 2010, **31**, 8494.

7. J. Rouwkema, N.C. Rivron, C.A. van Blitterswijk, *Trends in biotechnology*, 2008, **26**, 434.

8. E.C. Novosel, C. Kleinhans, P.J. Kluger, *Advanced drug delivery reviews*, 2011, **63**, 300.

9. F. Brandl, F. Sommer, A. Goepferich, *Biomaterials*, 2007**, 28**, 134.

10. K.C. Hribar, P. Soman, J. Warner, P. Chung, S. Chen, *Lab on a chip*, 2014, **14**, 268.

11. A.P. Zhang, X. Qu, P. Soman, K.C. Hribar, J.W. Lee, S. Chen, S. He, *Advanced materials*, 2012, **24**, 4266.

12. D.B. Kolesky, R.L. Truby, A.S. Gladman, T.A. Busbee, K.A. Homan, J.A. Lewis, *Advanced materials*, 2014, **26**, 3124.

13. C.A. DeForest, K.S. Anseth, *Nature chemistry*, 2011, **3**, 925.

14. A.M. Kloxin, A.M., Kasko, C.N. Salinas, K.S. Anseth, *Science*, 2009, **324**, 59.

15. K.C. Hribar, M.H. Lee, D. Lee, J.A. Burdick, *ACS nano*, 2011, **5**, 2948.

16. K.C. Hribar, Y.S. Choi, M.G. Ondeck, A.J. Engler, S. Chen, *Adv Funct Mater*, 2014, **24**, 4922.

17. H.W. Liao, J.H. Hafner, *Chem Mater*, 2005, **17**, 4636.

18. R. Weissleder, *Nature biotechnology*, 2001, **19**, 316.

19. L. Bozec, M. Odlyha, *Biophysical journal*, 2011, **101**, 228.

20. J.S. Miller, K.R. Stevens, M.T. Yang, B.M. Baker, D.H. Nguyen, D.M. Cohen, E. Toro, A.A. Chen, P.A. Galie, X. Yu, R. Chaturvedi, S.N. Bhatia, C.S. Chen, *Nature materials*, 2012, **11**, 768.

21. J.D. Baranski, R.R., Chaturvedi, K.R. Stevens, J. Eyckmans, B. Carvalho, R.D. Solorzano, M.T. Yang, J.S. Miller, S.N. Bhatia, C.S. Chen, *Proceedings of the National Academy of Sciences of the United States of America*, 2013, **110**, 7586.

Chapter 4

Nonlinear 3D Projection Printing of Concave Hydrogel Microstructures for Long-Term Multicellular Spheroid and Embryoid Body Culture

Abstract

Long-term culture and monitoring of individual multicellular spheroids and embryoid bodies (EBs) remains a challenge for in vitro cell propogation. Here, we used a continuous 3D projection printing approach –with an important modification of nonlinear exposure — to generate concave hydrogel microstructures that permit spheroid growth and long-term maintenance, without the need for spheroid transfer. Breast cancer spheroids grown to 10 d in the concave structures showed hypoxic cores and signs of necrosis using immunofluorescent and histochemical staining, key features of the tumor microenvironment in vivo. EBs consisting of induced pluripotent stem cells (iPSCs) grown on the hydrogels demonstrated narrow size distribution and undifferentiated markers at 3 d, followed by signs of differentiation by the presence of cavities and staining of the three germ layers at 10 d. These findings demonstrate a new method for

long-term (e.g. beyond spheroid formation at day 2, and with media exchange) 3D cell culture that should be able to assist in cancer spheroid studies as well as embryogenesis and patient-derived disease modeling with iPSC EBs.

4.1 Introduction

In the fields of bioengineering and cell biology, three-dimensional (3D) cell culture provides a means to more accurately resemble the physiological *in vivo* environment for preclinical studies (e.g. drug screening, cellular assays) [1-3]. Specifically, multicellular spheroids have been extensively used for studying embryogenesis in the form of embryoid bodies (EBs) [4-6], adult tissue growth and organogenesis [7,8], cancer progression and liver toxicity [9,10]. To date, technologies that generate multicellular spheroids are limited in culture duration (requiring spheroid transfer), optical clarity issues for imaging, or broad size distributions.

The hanging-drop method is a commercially available technique that has been extensively utilized in spheroid culture, yet this process is labor intensive due to the need for spheroid transfer and sometimes lacks reproducibility [11]. Micromolding and photolithography have been used to create microwells made of PDMS [12,13], or hydrogels such as poly(ethylene glycol) (PEG) [14,15] and agarose [16]. But these technologies sometimes require multiple labor steps and produce microwells with limited optical transparency for imaging, protein adsorption issues, size restrictions or sample loss with media exhcange, thus resorting to spheroid transfer to another plate.

Here, we created hydrogel microstructures made of photocrosslinkable PEGDA with gradual concave topohraphies that are optically clear and can be utilized for long-term (e.g. with media-exchange, for durations beyond 2-3 days)

cell spheroid culture. PEG is an FDA approved biomaterial and often utilized in cell culture for its low immunogenicity, minimal protein adsorption, lack of adhesive peptides (which in turn limits cell-material interaction and promotes cell aggregation), as well as optical clarity [17]. The structures are fabricated with a 3D projection printer that uses nonlinear UV light exposure. We demonstrate their feasibility for spheroid culture in two distinct models – breast cancer spheroids and induced pluripotent stem cells (iPSC) EBs. In the breast cancer model, we grow the spheroids to 10 d, noting size changes and staining of hypoxia and necrosis, important markers in tumor progression [9]. Next, we use the platform to generate EBs of iPSCs. iPSCs have become a desirable cell type as they are autologous (patient-derived) by nature and thus have the potential to be used in a multitude of patient-specific *in vitro* models and therapies. We show tight uniformity in EB size after 3 d, with important undifferentiated markers expressed. Expanding the culture to 10 d, we witness the EBs' spontaneous differentiation into the three germ layers, as evidenced by immunofluorescent staining. Importantly, EBs remained within the concave hydrogels during the entire process. This platform opens the door for more biological models to be developed of many cell types, including, but not limited to, cancer, embryogenesis, and patient-derived disease models using iPSCs.

4.2 Materials and Methods

4.2.1 Continuous 3D Printing Using Nonlinear Optical Projection

This 3D printing protocol was adapted from a previously described technology [18], with the modification of nonlinear UV light exposure for generating concave structures. Prepolymer solution consisting of 20% poly(ethylene glycol) diacrylate (PEGDA) (MW 700, Sigma), 0.05% Irgacure 2959 (Ciba) in phosphate buffer saline (PBS) was administered between two glass slides and exposed to 10 mW/cm^2 UV light source (Omnicure S2000, 365 nm) using dynamic optical projection stereolithography setup. On the computer, a gradient pattern was designed in Adobe Photoshop and converted to a grayscale image. The image was then processed through in-house software and z-sliced into a series of transverse planes, according to the grayscale intensity of each pixel. These planes were successively and continuously fed onto the DMD chip as optical masks to be projected onto the prepolymer solution. Nonlinear exposure time was controlled by the following equation:

$$\text{Total exposure time} = T_0 + T_0*(1+L_i*A_2)^2 \qquad (1)$$

where T_0 is the exposure time for the base layer, L_i is the layer number, and A_2 is the nonlinear factor. Total exposure time is the aggregate exposure for all the layers. Based on the exposure time and inputted height, the software adjusts the speed of the automated stage. In this case, the z-height for all structures was held constant at 500 μm. Hydrogels were polymerized onto glass coverslips pretreated with the chemical modification of 3-(Trimethoxysilyl)-Propyl Methacrylate

(TMSPMA). After fabrication, the hydrogels were washed three times in PBS over the course of two days.

4.2.2 Atomic Force Microscopy

Stiffness of the hydrogels was confirmed by atomic force microscopy (AFM; MFP3D, Asylum Research) as detailed previously [19, 20]. Briefly, a pyramidal probe, 0.08 N/m spring constant with a 35° half angle (PNP-TR20, Nanoworld), was used to indent the substrate. The probe indentation velocity was fixed at 2 μm/s with the trigger force of 2 nN. Elastic modulus maps were determined by the Hertz cone model with a sample Poisson ratio of 0.5 fit over a range of 10%-90% indentation force [20]. AFM software (Igor pro 6.22) was applied to generate the stiffness.

4.2.3 Scanning Electron Microscopy (SEM)

Hydrogel samples were dehydrated using increasing amounts of ethanol:water (i.e. 20% ethanol, 30%, and so on) until they were submerged in 100% ethanol and dried via critical point drying (Tousimis AutoSamdri 815A). Samples were then sputter coated with iridium and imaged using an FEI SFEG Ultra-High Resolution SEM.

4.2.4 Breast Cancer Cell culture and Hydrogel Seeding

BT474 breast cancer cells were used for tumor spheroid studies. BT474 cells were obtained from ATCC and were maintained in RPMI-1640 media supplemented with 10% (v/v) fetal bovine serum (FBS), penicillin/streptomycin/L-glutamine, and Fungizone (Omega Scientific Inc.). Hydrogels were sterilized

under UV light, and BT474 cells were seeded into the wells at the concentrations of 250K mL^{-1} (LOW) and 750K mL^{-1} (HIGH).

4.2.5 BT474 Spheroid Imaging, Sectioning, and Analysis

Brightfield images of cancer spheroids were taken at various timepoints using a Leica Fluorescence Microscope, and a live/dead fluorescence assay (calcein AM/ethidium homodimer) was performed at day 10 to qualitatively assess cell viability. Spheroid size was quantified using ImageJ software. Spheroids also grown to day 10 were fixed in 4% paraformaldehyde and cryosectioned at 20 μm thickness. Sections were stained for HIF-1α (1:50 HIF-1α mouse mAb, Novus Biologicals), a hypoxia marker, and DAPI, a nuclear stain, and H&E staining was also performed.

4.2.6 Integration-free Human Induced Pluripotent Stem Cells (iPSCs) Generation

Human perinatal foreskin fibroblasts (BJ, ATCC) and human adult dermal fibroblasts (HDF, Cell Applications) were maintained in DMEM (Corning) supplemented with 10% FBS (Tissue Culture Biologicals) and Antibiotics/Antimicotic (Corning) in a 37°C, 5%CO_2 incubator. Cells were passaged at a ratio of 1:6 every 3-5 days by 0.25% Trypsin-EDTA (Corning) before reprogramming. To prepare for reprogramming, fibroblasts were seeded at a density of 2 x 10^5 cells/well in 6-well plates, and allowed to attach and spread for 48h. Reprogramming was performed following the instructions in a Sendai virus-based Cyto Tune kit (Life technologies) for the delivery of four factors Oct4, Sox2, Klf4 and c-Myc.

4.2.7 Human iPSC Culture and EB Formation

Following successful reprogramming, growth factor reduced Matrigel (BD Biosciences, NJ, USA) was used as the substrate for the maintenance of the iPSCs culture in serum- and feeder-free conditioned medium (StemPro®, Life Technologies) following the manufacturer's instructions. Cells were split at a ratio of 1:6 every 3-4 days by Versene (Life Technologies) before experiments.

Similar to our cancer cell seeding protocol, hydrogels were sterilized under UV for 1 hour. Human iPSCs at 70–80% confluency were detached by Accutase (Innovative Cell Technologies) and resuspended in regular culture medium with 5uM ROCK inhibitor Y27632 (Stemgent). Cells were seeded at concentrations of 100 k or 400 k mL^{-1} into each of the well of a 24-well plate, which had an individual hydrogel array construct. The plates were spun at a speed of 50 *g* for 3 minutes and then incubated in a 37°C, 5% CO_2 incubator. Maintenance medium was replaced everyday. EBs formed spontaneously within the center of each concave hydrogel structure, and were monitored and imaged using a Leica DIC microscope. Image analysis (e.g. EB diameter size) was performed on imageJ software.

4.2.8 EB Immunofluorescence Staining

Embryoid bodies (EBs) were fixed within the hydrogels in 4% paraformaldehyde in PBS three days following seeding. They were subsequently permeabilized with 0.1% Triton X-100 in PBS and incubated with antibodies against Oct4 (Cell Signaling Technology) and Nanog (Cell Signaling Technology) followed by fluorophore-conjugated anti-IgG antibodies. DAPI (Invitrogen) nucleus counterstain was also

performed. For differentiation studies, EBs were grown in the same manner on the concave hydrogels at varying concentrations (100 or 400 k cells mL^{-1}) for 10 days, followed by fixing and immunostaining with biomarkers for the three germ layers: SOX-1 for ectoderm, SOX-17 for endoderm, and Brachyury for mesoderm (R&D Systems). Images were taken using a Leica fluorescence microscope and an Olympus confocal microscope.

2.3 Results and Discussion

Concave hydrogel microstructures for spheroid culture were fabricated using a light-based, continuous 3D projection printing technology adapted with nonlinear UV light epxosure. (Figure 4.1A) [18,21]. A 2D image of a gradient circle pattern is converted to a series of layer slices (53 layers in total) based on its grayscale intensity at each pixel (Figure 4.1A). Each layer represents a cross-sectional image in the series in proportion to the height of the structure (500 μm). The series is then fed to the digital micromirror device (DMD) for UV projection onto the photocurable prepolymer solution – in this case, 20% (w/v) poly(ethylene glycol) (PEG) diacrylate – in a continuous fashion. Importantly, this 3D printing technology permits the creation of any complex and precisely defined concave structure simply by changing the design or gradient of the inputted pattern (Figure 4.2). This feature represents a major advancement to previous 3D printing platforms, which rely on printing one dot or one layer at a time, while overcoming limitations associated with micromolding of soft biomaterials with complex designs.

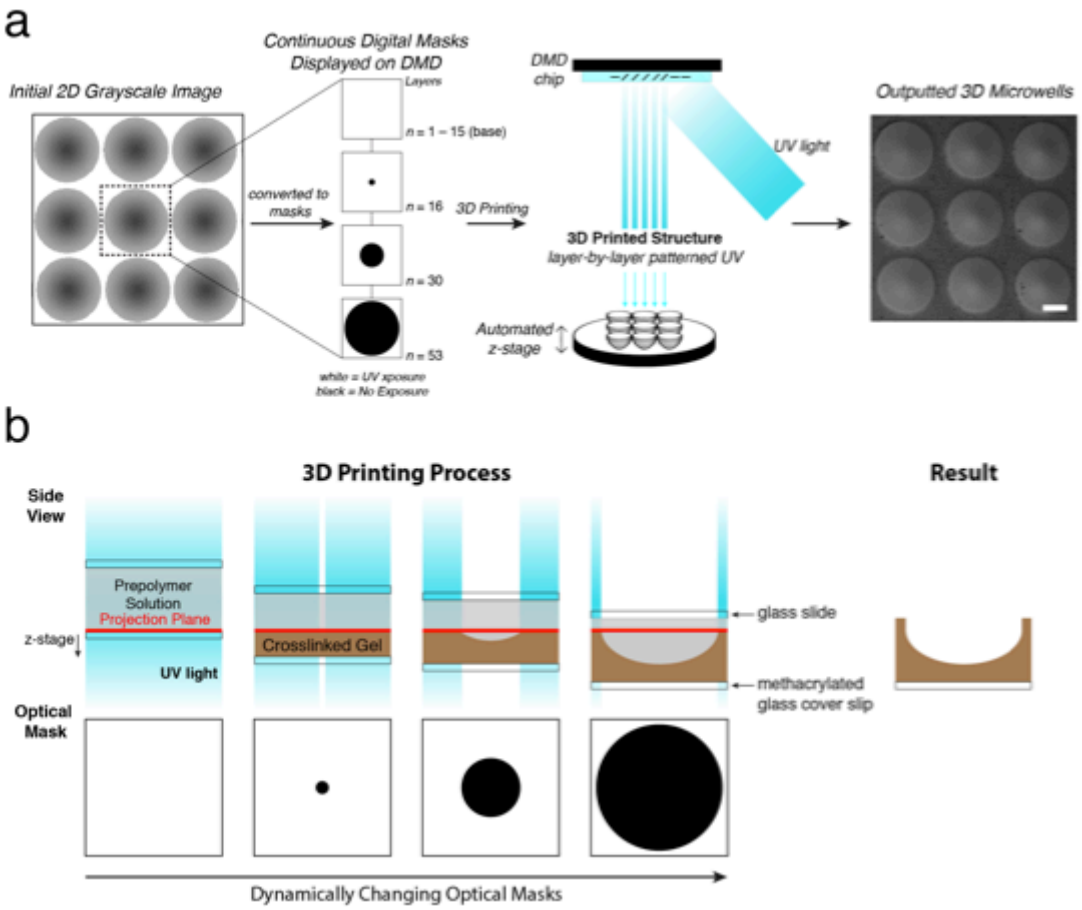

Figure 4.1: Continuous 3D printing process. A) Detailed schematic of the continuous 3D printing process. A grayscale image is divided into a series of digital masks (53 layers in total, 15 "base" layers where the entire structure is exposed to UV light). A white mask denotes a layer that is completely exposed to UV light, while black in the mask describes areas of no exposure for any given layer. Due to the gradient pattern in the grayscale image, the center of each concave structure receives the least amount of total UV exposure. The outputted structure is displayed on the right (scaled bar = 200 μm). **B**) Cross-sectional schematic of the 3D printing process over the course of all 53 layers. All scale bars = 200 μm.

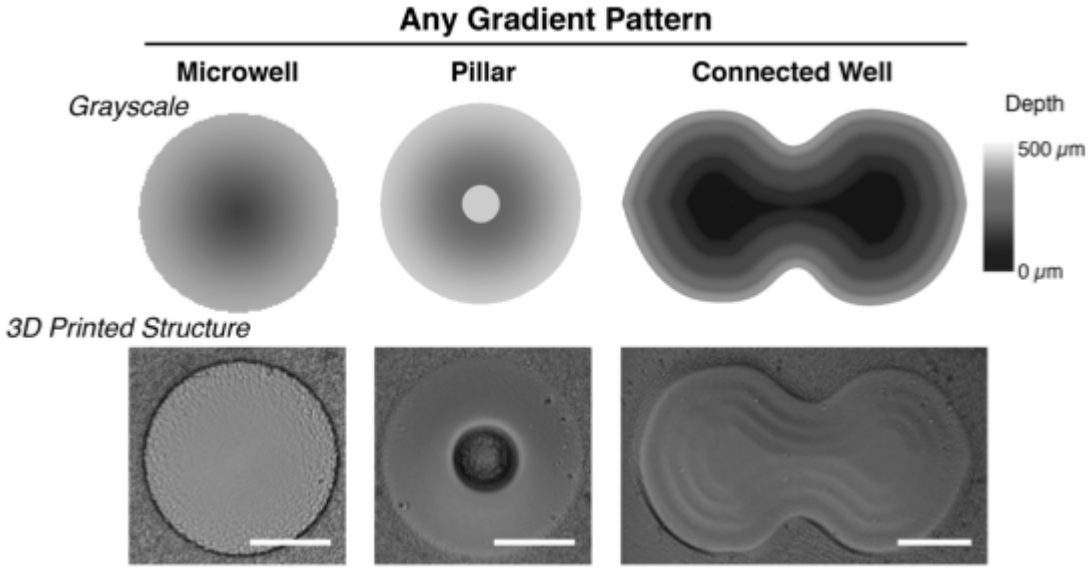

Figure 4.2: Versatility of Printing Design. Any gradient pattern can be designed and subsequently printed using this process, adding to its versatility in fabrication design.

A schemata of the 3D printing process at the molecular level is displayed in Figure 4.1B. For the first 15 layers, or masks, UV light is projected onto the entire prepolymer solution, photocrosslinking the base of the microwell structure. Subsequent optical masks with increasing areas of non-exposure (black, as indicated in Figure 4.1A) are displayed on the DMD. The concave hydrogel is therefore built in a continuous layer-by-layer fashion, alongside a continuously moving z-stage that coordinates its movements in the z direction with changes in the optical masks. Because we set the z-height to be 500 μm and there are 53 layers, the stage moves 9.4 μm for each layer, maintaining the same projection plane within the prepolymer solution as it moves through the layer series.

UV photopolymerization and gelation of PEGDA is a nonlinear process, where free radical initiation, polymer chain propagation, and termination take place on multi-order kinetics [22]. Thus we sought to create a 3D printing process that allows for nonlinear UV exposure (see *Methods)*. Figure 4.3 depicts the changes to the nonlinear fabrication parameters as well as the outputted structure, maintaining the same gradient circle design throughout.

As T_0 decreases, the well shape becomes wider and less polymerized, and largely unpolymerized in the middle of the concave hydrogel (Figure 4.3A, panels *i* to *ii*). This lack of polymerization is presumably due to a lower exposure time for the 15 base layers, where the entire solution is exposed to UV light. We hypothesize that a longer exposure time to the base layers is required to generate free radicals for the rest of the structure. While increasing exposure to the base layers can be achieved by increasing T_0 in a linear fashion, this method

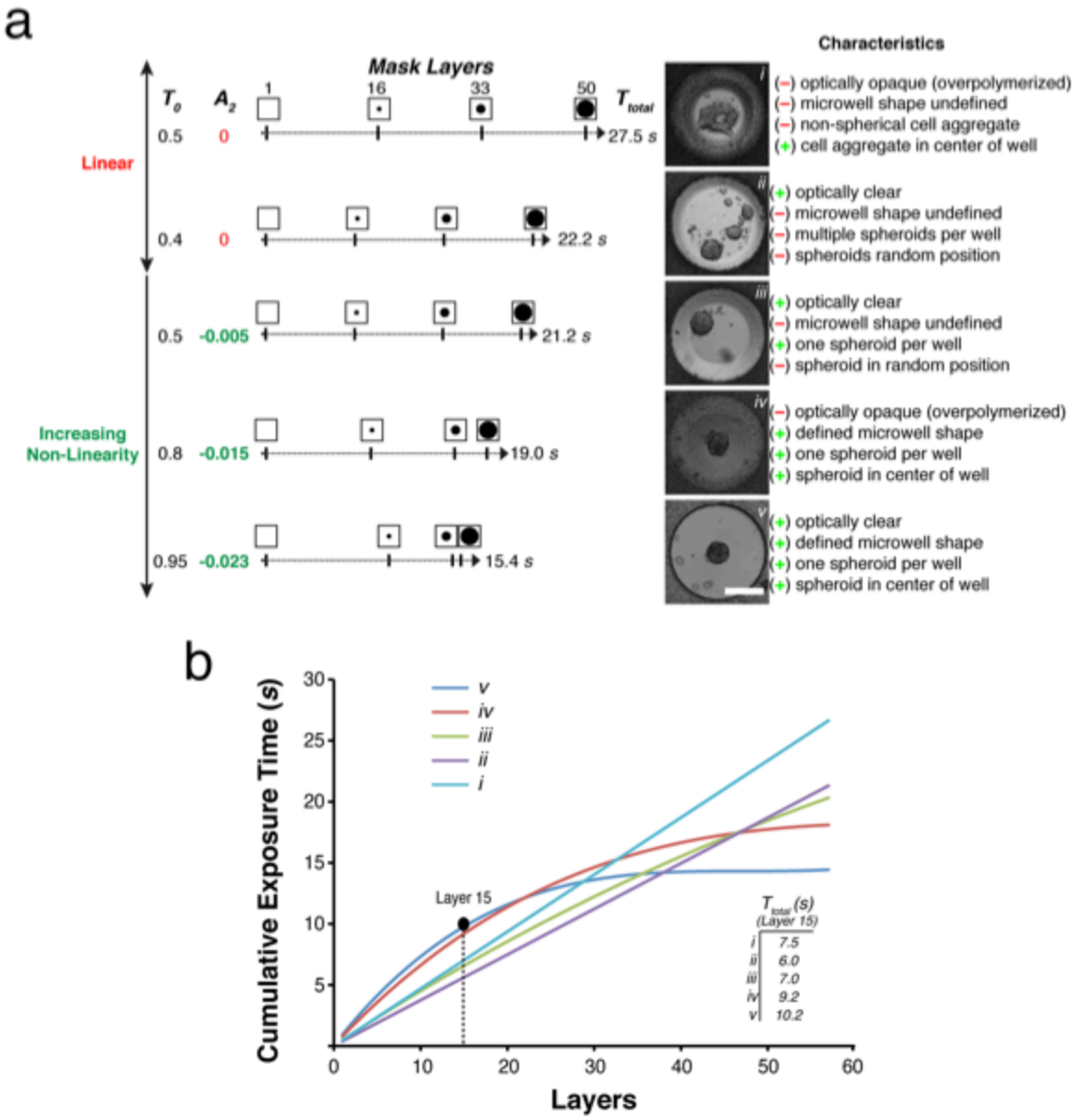

Figure 4.3: Characterization of nonlinear projection printing. A) Varying the fabrication parameters (T_0 and the nonlinear factor, A_2) to achieve an optically clear microwell that allows for single 3D cell spheroid growth in the middle of the concave hydrogel (*i* to *v*). The resulting microwells and day 3 spheroid culture are shown on the right. **B)** Graphical representation of the cumulative total exposure time at different layers in the optical mask series. The first 15 layers have a blank pattern, exposing the entire prepolymer solution to UV light and acting as the base of the structure. T_{total} values at layer 15 are displayed in the inset.

overpolymerizes the remaining layers of the hydrogel structure allowing for an undefined shape that is not optically clear (Figure 4.3A, panel *i*). We thus modulated the nonlinear factor, A_2, to vary the exposure time for each layer. When A_2 is negative, every successive layer is exposed for a shorter duration than the previous layer, in turn speeding up the entire fabrication process as it proceeds through the entire 53 layers (Figure 4.3A, panels *iii* to *v*). By increasing T_0 and making A_2 more negative, the bulk of the UV irradiation shifts to the earlier layers, allowing a longer duration for free radical generation in the base layers (where the entire prepolymer solution is exposed to UV light).

We empirically determined the optimal T_0 and A_2 values to be 0.95 *s* and -0.023, respectively, fitting our aforementioned design criteria – that is, a an optically clear, concave hydrogel that permits single spheroid formation in its center (Figure 4.3A, panel *v*). Figure 4.3b provides a graphical understanding of the cumulative exposure time in accordance to the layers for each of the five cases shown in Figure 4.3A. It is interesting to note the cumulative exposure time for the first 15 base layers increases from 6.0 *s* for linear exposure to 10.2 *s* for nonlinear exposure in panels *ii* and *v* of Figure 4.4A, respectively (Figure 4.4b inset). Thus, we believe that a longer duration of UV exposure to the base layers is required to initiate the free radical polymerization process throughout the prepolymer solution. Below this time, we observed unpolymerized sections in the microwell center.

We used scanning electron microscopy to assess the topography of the hydrogels. (Figure 4.4A). The hydrogel displays a gradually increasing slope from the center to the edge and steep walls, indicating a concave shape. Atomic force

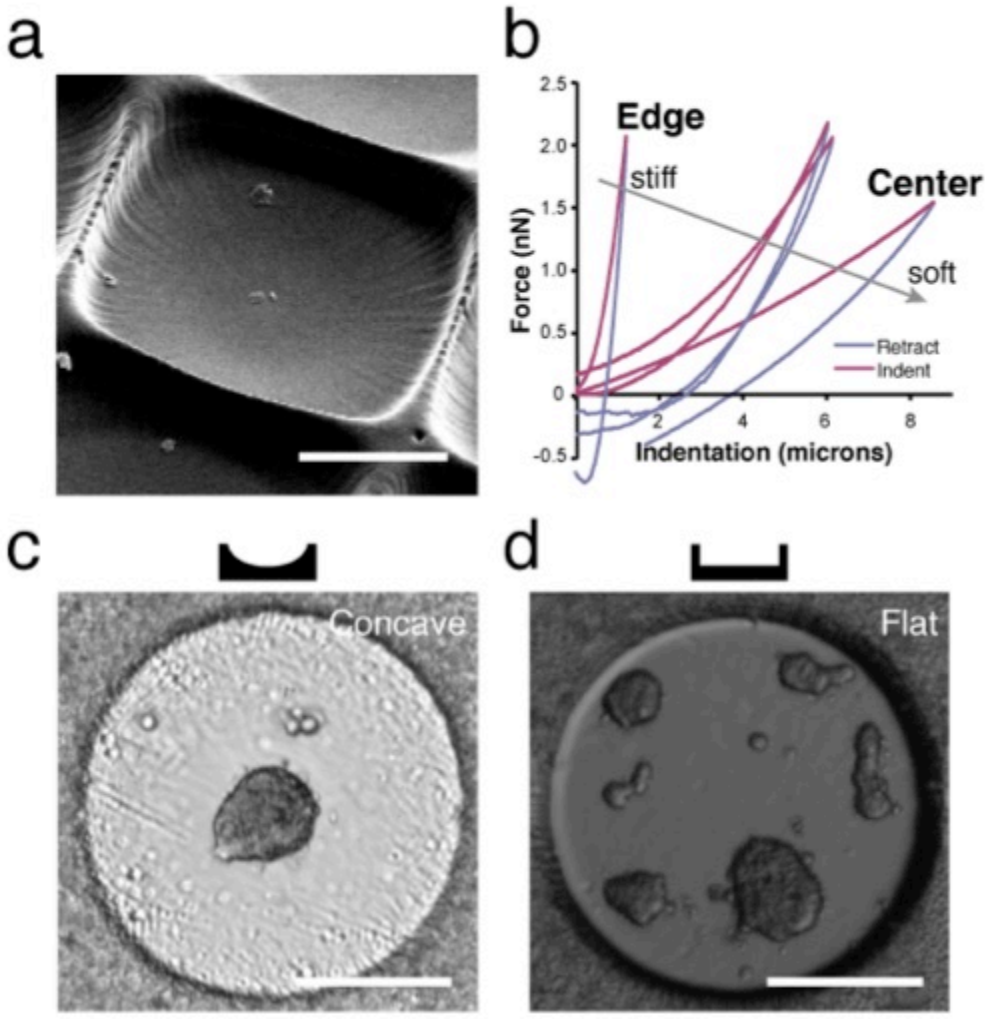

Figure 4.4: Characterization of 3D printed structures. A) Scanning Electron Microscopy image of dehydrated concave hydrogels. **B**) AFM stiffness measurements at different regions of the concave hydrogel. The center of the well appears soft (10 Pa) and gradually increases in stiffness to the edge of the well (~200 Pa). The walls of the structure, which are also the tallest part and the most exposed to UV, have a stiffness of ~1-2 kPa. **C**) Concave versus **D**) flat hydrogels for tumor spheroid generation. Cell culture at the day 3 timepoint is displayed. All scale bars = 200 μm.

microscopy was used to characterize the stiffness profile on the concave hydrogel surface (Figure 4.4B). The structure displayed a soft, low modulus center (10 Pa) that stiffened to the edge of the well (~200 Pa). The tallest part of the structure – the wall of the hydrogel – represented the stiffest region (1-2 kPa). We hypothesized that the soft center correlates to earlier layers of UV exposure during the fabrication process, and as it proceeds through the layers, increasing UV exposure drives additional crosslinking to stiffen the hydrogel. We confirmed this by taking stiffness measurements of flat hydrogel structures with different UV exposure to the base (Figure 4.5). It appears that the flat wells with 15 base layers has an average stiffness of 20 Pa, while 24 base layers and 34 base layers have higher moduli profiles of 151 Pa and 203 Pa, respectively. Thus, it is likely that the gradient UV exposure in our concave hydrogels is due to the variable light exposure in the continuous layer-by-layer 3D printing process.

For preliminary cell studies, we fabricated flat or concave hydrogels and seeded BT474 breast cancer cells to examine the effect of concavity on spheroid generation (Figure 4.4C and D). When flat hydrogels were used in cell culture, several spheroids of varying sizes formed within each well, while the desired single spheroid formation was achieved in the concave hydrogel microstructures. Expanding on our first cell experiments, BT474 breast cancer cells were seeded at various densities and used to assess tumor spheroid generation and growth within the concave hydrogels (Figure 4.6A). At day 2, LOW (250 k mL^{-1}) and HIGH (750 k mL^{-1}) cell seeding densities produced spheroids with diameters 146 ± 11 μm and 213 ± 16 μm, respectively (Figure 4.6B). However, over the course of the next

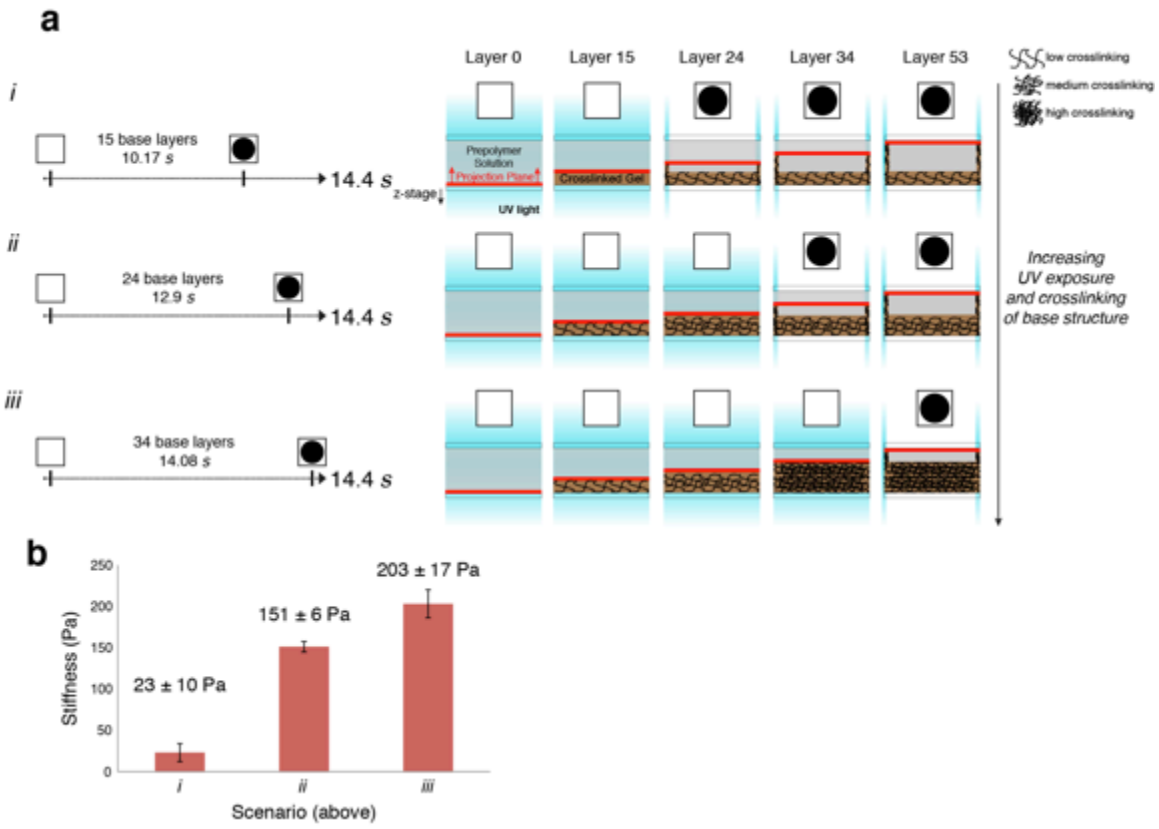

Figure 4.5: Assessment of 3D printing process with flat hydrogels. A) Schematics showing three scenarios for different base layers and exposure times and **B**) the resulting stiffness profiles from atomic force microscopy measurements.

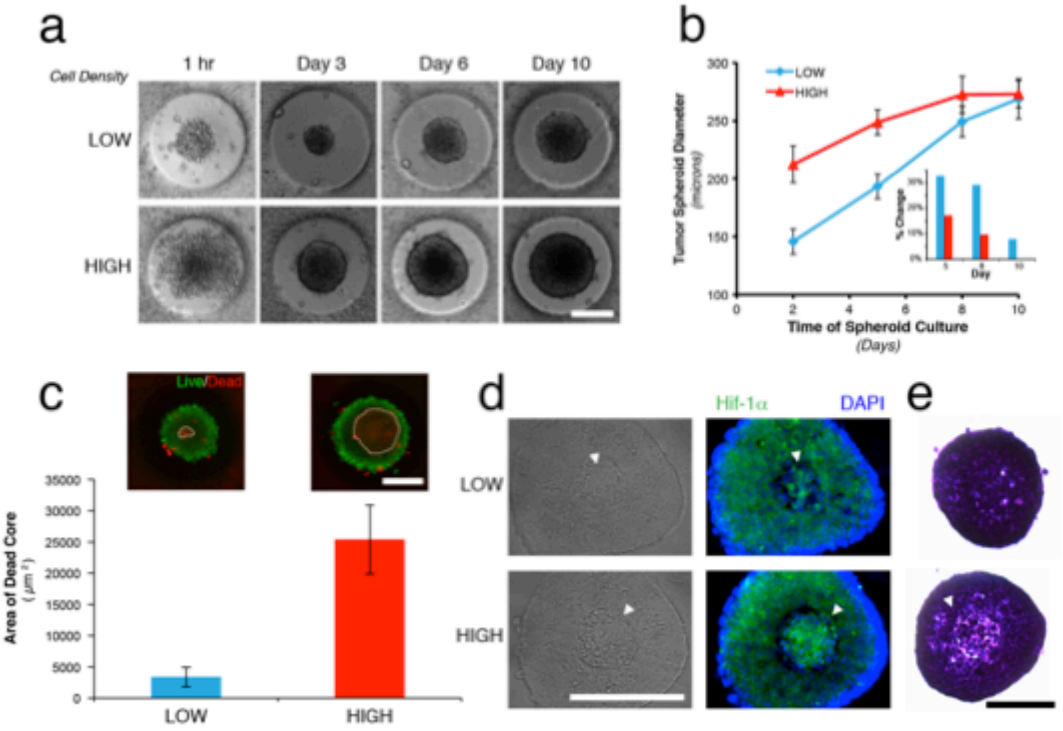

Figure 4.6: 3D printed concave hydrogels for cancer spheroid culture. A) Timelapse images of tumor spheroids grown at LOW (250 k mL^{-1}) and HIGH (750 k mL^{-1}) cell densities. **B**) Tumor spheroid sizes quantified over 10 days for LOW and HIGH cell seeding density (n = 12 or more). Inset: percent change in spheroid size in relation to the previous timepoint. **C**) Fluorescent images at day 10 depict live/dead staining (green/red), and the area of the dead core quantified (white outline of red fluorescence in live/dead images) (n=9). **D**) Immunohistochemistry staining of HIF-1-alpha (hypoxia marker), DAPI (nuclear), and brightfield images of spheroid cross-sections. **E**) Hematoxylin & Eosin (H&E) staining of spheroid cross-sections. Scale bars = 200 μm.

several days, spheroids from the HIGH group began to plateau at a size of around 250-275 μm, while the smaller spheroids from the LOW group continued to grow in size, albeit smaller than the 250 μm threshold. Growth rates for each group confirmed this trend (Figure 4.6B, inset). At day 10, spheroid diameters for both groups were within standard deviations of each other – 269 ± 17 μm and 273 ± 12 μm for LOW and HIGH groups, respectively.

Interestingly, live/dead staining with calcein AM/ethidium homodimer at day 10 showed that the HIGH group exhibited a 10-fold increase in its dead core area, compared to the LOW group: 25,394 ± 5514 cm^2 and 3,385 ± 1,565 cm^2 for HIGH and LOW groups, respectively (Figure 4.6C). This observation suggests a necrotic core forming in the HIGH group, correlating with regression in spheroid growth. It has been well documented that tumor spheroids greater than ~200 μm in diameter demonstrate a hypoxic core due to a nutrient and gas transport gradient, which in turn can lead to necrosis [9, 23]. The presence of a hypoxic core in the tumor spheroid provides a more physiologically relevant tumor model for cancer screening applications, as tumor hypoxia *in vivo* drives a pro-angiogenic cascade for continued growth and invasion [24]. Hypoxia was confirmed with immunostaining of the spheroid cross-sections for HIF-1α, a biomarker for hypoxia (Figure 4.6D), and necrosis was observed in hematoxylin and eosin staining (Figure 4.6E). The spheroids showed considerable hypoxia and necrosis more prevalently in spheroids from the HIGH group. These data are in good agreement with previous literature regarding tumor spheroid progression (e.g. hypoxia and necrosis).

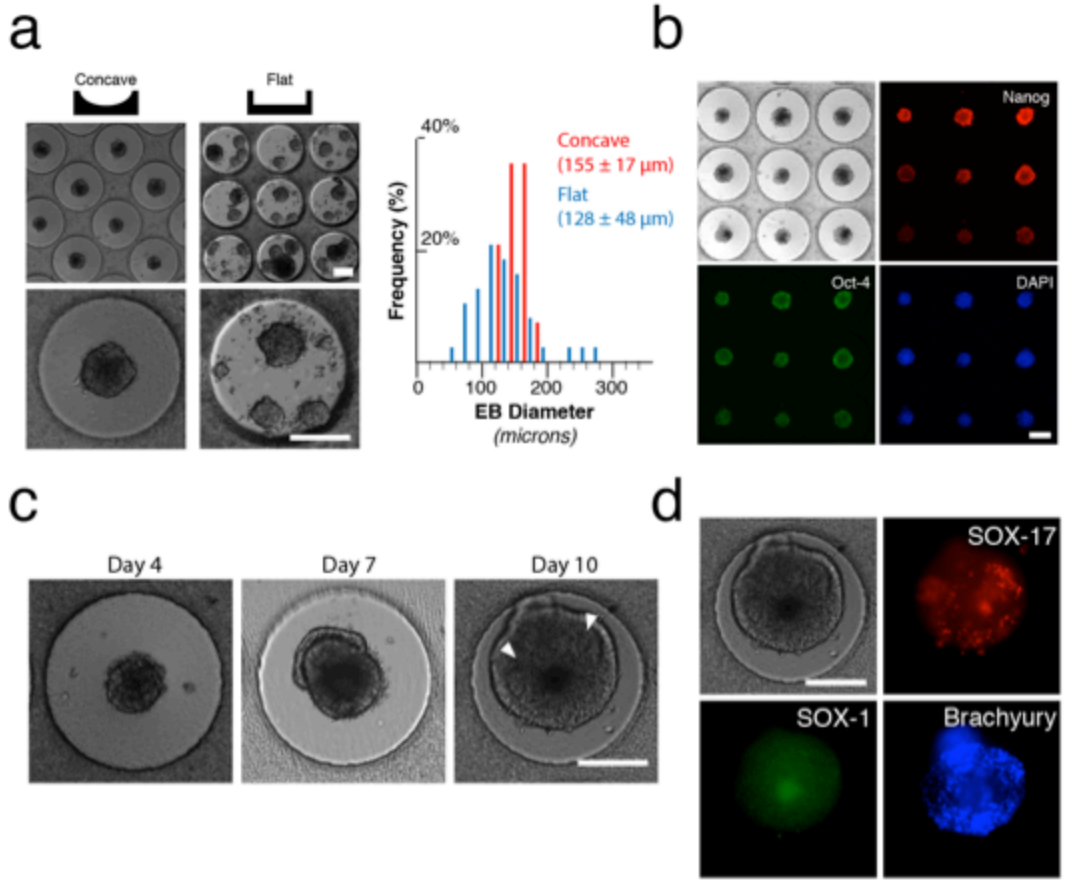

Figure 4.7: 3D printed concave hydrogels for embryoid body culture. A) Day 3 of human iPS cells grown on either concave hydrogels (cell seeding density 100 k mL^{-1}) or flat hydrogels (cell seeding density ~ 200 k mL^{-1}). Size distribution is quantified for each type (n = at least 14 for each group). **B**) Immunofluorescent staining of EBs on day 3 for Nanog and Oct4, two markers for pluripotency and non-differentiated cells, and DAPI, a nuclear stain. **C**) Brightfield images over longer timepoints (10 d), where white arrows indicate intra-organoid cavities. **D**) Immunofluorescent staining at day 10 of the three germ layers – ectoderm (SOX-1), endoderm (SOX-17), and mesoderm (brachyury) in concave hydrogels (initial cell seeding density ~ 100 k mL^{-1}). All scale bars = 200 µm.

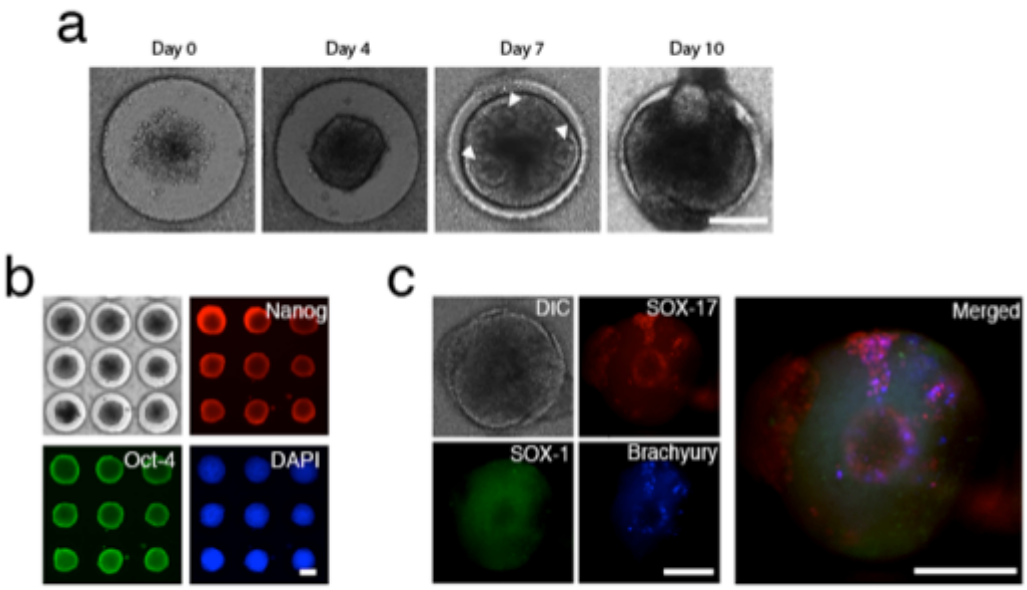

Figure 4.8: iPSC EBs formed from initial seeding density of 400 k mL^{-1}. A) Timelapse images of EB formation with iPS cells over 10 d. Arrows indicate areas of intra-organoid cavities, visual markers of differentiation. **B**) Immunofluorescent staining of pluripotent markers Nanog and Oct4 at day 3. **C**) Immunofluorescent staining at day 10 of the three germ layers – ectoderm (SOX-1), endoderm (SOX-17), and mesoderm (brachyury) in concave hydrogels. All scale bars = 200 μm.

Human iPSCs were utilized in subsequent experiments for generating and culturing EBs. iPSCs, derived by retroviral transduction of a combination of four transcription factors, Oct4, Sox2, c-Myc and Klf4, are stem cells with an equivalent self-renewal and differentiation capacity as embryonic stem cells [14]. In addition to their pluripotency, iPSCs provide a superior platform for clinical translation because they are autologous by nature (patient-specific). This facilitates their use in personalized disease modeling, drug testing, and regenerative medicine development, as well as minimizing any ethical concerns.

iPSCs were seeded on top of the concave hydrogels at a density of 100 k mL^{-1}. Single EBs formed after three days of culture, with an average diameter of 155 ± 17 μm (Figure 4.7A). Flat microstructures, conversely, generated a broader distribution of EB sizes, such that an initial seeding density of 200 k mL^{-1} produced EBs of 129 ± 48 μm. We reported similar observations for flat hydrogels with our breast cancer spheroids (Figure 4.4D). This is also consistent with previous literature on flat microwells that EBs only form at a critical cell density proportional to the microwell size, below which they form infrequently or at varied sizes [25]. At day 3, EBs showed pluripotency by immunostaining for Nanog and Oct4, transcription factors highly expressed in embryonic stem cells (Figure 4.7B). Similar results were seen with EBs formed from an initial cell density of 400 k mL^{-1} (Figure 4.8). Grown to day 10, EBs displayed morphological changes in their size, shape, and appearance in the form of intra-organoid cavities (Figure 4.7C and Figure 4.8). We hypothesized that this was due to spontaneous differentiation that can occur in these pluripotent cells, based on similar observations in the literature

[5]. Immunostaining confirmed EB differentiation to all three germ layers for both cell seeding densities, as evidenced by their co-expression of SOX-17 (endoderm), SOX-1 (ectoderm) and brachyury (mesoderm) (Figure 4.7D). These differentiation results serve to only show the possibility of visualizing differentiation of a single EB housed in the concave hydrogel. Further studies will be needed to address and quantify the different stages of embryogenesis and differentiation, as well as a more focused review on the necessary components in cell culture (e.g. media, growth factors) contributing to tissue-specific differentiation [4,26].

4.4 Conclusions

The concave hydrogel platform described here can be a valuable tool in the development of a multitude of spheroid-based cell culture models, especially for longer timepoints beyond the first media exchange. These may include tumor progression (e.g. proliferation, hypoxia, necrosis), migration and angiogenesis as well as various EB, and in particular iPSC, studies such as embryogenesis, organogenesis, toxicity, and patient-specific disease models. Due to its high reproducibility, low cost (material and time), ease of fabrication, and retention of the spheroids for long-term culture, this technology could also be adapted for high-throughput screening if individual hydrogel microstructures were to be printed into a high-throughput plate.

4.5 Acknowledgements

Chapter 4, in full, is a reformatted version of the published article as appears in Lab on a Chip, Volume 15 (2015). The dissertation author was the primary investigator and author of this paper, and thanks co-authors Dr. Darren Finlay, Xuanyi Ma, Dr. Xin Qu, Matthew G. Ondeck, Peter H. Chung, Fabian Zanella, Dr. Adam J. Engler, Dr. Farah Sheikh, Dr. Kristiina Vuori, and Dr. Shaochen Chen for their contributions. This work was supported by grants EB012597 and EB017876 from the NIH-National Institute of Biomedical Imaging and Bioengineering and grants CMMI-1332681 and CMMI-1120795 from the National Science Foundation (SC); the Saving tiny Heart Society and the California Institute of Regenerative Medicine (FS); ARRA grant (RC1 EB011780) from the NIH-National Institute of Biomedical Imaging and Bioengineering (KV); and DP020D006460 grant from the NIH (AJE). The authors would also like to thank John Warner for helpful discussions.

4.6 References

1 D. Huh, G.A. Hamilton, D.E. Ingber, *Trends in cell biology*, 2011, **21**, 745.

2 N.T. Elliott, F. Yuan, *Journal of pharmaceutical sciences*, 2011, **100**, 59.

3 F. Pampaloni, E.G. Reynaud, E.H. Stelzer, *Nature reviews. Molecular cell biology,* 2007, **8**, 839.

4 Y.S. Hwang, B.G. Chung, D. Ortmann, N. Hattori, H.C. Moeller, A. Khademhosseini, *Proceedings of the National Academy of Sciences of the United States of America*, 2009, **106**, 16978.

5 J. Itskovitz-Eldor, M. Schuldiner, D. Karsenti, A. Eden, O. Yanuka, M. Amit, H. Soreq, N. Benvenisty, *Molecular medicine*, 2000, **6**, 88.

6 J.R. Spence, C.N. Mayhew, S.A. Rankin, M.F. Kuhar, J.E. Vallance, K. Tolle, E.E. Hoskins, V.V. Kalinichenko, S.I. Wells, A.M. Zorn, N.F. Shroyer, J.M. Wells, *Nature*, 2011, **470**, 105.

7 A.M. Laib, A. Bartol, A. Alajati, T. Korff, H. Weber, H.G. Augustin, *Nature protocols*, 2009, **4**, 1202.

8 J.M. Kelm, V. Djonov, L.M. Ittner, D. Fluri, W. Born, S.P. Hoerstrup, M. Fussenegger, *Tissue engineering*, 2006, **12**, 2151.

9 F. Hirschhaeuser, H. Menne, C. Dittfeld, J. West, W. Mueller-Klieser, L.A. Kunz Schughart, *Journal of biotechnology*, 2010, **148**, 3.

10 J. Fukuda, K. Nakazawa, *Tissue Eng*, 2005, **11**, 1254.

11 C.R. Thoma, S. Stroebel, N. Rosch, B. Calpe, W. Krek, J.M. Kelm, *Journal of biomolecular screening*, 2013, **18**, 1330.

12 Y.Y. Choi, B.G. Chung, D.H. Lee, A. Khademhosseini, J.H. Kim, S.H. Lee, *Biomaterials*, 2010, **31**, 4296.

13 G.S Jeong, J.H. Song, A.R. Kang, Y. Jun, J.H. Kim, J.Y. Chang, S.H. Lee, *Adv Healthc Mater*, 2013, **2**, 119.

14 H.C. Moeller, M.K. Mian, S. Shrivastava, B.G. Chung, A. Khademhosseini, *Biomaterials*, 2008, **29**, 752.

15 J.M. Karp, J. Yeh, G. Eng, J. Fukuda, J. Blumling, K.Y. Suh, J. Cheng, A. Mahdavi, J. Borenstein, R. Langer, A. Khademhosseini, *Lab on a chip*, 2007, **7**, 786.

16 M.D. Ungrin, C. Joshi, A. Nica, C. Bauwens, P.W. Zandstra, *PloS one*, 2008, **3**, e1565.

17 N.A. Peppas, J.Z. Hilt, A. Khademhosseini, R. Langer, *Adv Mater*, 2006, **18**, 1345.

18 A.P. Zhang, X. Qu, P. Soman, K.C. Hribar, J.W. Lee, S.C. Chen, S. He, *Adv Mat*er 2012, **24**, 4266.

19 Y.S. Choi, L.G. Vincent, A.R. Lee, K.C. Kretchmer, S. Chirasatitsin, M.K. Dobke, A.J. Engler, *Biomaterials*, 2012, **33**, 6943.

20 M. Radmacher, *Method Cell Biol*, 2007, **83**, 347.

21 K.C. Hribar, P. Soman, J. Warner, P. Chung, S. Chen, *Lab on a chip*, 2014, **14**, 268.

22 S. Kizilel, V.H. Perez-Luna, F. Teymour, *Macromol Theor Simul* 2006, **15**, 686.

23 G. Metha, A.Y. Hsiao, M. Ingram, G.D. Luker, S. Takayama, *J Control Release*, 2012, **164**, 192.

24 D. Shweiki, M. Neeman, A. Itin, E. Keshet, *Proceedings of the National Academy of Sciences of the United States of America*, 1995, **92**, 768.

25 K. Takahashi, K. Tanabe, M. Ohnuki, M. Narita, T. Ichisaka, K. Tomoda, S. Yamanaka, *Cell*, 2007, **131**, 861.

26 M. Schuldiner, O. Yanuka, J. Iskovitz-Eldor, D.A. Melton, N. Benvenisty, *Proceedings of the National Academy of Sciences of the United States of America*, 2000, **97**, 11307.

Chapter 5

Novel Bio-printed Tumor-matrix Model Predicts Drug Efficacy and Potential Side-Effects

Abstract

A common hurdle in testing novel drugs and combination treatments for human disease is the lack of affordable, highly reproducible models from which to study the drug's effects on concurrently both tumor and surrounding microenvironment. Current anti-cancer drug evaluation relies on a set of *in vitro* assays that test singular populations of tumor cells for toxicity and in some cases migration, invasion and sphere forming capability, followed by costly *in vivo* animal model testing. A novel 3D projection printing platform allows for the first time multiple cell populations to be concurrently assessed after drug treatment allowing a less expensive, highly reproducible system for testing, potentially saving considerable research funds otherwise spent on costly animal models. Here, fabricated structures consisting of glioblastoma cells and microenvironment populations such as endothelial cells, allow evaluation of an anti-cancer drug's effect on tumor proliferation, invasion, ability to interact with microenvironment, transdifferentiation and importantly potential deleterious effects on

normal, non-tumorigenic cell populations, all of which are valuable predictors of *in vivo* anti-cancer drug affects.

5.1 Introduction

Historically, two-dimensional (2D) cell tissue culture has been employed for studying singular cell populations and disease states, including those of cancer. Cells intended for tissue culture are obtained through surgical resection, dissociation and finally plated onto a tissue culture dish with growth media. Here cells are not only being forced to adapt to a new environment and growth supplement, but also to a new structure - being removed from a larger three-dimensional structure in vivo, to an unnatural 2D platform. It has been demonstrated that cells not only display distinct morphological changes when in 2D that differ from their morphology in 3D [1], but also show significantly altered gene expression patterns [2-4], suggesting analyses using this system as a platform for cancer drug discovery could be an inaccurate representation of true actions *in vivo*.

Advances in cancer research have allowed for development of 3D models of cancer cells, in order to mimic physiological cell-cell contacts and increase intercellular signaling [5]. A common assay in breast cancer includes culturing tumor cells in soft agar, a semi-solid matrix, allowing them to form spheroids [6, 7]. Studying tumor spheroids allows a testing platform for novel compounds and their effect on proliferation and migration. Even with these advanced tissue culture models, there exists a dependence on animal models to recapitulate the disease and overall effectiveness of a novel drug, or combination treatment when assessed with microenvironmental changes and tumor adaptation. Animal models allow another dimension of analysis including tumor interaction and invasion into normal surrounding cells and tissues, blood vessel co-

option, angiogenesis and tumor recurrence. In addition to animal models being costly, they also require significant time, and staff resources.

In a cross-collaboration between bioengineering and cancer biology, 3D cell culture provides a means to more accurately model physiological tumors and surrounding microenvironment for preclinical studies including drug screening to assess cell responses not seen in single population 2D cultures [8, 9]. In particular, light-assisted 3D direct printing of hydrogels encapsulated cell populations has potential for a wide variety of applications for diagnostic and *in vitro* novel drug and combination treatment testing [10].

Here we created a hydrogel multi-population bioprinted tumor model made from a 3D projection printer. This platform allows for the study of multi-population cell interaction, migration, invasion, angiogenesis, cell co-option, transdifferentiation and finally population shrinkage and growth within a single well. This system is highly reproducible, easily stored, fixable, stainable, transportable and can be modified to accommodate any two or more populations of cells of diseased and/or non-diseased state and any model cell type. The goal of this novel application is to provide a low cost and reproducible testing platform for assessing multi-population interaction, toxicity and off target effects of novel drug combinations potentially saving critical research dollars wasted on costly *in vivo* animal models.

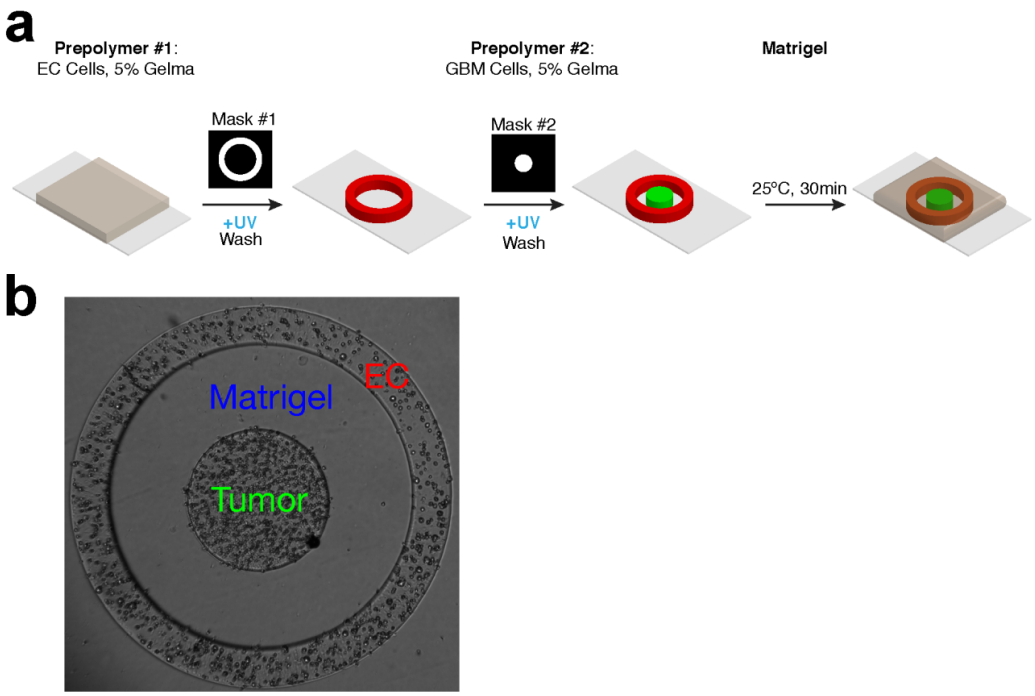

Figure 5.1: Photocrosslinkable hydrogel Design. **A**) 3D bioprinted slides Photocrosslinkable hydrogels are secured to a glass substrate by UV exposure. Gel 1 is the middle circular hydrogel comprising cell population 1, and Gel 2 is the outer ring of hydrogel comprising cell population 2. The thickness of the gels may be varied. A space between the middle print and the outer ring print may be incorporated. A third hydrogel may be overlaid the two printed structures to encapsulate the entire system for facilitating cell communications between the two populations. Created by using a mask-based 3D printer. Two digital masks (circle and ring) are created in computer software and uploaded to the digital micro mirror device of a 3D projection printer. UV light exposed on mask 1 is projected on to the material, polymerizing the ring structure which encompasses hydrogel 1 + cell type #1. The excess un-reacted material is washed away and hydrogel 2 + cell type #2 are added. Upon UV exposure to the mask 2, the circular structure is polymerized. **B**) Bioprinted Tumor (center, green), and endothelial cells (border ring, red) and spatial regions (no cells, matrigel).

5.2 Materials and Methods

5.2.1 Materials

Gelatin Methacrylate (GelMA) was synthesized by previously reported protocols, with a methacrylation rate of ~71% according to NMR [11]. LAP photoinitiator was synthesized according to previous reports [12].

5.2.2 3D Printing of Separate Endothelial and Tumor Cell Populations

A previously described 3D projection printer was used to fabricate the 3D structures with distinct cell populations [13, 14]. GelMA (5 % w/v) was mixed with photoinitiator lithium phenyl-2,4,6- trimethylbenzoylphosphinate (LAP) (0.12%) and either 005 glioblastoma cells (8.0 million / mL) or bend3 endothelial cells (2.5 million / mL).

The prepolymer solution is pipetted between a glass slide that has a thin layer of PDMS (50μm) on its surface, and a glass cover slip, which is spaced 125 μm apart using additional PDMS layers. Any size spacer (i.e. thickness of the PDMS) can be applied to dictate the thickness of the printed structure. Importantly, the cover slips are pretreated with the chemical modification of 3-(Trimethoxysilyl)-Propyl Methacrylate so the hydrogels chemically link to the glass substrate.

The 3D printer setup is similar to our previous work. Mainly, a digital micromirror device displays a computer-generated image. The image, or “mask” is designed in a CAD software and translated to the DMD software. In this case, the endothelial bend3 cell print is in the shape of a ring (width = 3 mm, ring diameter = 250μm), and the GBM 005 tumor print is in the shape of a circle (1 mm in diameter)

(Figure 5.1). Again, the size of each print, including the distance between bend3 and GBM prints, could potentially be adjusted by changing the design in the CAD drawing, however we kept these variables constant. By exposing the DMD chip to UV light (S2000, Omnicure), the pattern is photopolmerized in the prepolymer solution, and the cell-laden hydrogel is printed in the intended design.

For both bend3 and GBM prints, we used 6 mW/cm^2 power and exposed the samples for 45 seconds of UV light. After each successive print, the samples were washed thoroughly in dPBS, and excess liquid was aspirated away. Samples were placed in a 24-well plate after thorough washing. Upon printing each structure (bend3 and GBM prints together), 10 μL of matrigel was applied on top of each structure and allowed to gel for 30 min at room temperature. Fresh EGM-2 media (1 mL per well) was then applied to each sample and the samples were stored in incubation (37 ºC, 5% CO_2.

5.2.3 Cell Culture and Drug Study

EGM-2 media was exchanged every four days for each sample leading up to day 21. On day 21, the drug study was initiated. Media consisting of DMEM with 10 % FBS and 1 % Penicillin/Streptomycin was used post-day 21. Samples were exposed to four different conditions: control (media alone); anti-VEGF treatment (10 ng/ml), TMZ (Temozolomide, 50 μM), or combination treatment (anti-VEGF + TMZ).

5.2.4 3D Printed Sample Imaging

Samples were imaged at various timepoints using a Leica fluorescence microscope. Due to the GFP labeling of the tumor cells, fluorescent tracking of GBM cells was possible. Cells could be further stained with alternative dyes for real-time tracking, however this was not introduced. Images were taken every several days, noting

morphological changes in the cellular response, and invasion of the tumor cells in the matrigel matrix between the two prints.

5.2.5 Immunological Staining and Imaging

Samples were fixed with 4 % paraformaldehyde at room temperature for 10 minutes. Samples were stained for endothelial marker VWF, stem cell marker nestin, and nuclear dapi. VWF, GFP, nestin, and dapi were imaged using a confocal microscope.

5.2.6 Image Analysis

Fluorescent images were collected at various timepoints from the Leica microscope. Confocal would ideally be needed for understanding 3D tumor progression in our GFP-labelled tumor print, however we used a conventional fluorescent microscope due to availability. Fluorescent images were analyzed in ImageJ software. Each image was set to 8-bit and thresholded, outlining the fluorescent area. Quantification of the fluorescence was performed and analyzed at each time point.

Tumor invasion was determined by taking the fluorescent area beyond the original tumor print, and the percent invasion (% invasion) was determined by this area at each point in relation to an earlier timepoint. For instance, for tumor invasion during drug treatment, % invasion is determined by day X invasion area divided by day 21 (day 0 of the drug treatment). For tumor invasion prior to day 21, % invasion was normalized to the first time of imaging (day 8).

Confocal images from immunological staining were analyzed in ImageJ by taking the threshold for each image, and created a merged image of either VWF/GFP or nestin/GFP with red/green channels. The overlap of the two channels in each group was colored yellow and quantified as the percent of the total GFP.

5.3 Results

5.3.1 3D Bioprinted Tumor-Matrix Design to mimic in vivo tumor characteristics

In order to create stable multi-population 3D bioprints, photocrosslinkable hydrogels made of GelMA are secured to a glass substrate by UV exposure. GelMA, a photopolymerizable biomaterial derived from gelatin, is denatured collagen that still retains adhesion moieties such as RGD, and that has been functionalized with reactive acrylate groups. Importantly, the cover slips are pretreated with the chemical modification of 3-(Trimethoxysilyl)-Propyl Methacrylate so the hydrogels chemically link to the glass substrate. Based on the degree of acrylation and % GelMA, the hydrogel product can achieve modular material properties (stiffness, swelling, porosity), making it great material of choice for tissue engineering [11]. Here GelMA (5 % w/v) was mixed with photoinitiator lithium phenyl-2,4,6- trimethylbenzoylphosphinate (LAP) (0.12%) and either 005 glioblastoma cells (8.0 million / mL) for center round or bend3 endothelial cells (2.5 million / mL) printed on outer ring.

Gel 1 is the middle circular hydrogel comprising cell population 1, and Gel 2 is the outer ring of hydrogel comprising cell population 2 (Figure 5.1A & B). A space between the middle print and the outer ring print is incorporated (Figure 5.1A) to allow for visualization of cell invasion, migration and interaction with secondary cell population printed in outer ring. A third hydrogel, matrigel, is overlaid the two printed structures to encapsulate the entire system for facilitating cell communications between the two populations. This multipopulation 3D platform is created by using a mask-based 3D printer [10, 12-14]. Mainly, a digital micromirror device displays an computer-

generated image. The image, or "mask" is designed in a CAD software and translated to the DMD software. In this case, the endothelial bend3 cell print is in the shape of a ring (width = 3 mm, ring diameter = 250μm), and the GBM 005 tumor print is in the shape of a circle (1 mm in diameter) (Figure 5.1A). The size of each print, including the distance between bend3 and GBM prints, could potentially be adjusted by changing the design in the CAD drawing, however we kept these variables constant. By exposing the DMD chip to UV light (S2000, Omnicure), the pattern is photopolmerized in the prepolymer solution, and the cell-laden hydrogel is printed in the intended design.

For both bend3 and GBM prints, we used 6 mW/cm^2 power and exposed the samples for 45 seconds of UV light. After each successive print, the samples were washed thoroughly in dPBS, and excess liquid was aspirated away. Upon printing each structure (bend3 and GBM prints together), 10 μL of matrigel was applied on top of each structure and allowed to gel for 30 min at room temperature. Fresh EGM-2 media (1 mL per well) was then applied to each sample and the samples were stored in incubation (37 ºC, 5% CO_2) until drug treatment studies.

5.3.2 Pre-treatment Evolution of 3D Cancer Model

Figure 5.2 summarizes the evolution of the tumor-matrix co-culture system after 3D printing illustrating a cancer angiogenesis model. The ring (5% gelatin methacrylate with bend3 endothelial cells) and inner circle (5% gelatin methacrylate with green-fluorescent protein-labelled glioblastoma cells) are encapsulated with matrigel and co-cultured in endothelial growth media (EGM-2, Lonza). Cancer cell invasion into the void space between the cellular prints is visible after day 8, followed by tumor cell interaction with the non-fluorescently labeled endothelial cells. Once tumor cells make contact with

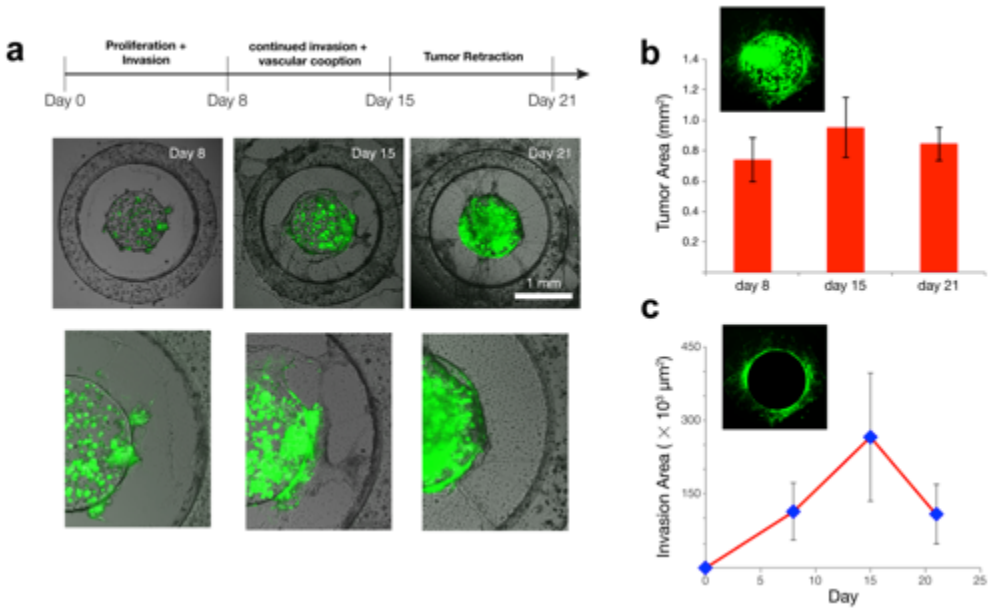

Figure 5.2: 3D bioprinted matrix evolution prior to novel drug or combination treatment. **A**) Following 3D bioprinting tumor cells can be visualized confined to the original print site at center. **B)** Tumor area, due to proliferation and invasion, appears to grow beyond original print site from day 8 to day 15. This is immediately followed by tumor retraction from endothelial border by day 21 resulting in tube structures connecting the tumor to the endothelial border printed ring. **C**) Quantification of invasion area.

outer ring of endothelial cells the tumor begins retraction back towards the core tumor, resulting in some endothelial cells being co-opted towards the tumor core printed structure. During this time, average tumor area increases by 0.3 mm^2 followed by a retraction and average tumor area decrease of 0.2 mm^2 (Figure 5.2B). In addition to tumor area variation, tumor invasion changes by an average $3x10^5$ μm^2 by day 15, followed by a retraction towards the original print area of an average $2x10^5$ μm^2 (Figure 5.2C), resulting in an average invasion distance from original tumor print site of $1x10^5$ μm^2 at time of drug treatment (day 21, Figure 5.2C). In addition, at day 21, non-fluorescent micro-tubules are visibly seen projecting from the inner tumor circular structure, possible evidence of angiogenesis as seen by endothelial cell co-option into a tube structure towards the printed tumor core. This tumor invasion and retraction phase is unique to the matrigel coated bioprints, and results in the unique ability to assess tumor-microenvironment co-option, tumor-endothelial interaction, and tumor cell transdifferentiation both before and after drug treatment.

5.3.3 3D Bioprinted Model predicts Drug Efficacy and off-target side effects

We have utilized the 3D-printed multi-population model to study the effects of anti-cancer drugs on tumor progression and synergy alterations with the microenvironment. Similar to what is known of temozolomide treatment in patients [15, 16] and cell lines [17], tumor regression and death is only noted with this treatment (Figure 5.3 & 4). Tumor *progression* is noted in control samples (no drug), anti-VEGF treatment, and combination TMZ+ anti-VEGF treatment (Figure 5.3 & 4). Anti-VEGF is an FDA-approved drug used for blocking angiogenesis in glioblastoma, however has not seen clinically significant survival enhancement. Recurrent tumors within patients

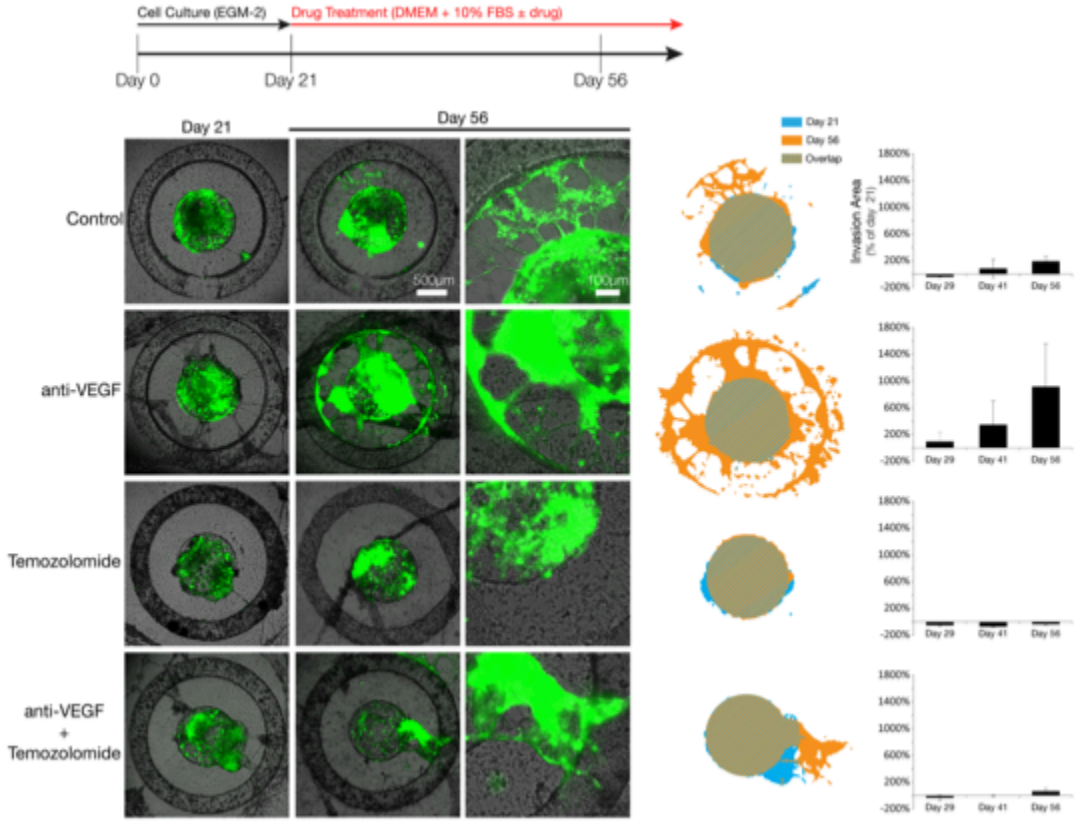

Figure 5.3: Application testing with known drug combinations. After 21 days bioprints were treated with corresponding drugs (anti-VEGF 10ng/ml and/or Temozolamide 50 μM) until day 56 to monitor cellular and cell-cell changes over time. Cellular changes are monitored by new growth (Orange) and compared with overlap with original tumor bulk (gray). Invasion area is quantified based on areas of these respective regionsand charted from Day 29, 41 and finally day 56.

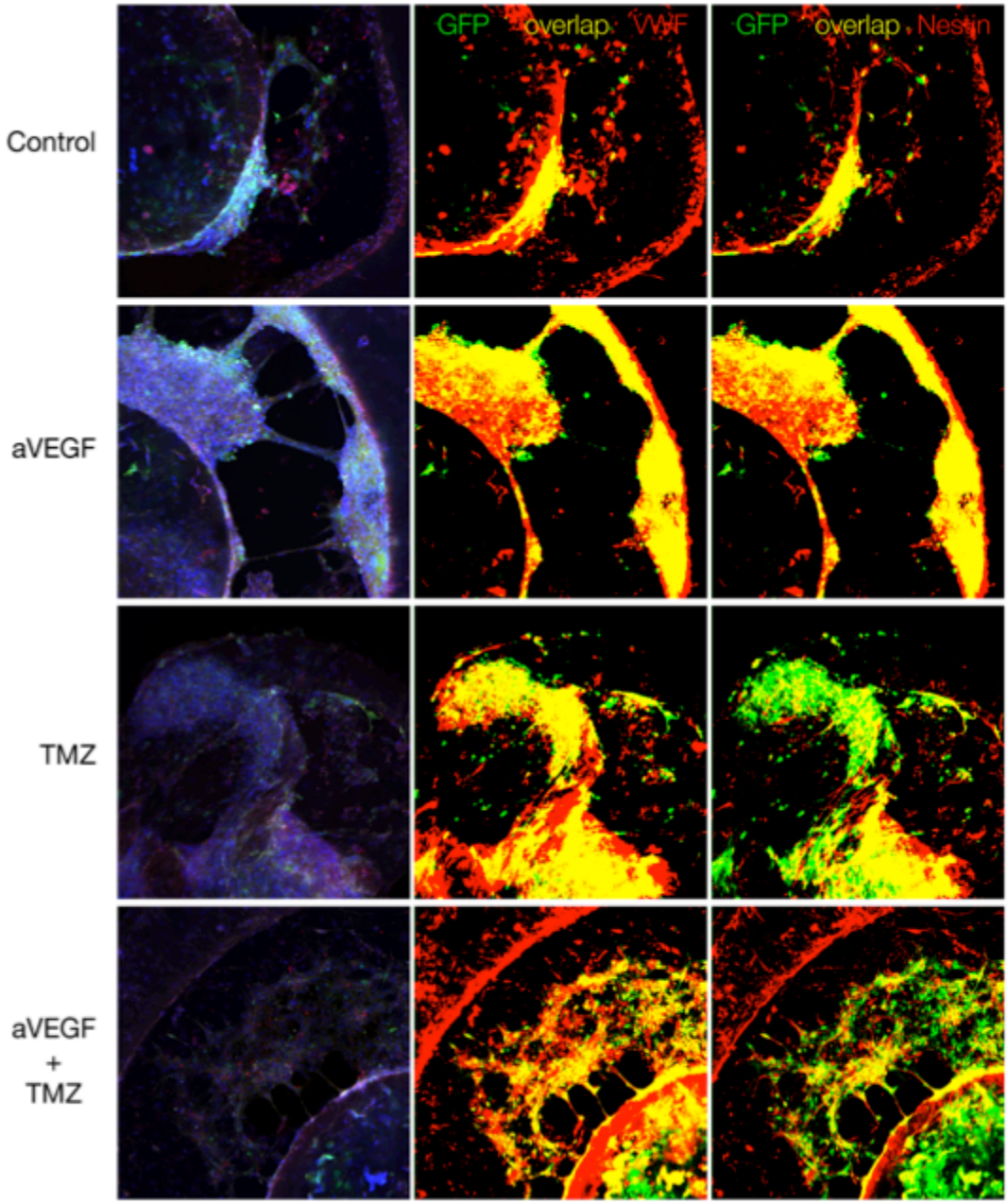

Figure 5.4: Confocal Analysis of Independent Population Markers. 3D bioprinted slides were fixed with 4% PFA in PBSfor 15minutes followed by IF preparation, internal GFP marker for Glioblastoma cells and conversely endothelial specific marker vWf (red) or Nestin (red) and overlap in yellow. Mouse GBM cells were either left untreated, treated with 10 ng/ml anti-VEGF, treated with 50 μM TMZ or treated with both anti-VEGF and TMZ concurrently. Images were captured from a Zeiss LSM710 Laser Scanner confocal microscope using 20X objective.

become highly aggressive and are resistant to standard therapy [18, 19]. Initial results from this testing platform indicate an increase in aggressiveness of Anti-VEGF treated GBM cells similar to that expected based on human, and mouse model data [20]. In addition, this model allows visualization of increased transdifferentiation, shown by GFP+ tube structures radiating between tumor and EC printed rings (Figure 5.3 & 5.4), in anti-VEGF treated samples consistent with published data suggesting recurrent tumors become resistant to anti-VEGF therapy by promoting a tumor to endothelial cell type transdifferentiation [21, 22]. This aggressive tumor behavior appears to become more severe when used in combination with TMZ in our 3D bioprinted model similar to patient response after DNA damage agents used in combination with anti-VEGF therapy [23]. Previously, recapitulating and predicting these human clinical outcomes could only be uncovered through expensive animal model testing, however this platform provides a much more inexpensive, and ability to test on human cell combinations that previously would not be possible. Thus, this novel 3D bioprinted, multi-population technology provides a predictive model for anti-cancer drug efficacy with clinical implications, including possible off-target side effects.

5.4 Discussion

Several platforms exist to test a single population of cells however studying several populations of cells interacting with another has been difficult due to growth condition variability, utility and application testing difficulties of co-cultures in 2D. The development of this 3D bioprinted testing platform is unique in its ability to be used as an efficient, application for testing, imaging and data analysis of multiple cell types and their

interaction with one another. The novel component is its radial design of a spatially patterned three-dimensional co-culture with the inclusion of an attachment matrix layer between the two populations permitting observation of tumor invasion, cell co-option, angiogenesis, tumor and/or microenvironment migration (repulsion/attraction) and general cell interaction to be assessed at early points of contact between the cells. This model was validated using existing drug combinations for treatment of glioblastoma, with results closely mimicking those observed in patient and mouse models and not seen in *in vitro* monolayer studies. It is our goal that future studies using this 3D bioprinted tumor-microenvironment technology will evolve to include other tumor associated cell types such as macrophages, pericytes and supportive smooth muscle cell populations. This technology can grow into representing other cancer systems, or disease comparisons. And finally, the ultimate goal would be to employ this 3D model as a novel testing platform in drug discovery that could save money and time otherwise spent on costly, needless mouse models.

5.5 Acknowledgements

Chapter 5, in full, is currently being prepared for submission for publication of the material. The dissertation author was the primary investigator and author of this paper, and thanks co-authors Dr. Amy Rommel, Dr. Inder Verma, and Dr. Shaochen Chen for their contributions. This work was supported by the National Institute of Health (NIH, grants EB017876 (SC) and HL053670 (IV)) and The Leona M. and Harry B. Helmsley Charitable Trust (grant 2012-PG-MED002) (IV).

5.6 References

1. E. Knight, S. Przyborski, *Journal of anatomy*, (Nov 20, 2014).

2. L. Vergani, M. Grattarola, C. Nicolini, *The international journal of biochemistry & cell biology*, 2004, **36**, 1447.

3. C. H. Thomas, J. H. Collier, C. S. Sfeir, K. E. Healy, *Proceedings of the National Academy of Sciences of the United States of America*, 2002, **99**, 1972.

4. M. Lu, F. Zhou, K. Hao, J. Liu, Q. Chen, P. Ni, H. Zhou, G. Wang, J. Zhang, *Biochemical pharmacology*, 2015, **93**, 210.

5. C. R. Thoma, M. Zimmermann, I. Agarkova, J. M. Kelm, W. Krek, *Advanced drug delivery reviews*, 2014, **69-70**, 29.

6. J. Benard, P. Schreiner, J. C. Delarue, C. Contesso, G. Riou, *Neoplasma*, 1983, **30**, 159.

7. S. Chumsri, P. Phatak, M.J. Edelman, K. Khakpour, A.W. Hamburger, A.M. Burger, *Cancer genomics & proteomics*, 2007, **4**, 165.

8. D. Huh, G. A. Hamilton, D. E. Ingber, *Trends in cell biology*, 2011, **21**, 745.

9. F. Pampaloni, E. G. Reynaud, E. H. Stelzer, *Nature reviews. Molecular cell biology*, 2007, **8**, 839.

10. K. C. Hribar, P. Soman, J. Warner, P. Chung, S. Chen, *Lab on a chip*, 2014, **14**, 268.

11. J.W. Nichol, S. Koshy, H. Bae, C.M. Hwang, S. Yamanlar, A. Khademhosseini, *Biomaterials*, 2010, **31**, 5536.

12. B. D. Fairbanks, M. P. Schwartz, C. N. Bowman, K. S. Anseth, *Biomaterials*, 2009, **30**, 6702.

13. A.P. Zhang, X. Qu, P. Soman, K.C. Hribar, J.W. Lee, S. Chen, S. He, *Advanced Materials*, 2012, **24**, 4266.

14. Y. Lu, G. Mapili, G. Suhali, S.C. Chen, K. Roy, *J Biomed Mater Res A*, 2006,**77A**, 396-405.

15. R. Stupp, W.P. Mason, M.J. van den Bent, M. Weller, B. Fisher, M.J.B. Taphoorn, K. Belanger, A. Brandes, C. Marosi, U. Bogdahn *et al.*, *The New England journal of medicine*, 2005, **352**, 987.

16. D. Osoba, M. Brada, W. K. Yung, M. Prados, *Journal of clinical oncology : official journal of the American Society of Clinical Oncology*, 2000, **18**, 1481.

17. Y. Hirose, M. S. Berger, R. O. *Cancer research*, 2001, **61**, 1957.

18. Y. Piao, J. Liang, L. Holmes, V. Henry, E. Sulman, J.F. de Groot, *Clinical cancer research : an official journal of the American Association for Cancer Research*, 2013, **19**, 4392.

19. O. Keunen, M. Johansson, A. Oudin, M. Sanzey, S.A. Rahim, F. Fack, F. Thorsen, T. Taxt, M. Bartos, R. Jirik *et al.*, *Proceedings of the National Academy of Sciences of the United States of America*, 2011, **108**, 3749.

20. J.F. de Groot, G. Fuller, A.J. Kumar, Y. Piao, K. Eterovic, Y. Ji, C.A. Conrad, *Neuro-oncology*, 2010, **12**, 233.

21. Y. Soda, T. Marumoto, D. Friedmann-Morvinski, M. Soda, F. Liu, H. Michiue, S. Pastorino, M. Yeng, R.M. Hoffman, S. Kesari, I.M. Verma, *Proceedings of the National Academy of Sciences of the United States of America*, 2011, **108**, 4274.

22. Y. Soda, C. Myskiw, A. Rommel, I. M. Verma, *Journal of molecular medicine*, 2013, **91**, 439.

23. T. T. Batchelor, E.R. Gerstner, K.E. Emblem, D.G. Duda, J. Kalpathy-Cramer, M. Snuderl, M. Ancukiewicz, P. Polaskova, M.C. Pinho, D. Jennings *et al.*, *Proceedings of the National Academy of Sciences of the United States of America*, 2013, **110**, 19059.

Chapter 6

Conclusions

Light-assisted patterning of hydrogels can vastly improve our ability to understand three-dimensional (3D) cellular interactions in the tissue microenvironment, and develop model systems that more closely reflect the *in vivo* human condition. In this dissertation, we aimed to explore several patterning techniques using a focused laser and light projection.

In chapter 2, we described digital plasmonic patterning (DPP), which utilizes a focused near-infrared light source to photothermally activate gold nanorods and pattern stiffness changes on a hydrogel substrate. Cell response such as durotaxis –the migration of cells from soft to stiff substrates – and alignment was observed. In chapter 3, we expanded the utility of gold nanorods to pattern hydrogels by applying this concept to a 3D collagen hydrogel model. We showed selective patterning of the gel by ultrafast laser-induced degradation (ULID) of collagen, producing channels into which endothelial cells migrated, aligned, and eventually formed tube-like structures similar to microvasculature.

In chapters 4 and 5, we turned to 3D projection printing to modulate cell behavior. First, in chapter 4, we demonstrated that non-linear projection printing could achieve hydrogels with controlled concavities. Breast cancer cells and stem cells seeded on top of these hydrogels aggregated due the gel's concavity, and in independent experiments formed tumor spheroids and embryoid bodies that were consistent with *in vivo* tumor and embryological characteristics, respectively. In chapter 5, we utilized projection printing

to develop a novel 3D bioprinted model of glioblastoma. By initially printing glioblastoma and its vascular cells in separate locations, and overlaying a secondary gel, we were able to observe cell interactions between the tumor and its vasculature that have not been seen *in vitro* before. Moreover, we tested the model with FDA approved drugs, and saw clinically relevant responses and side effects of the drugs.

In closing, the author believes this work is the tip of the iceberg for light-assisted patterning of hydrogels for cell biology applications. The impact of generating human-relevant tissue models *in vitro* can be immensely beneficial to the pharmaceutical, diagnostics, and medical industries at large, saving money from costly animal studies and providing a more predictive measure to study drug responses.